



10-3-08  
7  
009

**LIBRARY  
Michigan State  
University**

This is to certify that the  
dissertation entitled

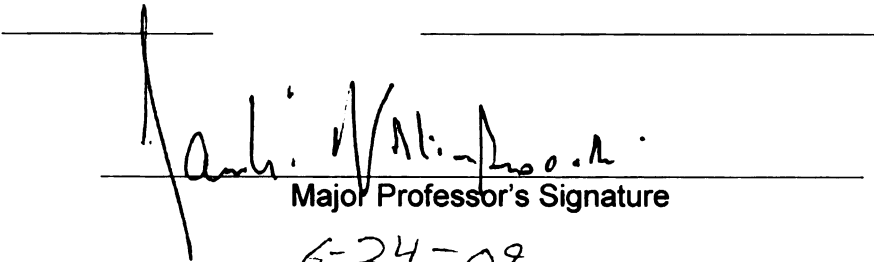
**A Real Time Bacterial Cell Detection System**

presented by

**Trevor Thomas Pled Barkham**

has been accepted towards fulfillment  
of the requirements for the

Ph.D degree in **Biochemistry and Molecular  
Biology  
and Chemistry**

  
Major Professor's Signature

6-24-09

**PLACE IN RETURN BOX** to remove this checkout from your record.  
**TO AVOID FINES** return on or before date due.  
**MAY BE RECALLED** with earlier due date if requested.

DATE DUE	DATE DUE	DATE DUE

**A Real Time Bacterial Cell Detection System**

**By**

**Trevor Thomas Pled Barkham**

**A DISSERTATION**

**Submitted to  
Michigan State University  
in partial fulfillment of the requirements  
for the degree of**

**DOCTOR OF PHILOSOPHY**

**Biochemistry and Molecular Biology  
and Chemistry**

**2009**



## **Abstract**

### **A Real Time Bacterial Cell Detection System**

By

Trevor Thomas Pled Barkham

The detection and prevention of microbial pathogens has always been a challenge. The development of new technologies over the years has brought with it improvements in our ability to detect and prevent infection by microbial pathogens, resulting in dramatic advances in the quality of public health. The first step in the prevention of infection by and spread of microbial pathogens is accurate detection. Our ability to quickly and precisely detect a specific microbial pathogen greatly enhances our ability to take the proper actions. There are many shortcomings in the current detection platform technologies. The many features required of a detection platform are speed, accuracy, sensitivity, portability, robustness, and ease-of-use. The overarching goal of this project is to design and fabricate a functional pathogen detection platform based on basic physical laws that uses simple electronic, chemical and biological technologies, and is capable of the real time detection of bacteria. Real time detection of a single bacterium is not an easy task. There is very little in the way of measurable or inducible signals that would allow detection let alone be specific enough for identification. The obvious solution then is to add a signal to the bacterium. In our strategy, ferromagnetic nanocomposite particles (FMNCPs) that contain surface recognition elements that can detect and bind to specific bacterial cell surface structures are used even if known to contain many complex surface

antigens. The FMNCPs utilize the bacterium's surface as a scaffold to coat the bacterium and effectively make a micro-magnet which can be detected by several types of magnetic sensors.

We will show that we have been able to design, fabricate, and test our detection platform and have shown that our detection platform is capable of real time detection of low concentrations of bacteria within five minutes.

Demonstrating ferromagnetic nanocomposite particles can be used for the detection of bacterial cell by magnetic induction with a search coil.

Copyright By  
Trevor Thomas Pled Barkham  
2009

## **ACKNOWLEDGMENTS**

My time at Michigan State has been a learning, and eye opening experience. Not just in the sciences, but life and the workings of the world. This has not been an easy path for me, and I would not be here if it wasn't for the support and help of many people. I would like to thank everyone how has helped me on my way.

Firstly, I would like the thank Dr. Rawle I. Hollingsworth for taking me into his lab and providing numerous opportunities and experiences. Your patience and guidance over the past years have been greatly appreciated. Thank you for your confidence. My appreciation is also expressed to my Graduate Committee: Drs. Charles Hoogstraten, Kathy Hunt, Ned Jackson, Bill Wedemeyer, and Greg Zeikus for their valuable insight and perspectives contributing to my project and professional development.

I would like to thank the members of the Hollingsworth Lab. As colleagues and friends you have all enriched studies and view of the world. Thank you Kun for always playing devils advocate even when you agree with me. Dr. Kuhn thank you for your help, insight, and perspective over the years. Dr. Kuhn, Dorothy Black and Matt Horn Thank you for reviewing and helping me with my paper. I would like to acknowledge the staff in the center for advanced microscopy. The entire staff has been most helpful, always willing to listen to and work with me. I would also like acknowledge the entire staff of the Biochemistry department from the repair shop to the receptionist's offices; you have aided me in resolving many problems and complaints.

I am most thankful for my Parents, Tom and Ruth. Thank you for all that you have done for me over the years and all that you have not done. You have helped become the man I am today. Thank you to all my family from grandma to brother you have all helped to shape me.

I would like to thank my wife Emily and my sons Edward and Benjamin, for their love and encouragement. Emily thank you for putting up with so much, I love you and appreciate all that you have done for me and with me.

## TABLE OF CONTENTS

<b>LIST OF TABLES.....</b>	<b>ix</b>
<b>LIST OF FIGURES.....</b>	<b>x</b>
<b>LIST OF ABBREVIATIONS.....</b>	<b>xiii</b>
<b>CHAPTER 1</b>	
Background: Detection of Bacteria.....	1
Introduction.....	1
Detection Platforms.....	9
Challenges Shared by All Detection Platforms.....	22
The Potential for Magnetic Detection.....	24
References.....	28
<b>CHAPTER 2</b>	
The Big Idea: Magnetic Modification of Bacteria.....	32
Introduction.....	32
Design of FMNCPs.....	37
Macromolecular Polymer System.....	37
Detection Platform Design.....	41
Theoretical Calculations and Expected Values.....	42
Noise.....	49
References.....	52
<b>CHAPTER 3</b>	
Macromolecular Polymer System.....	53
Introduction.....	53
Experimental.....	56
Results and Discussion.....	57
References.....	64
<b>CHAPTER 4</b>	
Nanocomposite Material.....	65
Introduction.....	65
Ferromagnetic Nanoparticles.....	66
Interaction of Ferromagnetic Nanoparticles.....	69
FMNCP and Bacterium Binding.....	74
Experimental.....	79
Results and Discussion.....	81
References.....	103

## **CHAPTER 5**

The Detection System.....	106
Introduction.....	106
Experimental.....	109
Results and Discussion.....	111
Conclusion.....	130
References.....	135

## **Appendix A**

Magnetism.....	136
Introduction.....	136
Magnetic Energies.....	141
References.....	148

## **Appendix B**

Calculations.....	149
References.....	153

## LIST OF TABLES

### Tables

1.1 Ranking of commercially available detection platforms.....	4
5.1 Voltages and magnetic fields generated by the FMNCP coated bacterium.	124
5.2 Control samples conductivity and average voltage with standard deviation .....	133



## LIST OF FIGURES

Figure 1.1 An example of a metabolic detection platform .....	10
Figure 1.2 Electronic Noise.....	11
Figure 1.3 Steps involved in DNA preparation for PCR.....	14
Figure 1.4 DNA hybridization platform.....	16
Figure 1.5 ELISA based method.....	19
Figure 2.1 FMNCP architecture.....	34
Figure 2.2 The bacterium is mixed with the FMNCP suspension.....	36
Figure 2.3 The lay out of the general design of the detection platform.....	38
Figure 2.4 Structures of macromolecular polymer system.....	40
Figure 2.5 FMNP passing through loop.....	44
Figure 2.6 Graph of equation 4.....	45
Figure 2.7 Graph of equation 5.....	47
Figure 2.8 Graph of equation 7.....	48
Figure 3.1 Reaction mechanism of macromolecular polymer system.....	55
Figure 3.2 HNMR time 0 minutes.....	58
Figure 3.3 HNMR time after 15 minutes.....	59
Figure 3.4 HNMR time after 30 minutes.....	60
Figure 3.5 HNMR final polymer.....	61
Figure 3.6 IR spectroscopy of macromolecular polymer system.....	62
Figure 3.7 Electrospray mass spectrum of macromolecular polymer system.....	63
Figure 4.1 The Langevin equation.....	71

Figure 4.2 The energy of a cobalt nanoparticle in the Earth's field.....	72
Figure 4.3 Structure of capsular polysaccharide.....	77
Figure 4.4 Structures of Rhizobium polysaccharides.....	78
Figure 4.5 Gold nanoparticle suspensions and controls.....	82
Figure 4.6 Fluorescent confocal microcopy images of a dried piece of the gold nanoparticle suspension.....	84
Figure 4.7 Cobalt nanoparticle suspensions.....	85
Figure 4.8 Cobalt nanoparticle suspension with bar magnet.....	86
Figure 4.9 TEM image of dried cobalt nanoparticle suspension.....	88
Figure 4.10 The confocal image of tubules and particles.....	90
Figure 4.11 Antibody evaluation.....	93
Figure 4.12 SEM image of heat fixed Rhizobium trifolii cells.....	95
Figure 4.13 SEM images of nanocomposite and <i>Rhizobium trifolii</i> mix 1.....	97
Figure 4.14 SEM image of nanocomposite and <i>Rhizobium trifolii</i> mix 2.....	98
Figure 4.15 TEM image of <i>Rhizobium trifolii</i> control.....	99
Figure 4.16 TEM image of the nanocomposite and <i>Rhizobium trifolii</i> mix 1.....	100
Figure 4.17 TEM image of the nanocomposite and <i>Rhizobium trifolii</i> mix 2.....	101
Figure 5.1 Graph of voltage induced in coil at different velocities.....	112
Figure 5.2 Graph of average corrected voltage vs. number of beads.....	114
Figure 5.3 Graph of average corrected voltage vs CFUs/mL.....	116
Figure 5.4 Raw data of voltage induced by sample.....	117
Figure 5.5 Graph of all of the nanocomposite and <i>Rhizobium trifolii</i> data samples with line smoothing applied to the data.....	118
Figure 5.6 Induced Voltages by the nanocomposite and <i>Rhizobium trifolii</i> .....	120

Figure 5.7 Graph of the average angle of alignment of the nanoparticles in the earth's field as a function of the number of 3 nm particles.....122

Figure 5.8. Average voltages of the different nanocomposite suspensions.....127

Figure 5.9 Graph of the average corrected voltage vs. the number of cells for *Rhizobium Trifolii* cell.....128

Figure 5.10 Graph of all the corrected voltage data.....129

Figure A1 The toroid shaped magnetic fields of magnetic dipoles of different sizes.....138

Figure A2 The cooperative interaction of the point magnetic dipoles in ferromagnetic materials results in a net magnetic moment.....139

Figure A3 Domain structure of a polycrystalline ferromagnetic material.....143

Figure 4 Domain walls.....144

Figure A5 Hysteresis loop.....145

Images in this dissertation are presented in color

## **LIST OF ABBREVIATIONS**

<b>AMR</b>	<b>anisotropic magnetoresistance</b>
<b>CFU</b>	<b>colony forming units</b>
<b>CPS</b>	<b>capsular polysaccharides</b>
<b>CWG</b>	<b>cell wall glycopolymers</b>
<b>EDC</b>	<b>1-ethyl-3-[3-dimethylaminopropyl] carbodiimide</b>
<b>ELISA</b>	<b>enzyme linked immunosorbent assay</b>
<b>EMF</b>	<b>electromagnetic force</b>
<b>Fab</b>	<b>antibody fragment</b>
<b>FITC</b>	<b>fluorescein isothiocyanate</b>
<b>FMNCP</b>	<b>ferromagnetic nanocomposite particles</b>
<b>FMNP</b>	<b>ferromagnetic nanoparticle</b>
<b>GMR</b>	<b>giant magnetoresistance</b>
<b>IC</b>	<b>integrated circuits</b>
<b>ICMS</b>	<b>intact cell mass spectrometry</b>
<b>IMS</b>	<b>immunomagnetic separation</b>
<b>KLH</b>	<b>keyhole limpet hemocyanin</b>
<b>LPS</b>	<b>lipopolysaccharides</b>
<b>M</b>	<b>magnetization</b>
<b>M<sub>s</sub></b>	<b>saturated magnetization</b>
<b>MALDI-TOF</b>	<b>matrix-assisted laser desorption/ionization time-of-flight</b>
<b>MAR</b>	<b>magnetic assay reader</b>
<b>MR</b>	<b>magnetoresistance</b>

MTJ	magnetic tunnel junction
MWCO	molecular weight cut off
NC	nanocomposite
PBS	phosphate buffered saline
PCR	polymerase chain reaction
RT-PCR	reverse transcriptase polymerase chain reaction
scFV	single chain fragment variable
SELEX	systematic evolution of ligands by exponential enrichment
SEM	scanning electron microscope
SPR	surface plasmon resonance
SQUID	superconducting quantum interference devices
SRM	surface recognition molecules
TEM	tunneling electron microscope
THF	tetrahydrofuran
VOCs	volatile organic compounds

## Chapter One

### Background: Detection of Bacteria

#### Introduction

The detection and protection against of microbial pathogens has always been a challenge. The development of new technologies over the years has brought with it improvements in our ability to detect and prevent infection by microbial pathogens, resulting in dramatic advances in the quality of public health. The first step in the prevention of infection by and spread of microbial pathogens is accurate detection. Our ability to quickly and precisely detect a specific microbial pathogen greatly enhances our ability to take the proper actions, whether it is isolating the cause of food poisoning or the detection of a biological weapons attack.

The development of detection platforms for bioterrorism and biowarfare agents has increased since the 2001 U.S. Postal Service-based anthrax attacks, in which out of a total 22 cases of cutaneous and respiratory anthrax, 5 were fatal [6]. With the average time between exposure and onset of symptoms being 4.5 days and an average of 10 days to get diagnosis from lab tests [6], fast identification of *Bacillus anthracis* spores and treatment with the appropriate antibiotics meant the difference between life and death for postal workers.

While biological attacks are a real threat, one is far more likely to die of food poisoning. It is estimated that in the United State there are approximately 76 million food-borne illnesses, 325,000 hospitalizations, and 5,000 deaths every year [4]. In fact, over the past 20 years, 38% of all publications on detection of

pathogenic bacteria have been concerned with the food industry. Of the remaining publications 18% were clinical, 16% were in water and environment, 26% in other areas, and only about 1% for defense [1]. In 2007 there were over 55 recalls issued by the USDA Food Safety and Inspection Service [3] regarding quality control issues in food.

The fast and accurate detection of pathogens has applications in nearly every aspect of our society, from personal home use to clinical and professional use. Early warning and monitoring systems, biological/chemical response units along with medical diagnostics are the most pressing applications in today's current environment. Areas of work such as emergency response units, front-line healthcare providers, law enforcement, and military personnel, that involve possible exposure to highly pathogenic bacteria demand fast and accurate detection. While speed and accuracy are the most important, they are not the only two features of current detection platforms that are in need of improvement. The other features are sensitivity, portability, robustness, and ease-of-use. Deficiencies in these features have limited the applications of detection platforms. One can envision an ideal detection platform embodying all the above features that would open the door to numerous possible applications.

There is no agreement on a standard for an ideal or preferred detection platform but one that yields results in 5 minutes or less, with an accuracy of 99% or better for all types of error should be close for all types of error. It would have the sensitivity to detect a single cell; it would be a small lightweight personal monitoring device that could be integrated into other personal electronic devices

such as a cell phone. The detection platform would also have the robustness to maintain function in normal day-to-day use in the field as well as in a broad range of environmental conditions especially temperature. Last but not least it would require no user initiative beyond turning it on. The detection platform should detect and alert the user to any new threat or condition autonomously.

While the desirable characteristics of the features of a detection platform may be stated generally, they must be assigned some quantification in order to make some comparisons among platforms and determine their strengths and deficiencies. Table 1.1 gives a list of currently available detection platforms and feature ratings. The relative importance of the features is ranked with speed as most valuable, followed respectively by accuracy, sensitivity, portability, robustness, and ease-of-use. The features are then rated based on a three star scale with three stars being the best (ideal) to zero (doesn't meet any of the criteria). The criteria of the above features and rating are as follows:

Speed is the time required to take and analyze a sample. Zero stars for analysis times greater than 48 hours, one star for greater than 24 hours, two stars for 24 hours or less and three stars for 5 minutes or less. Diseases such as anthrax can kill within 48 hr, with flu like first stage symptoms, which make diagnosis difficult, and rapidly progress to stage two lasting about 24 hours and ending in death [42]. Immediate diagnosis and treatment in the first stage are key to survival, treatment after the onset of second stage symptoms has little to no effect on the mortality of the victims.



Table 1.1 Ranking of commercially available detection platforms.

<b>Platform</b>	<b>VITEK2</b>	<b>RAZOR EX</b>	<b>RAPTOR</b>	<b>Spreeta</b>	<b>Reveal</b>
<b>Type</b>	Biochemical	PCR	Immunoglobins	Immunoglobins	Immunoglobins
<b>Speed</b>	★ ★	★ ★	★ ★	★ ★	★ ★
<b>Accuracy</b>	★ ★	★ ★	★ ★	N/A	★ ★
<b>Sensitivity</b>					
<b>Portability</b>	★	★ ★	★ ★	★ ★	★ ★
<b>Robustness</b>		★ ★	★ ★	★	★ ★
<b>Ease of use</b>	★	★		★	★ ★

Accuracy will be the percentage of total pathogenic samples correctly identified. One star for 70% or better, two stars for 80% or better and three stars for 99% and better.

The sensitivity is the limit of detection for the platform. Three stars for detection of 1 cell, two stars for detection of 10 or fewer cells and one star for detection of 100 cells or fewer. Low limits of detection are needed because an infectious dose of pathogenic bacteria such as *Yersinia pestis* can be less than 10 organisms [44]. The “reality” is that it really only takes one viable organism to take root to cause an infection. Another reason for low detection limits is that samples with low concentrations of the pathogen are the norm.

For the robustness, three stars for platforms that can function in the normal day-to-day use in the field – the same that one would expect of a cell phone. They should be shock and impact resistant as well as functioning in a broad range of environmental conditions like temperature and humidity. Two stars if it is shock and impact resistant but does not function in varying environmental conditions and vice-versa. One star if it can function in the field.

For the portability criteria, three stars for a personal monitoring device that can be integrated into other personal electronic devices such as a cell phone. Two stars if it can be moved around in the field and one star if it cannot be moved.

For ease-of-use, three stars indicate that the platform requires no user initiative, no sampling, no sample preparation yet the platform still detects and alerts. Two stars, the platform requires user initiative and sampling but no

preparation. One star, the platform requires user initiative and sampling with minimal sample preparation (such as pipetting and mixing).

Now that we have outlined an ideal detector let us take it one step further. Here we will show you how and why such a device is needed and the impact it would have on the world. Imagine now that everyone has this technology integrated into their cell phones, and is constantly monitoring their environment. While this platform can function on its own, it will actually be connected to a larger central monitoring system. At the moment of detection a call would be sent out from the detector to the central monitoring system, as well as notifying the user. The central monitoring system can then be in contact (operator, or text message) with the exposed individual, giving instructions and collecting information. Even without contact with the exposed individual a wealth of information can be obtained, such as location (past and present) by GPS, as well as the individual that has been exposed via phone registers. Once an individual is identified a database can be mined such as DMV records. At the same time that information is being collected, the appropriate response teams can be notified and begin mobilizing. The central monitoring system will then coordinate the response by relaying information as to the location and number of possible exposed individuals. This type of system would drastically improve our ability to stop the spread of disease and improve the chances of survival of the exposed. Such a system would allow the global monitoring of the origin and progression of diseases.

Such a system brings up privacy and tampering concerns. The ethical and moral implications of technology must not be forgotten. While we may suggest the possibility that everyone would carry such a device, the choice should be left up to the individual. The use of such detection platforms may not find a place in the hands of the general public but only those who have a more realistic chance of exposure, such as first responders and military personnel. The device could also be employed in much the same way that surveillance cameras are on street corners, hospital, and government buildings. While technology has provided many improvements in our lives we must not allow it to be used to infringe upon our liberty and freedom. With all new technologies and scientific advancements there will always be debate over how they will be used. As scientists we strive to better understand the world around us with hopes of improving the lives of our fellow mankind. The knowledge that science gives us allows us the potential to do great things both good and bad, we must all choose what we do with our knowledge. We must also look to the future and think about what implications that our actions will have in the future.

New advances in technology in all fields of science have yielded a plethora of detection platforms of every possible combination and the economics of mass manufacturing has brought them within an almost affordable price range. Traditional methods of detection that rely on cultivation and biochemical assays can take anywhere from 24 hours to 1 month [7, 8]. While these methods are reliable, highly selective and sensitive, they are not capable of yielding rapid or real-time detection. Rapid and real-time detection is a relative term in defining a

detection platform's performance, often only the length of time for an assay is given excluding the time for sample processing, purification, and enrichment. These steps not only increase the time it takes to get results, but in many cases require a laboratory environment to operate which is neither economical nor practical for field use and does not allow for personal monitoring.

Detection platforms are classified by one of two means, the first is the type of identifying markers that are characteristic of a particular pathogen such as its DNA or select surface antigens. The second classification is based on the transducer that measures the changes in the identifier elements, such as optical, electrochemical, and mass characteristics. The second classification is not ideal and leads confusion due to the numerous types of transducers. For simplicity I will use classification based on identifying elements, which are divided into four major groups: metabolic, genetic, surface recognition, and other. Classifying by identifying elements gives a better understanding of what is available for detection and how best to detect it. As mentioned before, there are many features that are demanded of these detection platforms. They must have speed, accuracy, sensitivity, portability, robustness, and ease to use.

The ability to determine the viability of the cells is important especially for validation testing. In the next section I will discuss some of the different detection platform technologies, design, and function, along with their challenges. I will also cover the major types of detection methods for each of the four areas: metabolic, genetic, surface recognition, and other features of the pathogen cells.

## **Detection Platforms**

Biochemical detection platforms rely on the metabolic byproducts and enzymatic activities that are associated with a specific bacterium (figure 1.1). Many of the assays performed in traditional laboratory detection protocols have been miniaturized, automated, and placed on cards. This allows for several assays to be run simultaneously with small samples and greatly reduces the time for identification. One such platform is the VITEK2 which measures the fluorescence of probes on the card and uses a pattern recognition database to identify bacteria [9].

Another biochemical based platform is the electronic nose. This technology analyzes the specific volatile organic compounds (VOCs) produced by a bacterium, using complex pattern recognition software [8]. Electronic noses are made up of arrays of conducting polymers or semi-conducting materials which are coated or doped with chemical or biological reactants (figure 1.2). Interaction of the analyte with the array causes a change in the resistance of the conduction polymers or semi-conducting materials, which is then analyzed and compared to a database [10, 11]. Other methods of analysis include mass spectrometry, infrared spectroscopy, and gas chromatography [12]. An obvious drawback to these platforms is that they require a pure isolated sample of reasonable concentration. A mixed culture can produce the same biochemical profile as a single bacterium, as none of the biochemical measurements by themselves can specifically identify the bacterial strain.

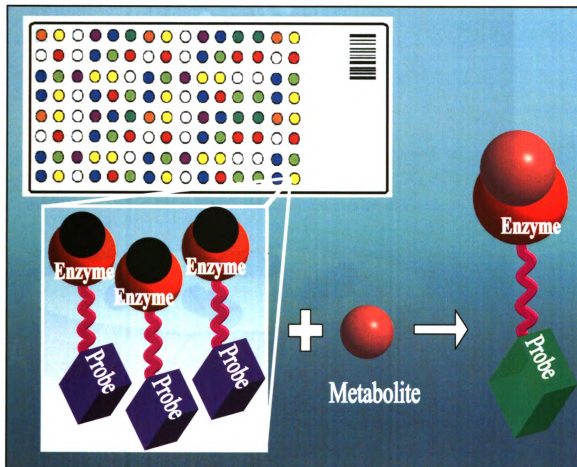


Figure 1.1 An example of a metabolic detection platform each spot on the chip represents a different metabolic assay. The white box show an example of an assay with enzyme linked with a fluorescent probe. Once the sample is added to the card, the metabolite reacts with the enzyme resulting in a change in the fluorescent probe. The card is then analyzed by the instrument and a metabolic profile is generated and compared with standards for identification.

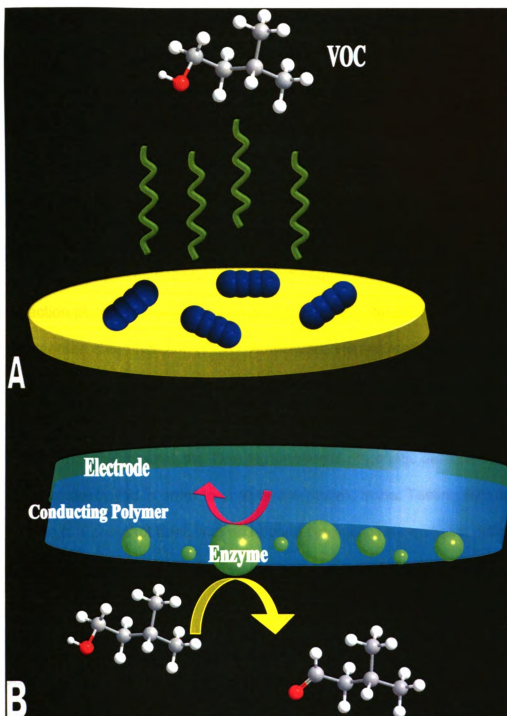


Figure 1.2 Electronic Nose. In A) isolated bacteria produce VOCs when grown on specific media. B) The VOCs react with the enzymes (lime) which results in a change in the resistance of the conduction polymer (blue), which is measured by the attached electrode (green).



Another biochemical detection platform is based on electrochemical measurements of enzyme linked electrodes. Detection is typically based on the inhibition of the enzyme by a bacterial toxin resulting in change of the electrochemical measurements. One example is the acetylcholinesterase-based electrode biosensor that is used to detect anatoxin-a, a toxin produced by certain cyanobacteria [13].

Detection platforms that are based on genetic material identify pathogens by detecting species specific nucleic acid sequences of DNA or RNA. All genetic detection platforms use some form of amplification, whether by culturing or the polymerase chain reaction (PCR). Amplification is required due to the low concentration of analyte typically found in a sample. The exceptions are cases where large numbers of cells can be isolated from a sample to provide enough genetic material for analysis. One big weakness of genetic detection is that the cells are destroyed in order to analyze the nucleic acids. Testing with limited sample is a one shot deal, with no second chances. This makes it difficult to determine the pathogen's viability if at all and impossible to do confirmation testing.

The basic strategy of genetic detection is the hybridization of species specific nucleic acid sequences with complementary probe sequences. This basic strategy makes use of the complementary probe sequences that are either free in solution or immobilized. Genetic detection platforms that make use of free complimentary probe sequences make use of polymerase chain reaction (PCR) methods. There are several different PCR methods that can be used in a

platform but only real time PCR techniques offer the speed that is needed for rapid detection. While not being a true real time detection platform, it is near real time. There are different real time PCR techniques of varying complexity and sensitivity, but all are based on the same principle of monitoring the amplification of species specific nucleic acid sequences typically by the fluorescence emissions of a fluorophore, which changes through specific or nonspecific interactions with the amplified nucleic acids [14]. Other methods of detection include electrophoresis of the amplified sequences and hybridization with immobilized probes.

Another technique that was developed to determine cell viability is reverse transcriptase PCR (RT-PCR), in which the RNA of the target pathogen is used. This is because RNA is rapidly degraded by endogenous RNases and would only be present if the cells were viable. PCR is a powerful diagnostic tool, and with the aid of automation it can efficiently and accurately analyze large numbers of samples in a clinical lab setting [15]. In many cases, however, it is not suitable for field work as it requires a laboratory environment where quality control can be maintained and trained personnel can quickly perform the many preparation procedures needed before sample analysis. In order for PCR techniques to achieve a high level of sensitivity and specificity, it requires very pure and clean samples, which lengthens the time it takes to get results (Figure 1.3). Sample preparation procedures are a challenge to all detection platforms and will be addressed in a following section. There are portable PCR detection platforms available, one such platform is the RAZOR EX system made by Idaho

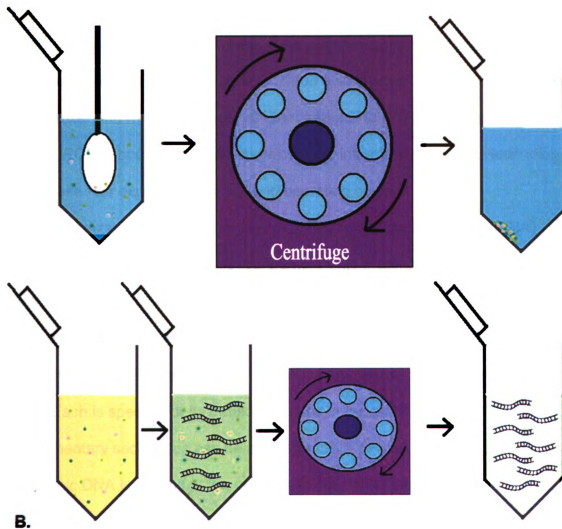


Figure 1.3 Steps involved in a DNA preparation for PCR. In step A the sample is collected, and the cells are isolated and concentrated. In B, the cells are resuspended and lysed to extract the DNA and the DNA is isolated. Once the DNA has been isolated, it can then be used for PCR. Preparation and isolation procedures vary depending on the sample matrix. Typical laboratory procedures require a minimum of 60 min.

Technology Inc. The RAZOR EX system offers near real time detections with results within 30 minutes and detection limits in the range of 1000 cfu/ml [16]. The 30 minutes needed for detection do not include the 5 minute minimum sample preparation time for powders. Other sample matrices require further enrichment and purification steps, which then also involve other equipment such as a vortexer and microcentrifuge. Another setback to PCR based detection is the cost. PCR is both equipment, chemical, and information intensive technology which makes for expensive start up and operating costs.

Hybridization platforms are made up of single stranded DNA (ssDNA) complementary probe sequences immobilized onto a matrix which is suitable for detection of hybridization [11]. Highly sensitive transducers detect hybridization of complementary pathogenic DNA by changes in mass, electrical charge, and optical properties (Figure 1.4). The ssDNA is immobilized on chips, arrays, and beads. Each is specific for its transducer used in the platform. Hybridization of complementary sequences can be done with DNA or RNA. While direct detection of genomic DNA is difficult at low concentrations, RNA has multiple transcripts that allows for lower detection limits. Often, hybridization methods are coupled with PCR to increase the number of targets that can be analyzed at the same time, and to increase sensitivity and specificity [17]. Hybridization methods suffer setbacks in ease-of-use and robustness similar to PCR in that highly pure and clean samples are needed as well as properly designed probes to limit nonspecific binding. The design of probes necessitates large databases,

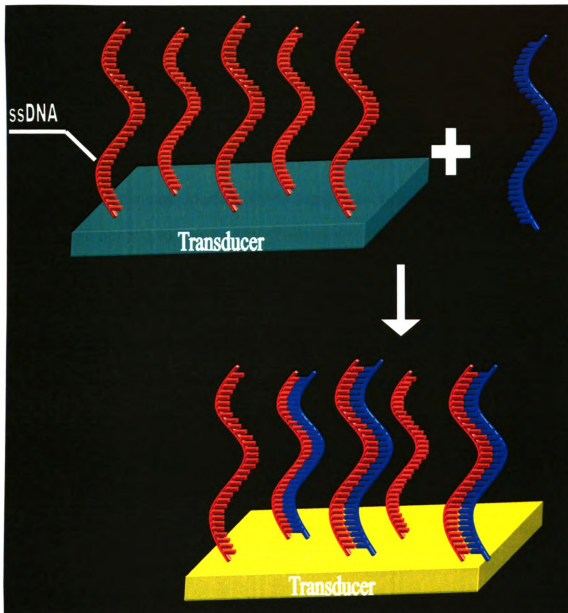


Figure 1.4 DNA hybridization platform of single stranded DNA (ssDNA red) is immobilized onto a sensitive transducer which sends a signal upon hybridization of complementary pathogenic DNA (blue).

screening and validation of probes. It is the same for PCR primers and probes; in both cases the results are both time consuming and costly.

Surface recognition based detection platforms make use of molecular structures that have a high affinity for specific molecular topological structures. A prime example of surface recognition molecules is immunoglobins (antibodies). Immunoglobins have the ability to bind to specific molecular topological structures (antigens) on the surface of pathogens. A signal is generated upon binding of the antibody and antigen, with the signal type dependent upon the transducer and the method used. These signals can be optical, electrochemical, mass, and magnetic, to name a few. There are several different methods employed by various platforms, but are typically used in one of two ways.

The first use immobilized antibodies on a transducer surface, which can be piezoelectric, nanoelectromechanical and thin metal film. Piezoelectric and nanoelectromechanical transducers are typically cantilevers, which are very sensitive to small changes in mass. These cantilevers have been mainly used for detection of proteins, DNA and small molecules as well as single cells [20, 21]. One shortcoming besides the high cost of fabrication is the lack of robustness of the sensor – overloading the cantilevers can cause them to break [22]. Thin metal film works by surface plasmon resonance (SPR), which measures changes in refractive index of a thin metal film with antibodies immobilized on the surface. Binding of the pathogen to the antibody causes a change in the refractive index of the thin metal film [23]. There are commercial SPR instruments and even a portable kit, the “Spreeta”, made by Texas Instruments. The Spreeta system

yields results within 30 minutes and has been shown to have a sensitivity of  $10^2$  to  $10^3$  colony forming units (CFU)/mL for *E. Coli* O157:H7.

The second and most popular method of using antibodies is a sandwich technique. Based on the classic enzyme-linked immunosorbent assay (ELISA), (figure 1.5) this method also makes use of immobilized antibodies on a surface that binds the pathogen, then a probe labeled secondary antibody binds to the pathogen. The probe on the secondary antibody signals or transduces a signal which is picked up by the detector. The type of probe depends on the detection platform; in some cases a third antibody is used. The probes can be fluorophors, optical and magnetic nanoparticles, and enzymes. Common and inexpensive types of this detector are lateral flow test strips which rely on visual detection. Neogen's Reveal lateral flow pathogen test is a good example of these types of test [40]. While they yield quick results they have poor sensitivity and otherwise require pre-enrichment of the sample.

One portable commercially available sandwich-based platform detection unit is the RAPTOR made by Research International, Inc. The RAPTOR uses immobilized antibodies on the surface of an optical wave guide. Once the pathogen binds to the surface, a secondary antibody with a fluorescent probe can subsequently bind and the fluorescence can be measured to detect the pathogen [26]. The RAPTOR unit has an assay time of 10 to 15 minutes and a detection limit of 30 CFU/mL for anthrax spores in water [27].

Advances in sensor and detector technologies have increased the sensitivity of immunological detection. Antibody technology has also made

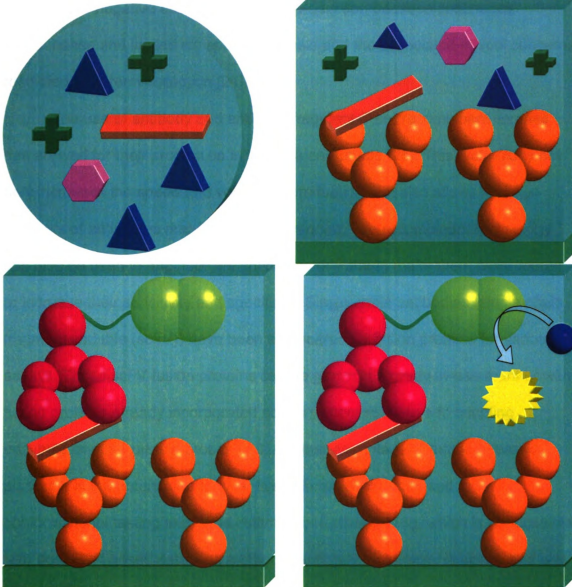


Figure 1.5 ELISA based method. Sample is added to immobilized antibodies (orange) then it is washed to remove unbound sample. Next a secondary antibody (pink) linked to a enzyme (lime) is added, then washed again to remove unbound antibody. Next the enzyme substrate (blue) is added and the product is produced signaling detection.



advances in recent years resolving many criticisms. New production techniques eliminate the need for live animal and hybridoma cultures to produce antibodies, which was a negative aspect of antibody production because continuous maintenance and limited life span of animals and the associated ethical concerns restricted long-term collection [24].

The use of antibody and antibody fragment (Fab) recombinant libraries has allowed for their production in bacteria and phage [25]. This technology not only increases the speed and volume of production, but also allows for large numbers of antibodies and Fabs to be screened. The recombinant technology can also be used to engineer the antibodies or Fabs to make them more robust or increase their sensitivity and specificity. Single chain antibodies (single chain fragment variable (scFV)) have been engineered as fusion proteins for various assays. These scFV fusion proteins can be grown in a ready-to-use manner with fusion proteins already incorporated so it is unnecessary to add coupling enzymes or other protein probes to it. Another advantage to antibody based platforms is the potential to recover live cells which can be used for conformational testing and/or be cultured for further testing, which is not possible with post PCR based detection methods. Antibody technology is sound and well documented and continues to be developed.

Other surface recognition molecules that can be used are aptamers. Aptamers are small single stranded DNA or RNA molecules that act as ligands to bind to non-nucleic acid targets [8]. Aptamers are used in detection platforms in much the same way that antibodies are used to bind a specific target. Aptamers

have some notable advantages over antibodies, most importantly that they are chemically synthesized, which allows them to be made and modified on demand. Aptamers are discovered using a high throughput selection process called systematic evolution of ligands by exponential enrichment (SELEX) [19]. This technique allows one to screen a large library of aptamers against a specific target and select for those aptamers with high affinity for the targets. Some aptamers used for pathogen detection range in length from 17 to 78 nucleotides long [18]. Aptamers do not remain linear polymer chains but form secondary three dimensional structures. Aptamers may replace antibodies in some applications because of their structural and functional robustness. While aptamers have been shown to perform well in laboratory testing, they have yet to be fully tested. They must be tested in field conditions where sample matrixes could contain inhibitors. This technology is still under development but holds promise.

Other detection platforms take various forms such as tissue or cell based detection platforms, and mass spectrometry. One tissue or cell based detection platform makes use of B-lymphocytes that have been engineered to emit light when they come in contact with their target pathogen [28]. The B-lymphocytes are engineered to express a pathogen specific membrane bound antibody along with calcium sensitive bioluminescent protein. Binding of antibodies with the pathogen increases intracellular calcium causing the protein to luminesce. One obvious problem with this is the amount of time and money that is required in the upkeep of the cell line as well as the luminometer needed to take measurements.

There are several mass spectrometry techniques that are used for pathogen detection, with matrix-assisted laser desorption/ionization time-of-flight (MALDI-TOF) mass spectrometry topping the list. MALDI-TOF popularity is due to its ability to do intact cell mass spectrometry (ICMS) for direct profiling of pathogens [43], with little sample preparation. The ICMS spectrum that is generated gives a profile of the protein composition of the pathogen. This spectral fingerprint can then be compared with reference spectra as well as protein databases for identification. Other pathogen specific biomarkers besides proteins can be used in mass spectrometry detection platforms such as nucleic acid sequences, metabolites, lipids, and polysaccharides. In all cases data bases must be made for profile comparison. The data bases contain spectral profiles from known pathogens. Mass spectrometry techniques that do not use ICMS typically require lengthy sample preparation and/or chromatographic separation. One drawback is the need for concentrated clean samples. The more complex the sample matrix the higher the limit of detection. Complex sample matrices also require more complex identification software [8]. As with most chemical spectrometry, instrument cost is steep and is restricted to laboratory use, due to the instrument size.

### **Challenges Shared by All Detection Platforms**

The challenges for detection platforms are many. The greatest of the difficulties is sensitivity; the detection platform must be able to detect low concentrations of the target pathogen. High sensitivity can be a double-edged sword: while it allows for detection of low concentrations of the analyte, at the

same time, it increases their sensitivity to inhibitors as well, and requires very clean or pure samples. Such is the case with PCR based detection platforms. Most detection platforms can analyze powder samples (e.g, spores) with little or no preparation, but complex matrix samples such as blood, stool, mucus, soil, food stocks, and water all contain inhibitors and competing agents. This makes sensitive and specific detection difficult and creates issues with reproducibility as well [8]. Another problem with smaller detectors is that the sample volume decreases as well. This can limit the platform's detection limit in low pathogen concentrations. Specificity is important as well – the ability to specifically identify the target pathogen from the background and limit false-positives and negatives. Pathogens must be isolated and purified from the sample matrix before analysis, and this slows the time it takes to detect. There are several methods for processing samples, many of which can only be done in a laboratory setting.

Another challenge is making a user-friendly device, which requires little-to-no training. Many manufacturers have made automated platforms which eliminate the need for manual preparation. The obstacles to these features are reduced portability and high cost - not just the initial cost, but also the cost of continual operation. Mass production and the savings generated by an economy of scale will reduce prices but not until one platform proves its utility and has the features discussed in Section 1.

### **The Potential for Magnetic Detection**

Ferromagnetic nanoparticles have a wide range of applications from magnetic memory storage devices to biomedical probes for MRI. This is due to

the unique magnetic properties of ferromagnetic nanoparticles, which are considerably different from that of their bulk material. Further discussion on properties of ferromagnetic nanoparticles can be found in Chapter 2.

Immunomagnetic separation (IMS) is used extensively in the separation and enrichment techniques used in many detection platforms [30, 31].

Immunomagnetic separation uses micron or nano size ferromagnetic particles that have been functionalized with antibodies. When mixed with the target bacteria and placed in a magnetic field the particles will be pulled to the magnet along with whatever is attached to the antibody. IMS greatly reduces detection times by easily removing bacteria from complex heterogeneous mixtures [32]. While several groups have designed sensors for the detection of ferromagnetic nanoparticles [33, 34, 35, 36, 37, 38] and have proposed possible biosensing applications, there has been relatively little work done on the use of ferromagnetic particles for detection of pathogens. This may be mainly because of the limited use/exposure of magnetic sensing instrumentation in biological sciences, leaving many unaware of its great potential.

Several groups have been able to detect ferromagnetic nanoparticles using different magnetic field sensors. The types of magnetic field sensors used are magnetoresistance, Hall Effect sensors, superconducting quantum interference devices (SQUID) and pick up coil devices. SQUID is used in a broad range of applications from characterizing properties of a material to biomedical measurements such as magnetocardiographs. SQUID is a very sensitive type of magnetic sensor with detection limits demonstrated as low as  $10^{-17}$  T [45]. While

SQUID are capable of magnetic characterization of materials as well as detection of FMPs, the instrument is far too large, and its requirement of liquid helium or nitrogen (for high temperature SQUID) is impractical for portable detection platforms.

Magnetoresistance (MR) is a change in a material's resistance in response to an external magnetic field. There are many MR materials and devices such as anisotropic magnetoresistance (AMR), magnetic tunnel junction (MTJ) and giant magnetoresistive (GMR) sensors [39]. Researchers have developed a GMR sensor capable of detecting 14 superparamagnetic magnetite (16 nm) nanoparticles at room temperature [46].

Hall Effect sensors measure the transverse voltage caused by a magnetic field on a current carrying conductor. Japanese researchers have fabricated Hall sensors for use in biosensor arrays that can detect a single superparamagnetic nanoparticle (200 nm) [47]. Both of the above sensors are highly sensitive microfabricated magnetic field sensors. These magnetic field sensors are capable of detecting single ferromagnetic nanoparticles, and are designed to be used in a chip based format. These platforms have a static design wherein the particles must be immobilized on the sensor, which limits the throughput of the detection platform. These platforms have other issues that must be dealt with such as removal of nonbonding particles and nonspecific interacting FMPs.

Pick up coils, also called induction coils, are based on Faraday's Law of induction, in which a voltage is induced in a loop by a magnet moving through it. There are many types of sensors that make use of coils, and vary in their design

and complexity depending on the method. Researchers have developed a pick up coil sensor capable of detecting 7 ng of 25nm FMPs by AC susceptibility measurements [37]. Pick up coils have an advantage over other sensors in that they are simple and robust making them ideal for sensors in detection platforms. While the sensors are capable of detecting single FMPs they need to be worked into detection platforms that are able to detect and discriminate between bound and non-bound FMPs. One commercially available magnetic detector is the Magnetic Assay Reader (MAR) by MagnaBioSciences [41]. MAR is a lateral flow type test with superparamagnetic nanoparticles to label the antibodies. The MAR uses magnetic field sensors in a pattern called a gradiometer, which move along the strip. Once the target is immobilized, it can detect the change in the magnetic field. While this detection platform offers greater sensitivity than other lateral flow detectors its detection limit is still much higher than what is needed.

Ferromagnetic nanoparticles have many advantages over other molecular tags or labels. Methods used for the detection of ferromagnetic nanoparticles are passive (non-destructive). That is detection does not damage the FMPs or the sample, unlike fluorescence detection methods that use damaging UV light. The ferromagnetic nanoparticles are chemically stable and maintain their magnetic signal over time. They do not have the problems of optical systems of bleaching, and quenching. Magnetic detection systems of ferromagnetic nanoparticle can offer more quantitative measurements than optical systems. The magnetic properties of ferromagnetic nanoparticles are proportional to the total amount of material. Measurements based on magnetization are proportional to the

magnetic moment per unit volume, and measure the total volume, not just the surfaces as in other detection systems. Another major advantage of magnetic sensing and measurement is that it is a nondestructive method of testing and evaluating of samples.

As mentioned before the true challenge for all detection platforms is speed. The time from the moment a sample is taken to the point of detection is crucial. We will show that our detection platforms can perform at the desired speeds, and are capable of embodying all of the features demanded of such a device. Accuracy is also a challenge that must be balanced with speed. We must keep in mind that there will always be trade offs between speed and accuracy. With infinite time one could know with absolute certainty, but time is not infinite and decisions must be made immediately, and actions taken.



## REFERENCES

1. O. Lazcka, F.J. Del Campo, F.X. Munoz, Pathogen Detection: A perspective of traditional methods and biosensors. *Biosensors and Bioelectronics* Vol:22, pg:1205-1217, 2007.
2. <http://www.state.gov/t/ac/trt/4718.htm#treaty> Convention on the Prohibition of the Development, Production and Stockpiling of Bacteriological (Biological) and Toxin Weapons and on Their Destruction 2008.
3. [http://www.fsis.usda.gov/Fsis\\_Recalls/Recall\\_Case\\_Archive/index.asp](http://www.fsis.usda.gov/Fsis_Recalls/Recall_Case_Archive/index.asp) USDA Food Safety and Inspection Service Recall case Archive 2007.
4. P.S. Mead, L. Slutsker, V. Dietz, L.F. McCaig, J.S. Bresee, C. Shapiro, P.M. Griffin, R.V. Tauxe, Food-Related Illness and Death in the United States, *Journal of Environmental Health*. Vol:62, Issue:7, Pg:9-18, 2000
5. J. Guarner<sup>\*</sup>, J.A. Jernigan, W.J. Shieh, K. Tatti , L.M. Flannagan, D.S. Stephens, T. Popovic, D.A. Ashford, B.A. Perkins and S.R. Zaki, Pathology and Pathogenesis of bioterrorism-related inhalational Anthrax *American Journal of Pathology*, Vol:163, No:2, 2003.
6. National Anthrax Epidemiologic Investigation Team, Investigation of Bioterrorism-related anthrax, United States 2001: epidemiologic findings. *Emerging Infectious Diseases* Vol:8 No:10, 2002
7. P.R. Murray, E.J. Baron, J.H. Jorgensen, M.L. Landry, M.A. Pfaller. *Manual of clinical microbiology* 9<sup>th</sup> edition, ASM Press, 2007.
8. D.V. Lim, J.M. Simpson, E.A. Kearns, M.F. Kramer. Current and developing technologies for monitoring agents of bioterrorism and biowarfare. *Clinical Microbiology Reviews*, Vol:18, No:4, pg: 583-607, 2005
9. [www.biomeriwx-usa.com](http://www.biomeriwx-usa.com) 2008.
10. A.K. Deisingh, M. Thompson, Biosensors for the detection of bacteria, *Can. J. Microbiol.* Vol:50(2) pg:69–77, 2004.
11. K. Arora, S. Chand, B.D. Malhotra, Recent developments in bio-molecular electronic techniques for food pathogens. *Analytica Chimica Acta*, Vol:568, issues:1-2, pg:259-274, 2006.
12. F. Röck, N. Barsan, U. Weimar, Electronic Nose: Current Status and Future Trends. *Chem. Rev.* Vol:108 (2), pg:705–725, 2008.

13. F. Villatte, H. Schulze, R. D. Schmid, T. T. Bachmann, A disposable acetylcholinesterase-based electrode biosensor to detect anatoxin-a(s) in water. *Anal Bioanal Chem*, Vol:372 pg:322–326, 2002.
14. P.T. Monis, S. Giglio, Nucleic acid amplification-based techniques for pathogen detection and identification. *Infection, Genetics and Evolution* Vol:6(1) pg:2-12, 2006.
15. M.G. Morshed, M.K. Lee, D. Jorgensen, J.L. Isaac-Renton, Molecular methods used in clinical laboratory: prospects and pitfalls. *FEMS IMMUNOLOGY AND MEDICAL MICROBIOLOGY*, Vol:49(2) pg:184-191, 2007.
16. Idaho technology Inc. 390 Wakara Way, Salt Lake City, Utah 84108, USA
17. F. Lucarelli, S. Tombelli, M. Minunni, G. Marrazza, M. Mascini, Electrochemical and piezoelectric DNA biosensors for hybridisation detection. *Analytica Chimica Acta*, Vol:609, issues:2, pg:139-159, 2008.
18. N. Fischer, T.M. Tarasow, J.B.H. Tok, Aptasensors for biosecurity applications. *Current Opinion in Chemical Biology* Vol:11, Issue:3, pg:316-328, 2007.
19. D.H.J. Bunka, P.G. Stockley, Aptamers come of age – at Last. *Nature Reviews Microbiology* Vol:4, pg:588-596, 2006.
20. A. Johansson, G. Blagoi, A. Boisen, Polymeric cantilever-based biosensors with integrated readout. *Applied Physics Letters*, Vol:89(17) pg:3505.1-3505.3 2006
21. B. Ilic, D. Czaplewski, M. Zalalutdinov, single cell detection with micromechanical oscillator. *Journal of Vacuum Science & Technology B*, Vol:19(6) pg:2825-2828, 2001.
22. A.K. Gupta, P.R. Nair, D. Akin, Anomalous resonance in a nanomechanical biosensor. *PNSA*, Vol:103 Issue:36 pg:13362-13367, 2006.
23. J. Waswa, J. Irudayaraj, C. DebRoy, Direct detection of E. Coli O157:H7 in selected food systems by a surface plasmon resonance biosensor. *LWT-Food Science and Technology*, Vol:40 Issue:2 pg:187-192 2007.
24. S.S. Iqbal, M.W. Mayo, J.G. Bruno, B.V. Bronk, C.A. Batt, J.P. Chambers, A review of molecular recognition technologies for detection of biological threat agents. *Biosensors & Bioelectronics* Vol:15, pg:549–578, 2000.

25. B. Krebs, R. Rauchenberger, R. Silke, et al. High-throughput generation and engineering of recombinant human antibodies. *Journal Of Immunological Methods*, Vol:254 Issue:1-2 pg:67-84 2001.
26. C.C. Jung, E.W. Saaski, D.A. McCrae, B.M. Lingerfelt, G.P. Anderson, RAPTOR: a fluoroimmunoassay-based fiber optic sensor for detection of biological threats. *IEEE Sensors Journal*, Vol:3 Issue:4 pg:352-360, 2003.
27. Research international, Inc 17161 Beaton Rd SE, WA 98272-1034 360-805-4930 <http://www.resrchintl.com/>, (2008)
28. T.H. Rider, M.S. Petrovick, F.E. Nargi, et al. A B Cell-Based Sensor for Rapid Identification of Pathogens, *SCIENCE*, Vol:301 Issue:5630 pg:213-215, 2003.
29. M. Magnani, L. Galluzzi, I.J. Bruce, The use of magnetic nanoparticles in the development of new molecular detection systems. *Journal of Nanoscience and Nanotechnology*, Vol:6 Issue:8 pg:2302-2311, 2006,
30. I.M. Hsing, Y. Xu, W.T. Zhao, micro- and Nano- magnetic particles for applications in biosensing. *Electroanalysis* Vol:19 Issue:7-8 pg:755-768, 2007.
31. H.W. Gu, K.M. Xu, C.J. Xu et al. Biofunctional magnetic nanoparticles for protein separation and pathogen detection. *Chemical Communications*, Vol:9 pg:941-949, 2006.
32. D. Horak, M. Babic, H. Mackova, et al. Preparation and properties of magnetic nano- and micronsized particles for biological and environmental separations. *Journal of Separation Science* Vol:30 Issue:11 pg:1751-1772, 2007.
33. D.L. Graham, H.A. Ferreira, P.P. Freitas, Magnetoresistive -based biosensors and biochips. *Trends in Biotechnology*, Vol:22 Issue:9 pg:455-462, 2004.
34. L. Ejlsing, M.F. Hansen, A.K. Menon, et al. Planar hall effect sensor for magnetic micro- and nanobead detection. *Applied Physics Letters*, Vol:84 Issue:23 pg:4729-4731, 2004.
35. D.R. Baselt, G.U. Lee, M. Natesan, et al. A biosensor based on magnetoresistance technology. *Biosensors & Bioelectronics*, Vol:13 Issue:7-8 pg:731-739, 1998.

36. G.X. Li, V. Joshi, R.L. White, et al. Detection of single micron sized magnetic beads and magnetic nanoparticles using spin valve sensors for biological applications. *Journal of Applied Physics* Vol:93 Issue:10 pg:7557-7559, 2003.
37. T.Q. Yang, M. Abe, K. Horiguchi, K. Enpuku, Detection of magnetic nanoparticles with ac susceptibility measurements. *Physica C: Superconductivity*, Vol:412-414, part 2 pg:1496-1500, 2004.
38. G. Mihajlovic, P. Xiong, S. von Molnar, et al. Submicrometer hall sensor for Superparamagnetic nanoparticle detection. *IEEE Transactions on Magnetics*, Vol:43 Issue:6 pg:2400-2402, 2007.
39. S. Parkin, X. Jiang, C. Kaiser, et al. Magnetically engineered Spintronic sensors and memory. *Proceedings of the IEEE*, Vol:91 Issue:5 pg:661-680, 2003.
40. Neogen Corporation, 620 Lesher Place, Lansing, MI 48912
41. MagnaBioSciences a Quantum Design Company 6325 Lusk Boulevard, San Diego, CA 92121-3733
42. S. Shafazand, R. Doyle, S. Ruoss, et al. Inhalation Anthrax: Epidemiology, Diagnosis, and management. *CHEST*, Vol:116 Issue:5 pg:1369-1376, 1999.
43. P. Lasch, H. Nattermann, M. Erhard, et al. MALDI-TOF Mass Spectrometry compatible inactivation method for highly pathogenic microbial cells and spores. *Analytical Chemistry*, Vol:80 Issue:6 pg:2026-2034, 2008.
44. M.B. Prentice, L. Rahalison, Plague. *Lancet* vol:369 pg:1196-1207, 2007.
45. R.L. Fagaly, Superconducting Quantum interference device instruments and applications. *Review of Scientific Instruments*, Vol:77(10) pg:101101-101101-45, 2006.
46. S.X. Wang, G. Li, Advances in giant magnetoresistance biosensors with magnetic nanoparticle Tags: review and outlook. *IEEE Transactions on Magnetics*, Vol:44 No:7 pg:1687-1702, 2008.
47. Y. Kumagai, Y. Imai, M. Abe, et al. Sensitivity dependence of hall biosensor arrays with the position of superparamagnetic beads on their active regions. *Journal of Applied Physics* Vol:103, Issue:7, pg:07A309 2008.

## **Chapter 2**

### **The Big Idea: Magnetic Modification of Bacteria**

#### **Introduction**

The overarching goal of this project is to design and fabricate a functional pathogen detection platform based on basic physical laws that uses simple electronic, chemical and biological technologies, and is capable of the real time detection of a single bacterium. We first begin with a single bacterium and build up our methodology and detection platform around it – a more detailed discussion on the specific features, concepts, and components of the detection platform will be presented in the following sections.

Real time detection of a single bacterium is not an easy task. There is very little in the way of measurable or inducible signals that would allow detection, let alone be specific enough for species identification. The obvious solution then is to add a signal to the bacterium. This can be accomplished through numerous probes of varying design. The difficulty is finding a probe that increases the signal of a single bacterium sufficiently to allow detection over the background. Magnetotactic bacteria can produce magnetic fields that are 20 to 30 times that of the earth's magnetic field ( $50\ \mu\text{T}$ ) [1], and some with field as high as 0.6 T [2]. There are several types of magnetic sensors with sensitivities far below those needed for the detection of magnetotactic bacteria ranging from nT to fT. In our discussion of ferromagnetic nanoparticles in chapter 4 we will see that cobalt nanoparticles can be made that are smaller but produce fields equal to those of magnetotactic bacteria. Putting this all together it becomes evident that detection

of a single bacterium is possible with the use of magnetic probes and a magnetic sensor.

Our strategy is to make use of the large magnetic field produced by ferromagnetic nanoparticles to detect the bacteria. In our strategy, ferromagnetic nanocomposite particles (FMNCP) (figure 2.1) that contain surface recognition elements that can detect and bind to specific bacterial cell surface structures are used even if known to contain many complex surface antigens. The FMNCPs utilize the bacterium's surface as a scaffold to coat the bacterium and effectively make a micro-magnet (figure 2.2) which can be detected by several types of magnetic sensors. Our method of detection is based on Faradays Law of

Induction:

$$V = N \frac{AB}{t}$$

Faraday's Law states that the voltage  $V$  induced in a system is proportional to the number  $N$  of turns in the coil, to the area  $A$  of the coil, and the magnetic flux  $B$  passing through the coil, while it is inversely proportional to the time  $t$  it takes to pass through the coil [3]. This fundamental physical law makes up the basis of our detection method. We can imagine the same concept but on a much smaller scale where we have a micrometer sized magnetized bacterium passing through a coil and inducing a voltage which we measure, the detector itself is made up of a simple coil attached to a very sensitive voltmeter. We now have a very sensitive, fast, and simple detection method. In order to control sensitivity we can change the number of loops or the speed at which the bacterium passes through the coils to increase the voltage. Now we must incorporate this detection method into a platform that will allow the bacterium to come into contact with the

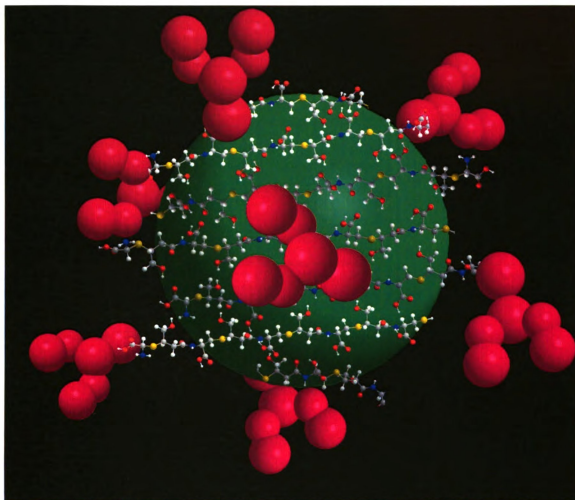
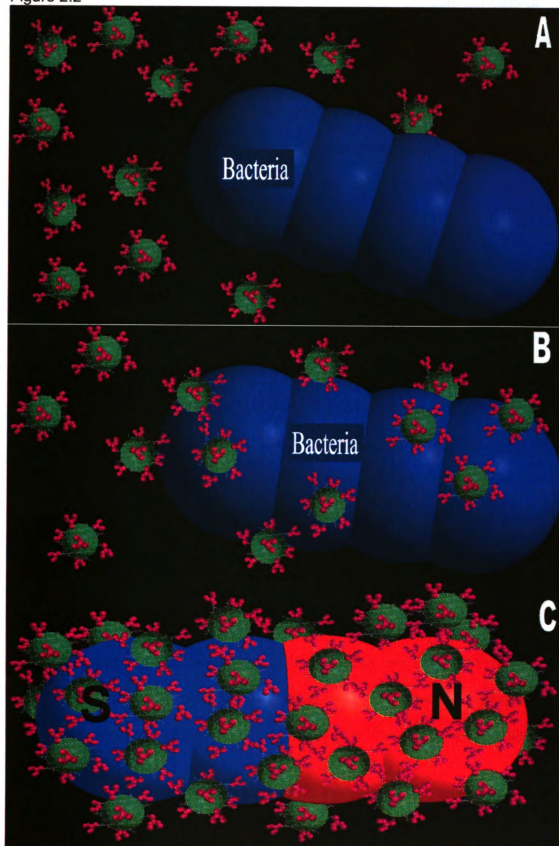


Figure 2.1 FMNCP architecture. The FMNCP is made of a metal nanoparticle core (green), coated with a macromolecular polymer system (multicolored spheres). With antibodies/ surface recognition molecules (pink).

Figure 2.2 A) The bacterium is mixed with the FMNCP suspension. As the bacterium mixes with the FMNCP suspension the FMNCPs coat the cell's surface (B). The FMNCPs interact cooperatively as they bind, transforming the bacterium in to a micromagnet.



Figure 2.2



FMNCPs and then pass through the coil. Our detection platform consists of FMNCPs in a suspension medium that is continually circulating in a loop that passes through the coil (Figure 2.3). When the target bacterium is introduced into the system the FMNCPs bind and encapsulate it as it circulates. As the FMNCP-encapsulated bacterium passes through the coil, it induces a voltage per Faraday's Law, signaling that the bacterium has been detected.

### **Design of FMNCP**

There are many features that must be incorporated in to the design of the FMNCP. These include the ability to identify specific cell surface chemical structures, contain a signal element for detection; forms stable suspensions, and contain functionality which allows for derivatization. The ability to identify specific cell surface chemical structures is done by the use of surface recognition molecules, such as antibodies. The method of detection is magnetic induction so the signal element must be magnetic. The metal nanoparticle core will be made up of the ferromagnetic metal cobalt. The ability to form stable suspensions, and contain functionality which allows for derivatization is a difficult challenge, that leads us to the design of a macromolecular polymer system.

### **Macromolecular polymer system**

The macromolecular polymer system features are, it must (1) show chemical properties similar to biomacromolecules such as proteins, (2) incorporate sites of functionality that can bind transition metals, (3) contain functionality that facilitates attachment of antibodies, and (4) contain

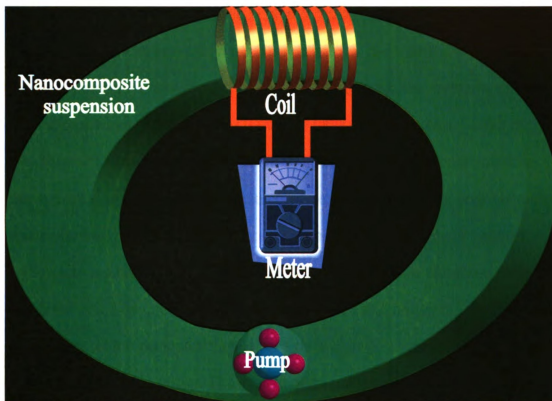


Figure 2.3 The lay out of the general design of the detection platform. The detection platform consists of an induction coil attached to a voltmeter, through which a FMNCP suspension (green) passes through which is circulated in a continuous loop by the pump. Once the target bacterium enters the system in encounters the FMNCPs becoming coated with them, at the same time it is swept through the coil, and induces a voltage signaling detection.

functionality that prevents aggregation. The chemical structure of the macromolecular polymer system can be seen in figure 2.4 it has been designed to incorporate all of the above features. The macromolecular polymer system is a highly functionalized, polypolar chiral polymer. It has many structural and chemical similarities with that of biomolecules, with a polyamide backbone with side chains made up of carboxylic acid and alcohol groups. The large polyamide chain is a peptide mimetic polymer. The polyamide backbone can also aid in secondary structure formations. The polymer backbone also contains thioethers, sulfur atoms have high affinity for transition metals; the numerous thiols in the backbone of the macromolecular polymer system provide multiple points of attachment to the metal nanoparticle core, allowing the polymer scaffold material to envelop the metal nanoparticle core. Once the macromolecular polymer system has bound to the metal nanoparticle, the polymer is stabilized by its polar backbone and side chains in aqueous suspension and behaves like a protein. Stabilization of the nanoparticle suspension is also greatly affected by the charge of the carboxylic acid group. The overall negative charge of the polymer/nanoparticle complex is not only favorable in an aqueous suspension, but it prevents agglomeration of the nanocomplexes through electrostatic repulsion of like charges. The Carboxylic acids share the same charge as many bacteria do which reduces nonspecific bonding. In addition to providing stability, the side chains of the polymer scaffold material also provide an excellent scaffold for further chemical modification.

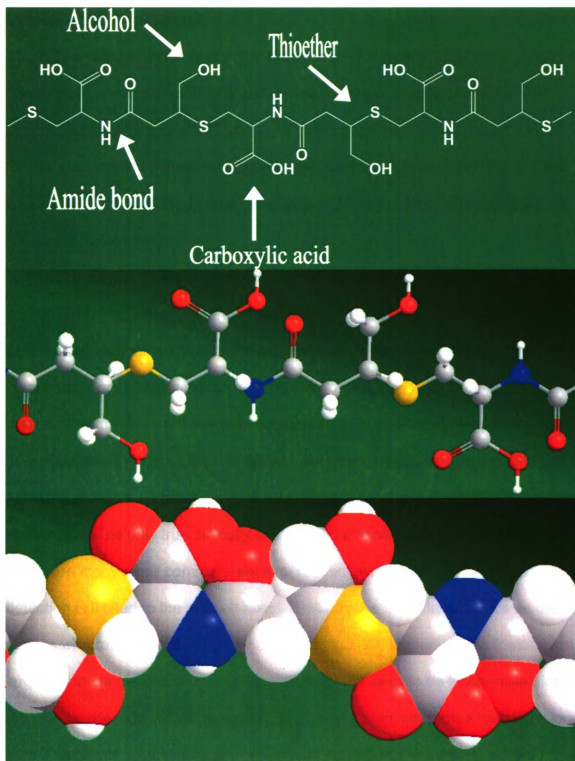


Figure 2.4 Structures of macromolecular polymer system. Top) Chemical structure of the polymer, middle) ball and stick, bottom) space filling. The macromolecular polymer system consists of a chiral backbone made up of a polyamide bonds and thioethers. The polymer scaffold side chains are made up of carboxylic acid and alcohol groups.

## **Detection platform Design**

The overall design of our detection platform (Figure 2.3) is rather simple, it consists of an induction coil attached to a voltmeter, through which a FMNCP suspension passes and is circulated in a continuous loop by a pump. Our vision for this platform is a miniature, simple to use, and portable detector that is small enough to be incorporated into a cell phone or other personal electronics as discussed in Chapter 1.

The simplicity of our detection platform allows for its components to be manufactured individually and then assembled in the platform, which lets us use off-the-shelf technology. With the many technologies available today, many of the components are easily miniaturized and readily available from a variety of manufacturers. There are several companies that specialize in high quality coils, as well as micro pumps, which fit the size and performance requirements of our detection platform. This should speed the production and make fabrication more economical. The only true difficulty lies with the miniaturizing of the voltmeter. There are many small commercially available voltmeters, but their range of detection is limited to the millivolt range. This creates a challenge for us as our system will create a current in the nanovolt range. While many of the features on larger nanovolt meter are unnecessary and will not need to be incorporated into the final device, it is still difficult to miniaturize and maintain such a low detection limit. The use of custom designed integrated circuits (IC) will greatly aid the miniaturization of the volt meter. For increased functionality, other electronic components will be incorporated allowing for data storage and analysis. The

device will be programmable with a variety of functions. Another solution is to use a different detector such as an atomic magnetometer.

The shrinking of the components of the device to make a smaller instrument is a key step in making a versatile and functional detector. A device that is easily held in your hand, clipped to your belt, or slipped into a pocket, much like a cell phone is the ideal size. The increasing computing and memory capacity of smaller and smaller electronics and modern microfabrication, decrease cost, while increasing the capabilities of the detection platform. These advancements allow for on board data storage and analysis, wireless capabilities with down loads, updates and alerts.

### **Theoretical Calculations and Expected values**

In this section, theoretical calculations are used to demonstrate that the mode of operation of the device is physically possible and within the realm of today's technological capabilities. Please note many of the calculations are done as theoretical maximum and some assumptions are made in order to simplify the calculations. More complicated calculations and simulations could be used but the number of variables and the broad range of magnetic properties brought about by small changes in nanoparticles make it an act of futility, unless all of the variables are known. For this reason it is better in some cases to do experimentation first and then try and determine which properties are playing the crucial parts.

In order to determine the voltages induced by a bacterium coated with ferromagnetic nanoparticles as it passes through a coil, we can first start by

looking at what voltage should be induced by a single ferromagnetic nanoparticle (FMNP). Faraday's law (equation 1) [4] can be used to calculate the voltage induced, where  $N$  is the number of turns in the loop,  $\Phi$  is the magnetic flux moving through the coil, and  $dt$  is the time it takes to pass through the loop:

$$V = -N(d\Phi/dt) \quad 1.$$

In our calculation we will assume that the FMNP passes through the loop at its center with its magnetic field perpendicular to the plane of the loop. The particle will be treated as a point magnetic dipole (Figure 2.5). In order to calculate the voltage using equation 4 we must determine  $d\Phi$ ; all of the other variables are known. The magnetic flux is given by equation 2:

$$\Phi = \int \mathbf{B} \cdot d\mathbf{A} \quad 2.$$

where  $A$  is the area of the loop and  $\mathbf{B}$  is the magnetic flux density given by equation 3 [5]:

$$\mathbf{B} = \mu/4\pi(-\mathbf{m}/r^3 + (3\mathbf{m} \cdot \mathbf{r})\mathbf{r}/r^5) \quad 3.$$

Where  $\mu$  is the permeability of free space,  $m$  is the magnetic moment and  $r$  is the distance from the point magnetic dipole to the loop. Integrating equation 3 over the area of the loop at radius  $R$  in the  $z$  direction we get equation 4. This gives us the magnetic flux through the loop in the  $z$  direction at distance  $z$  away (Figure 2.6).

$$\Phi(z) = \mu m/2 [ (R^2+Z^2)^{-1/2} - Z^2(R^2+Z^2)^{-3/2} ] \quad 4.$$

from which we derive

$$d\Phi/dz = \mu m/2 [ (4/3)Z^3(R^2+Z^2)^{-5/2} - 3Z(R^2+Z^2)^{-3/2} ] \quad 5.$$



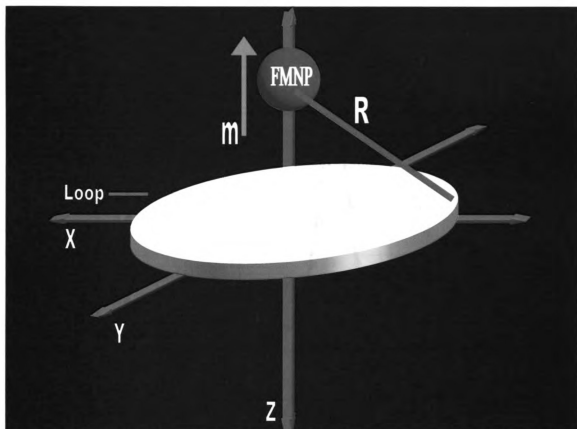


Figure 2.5 The drawing above shows the FMNP (red) moving down in the z axes through a single loop (green) with its magnetic moment ( $m$ ) perpendicular to the loop, which is in the x-y plane.

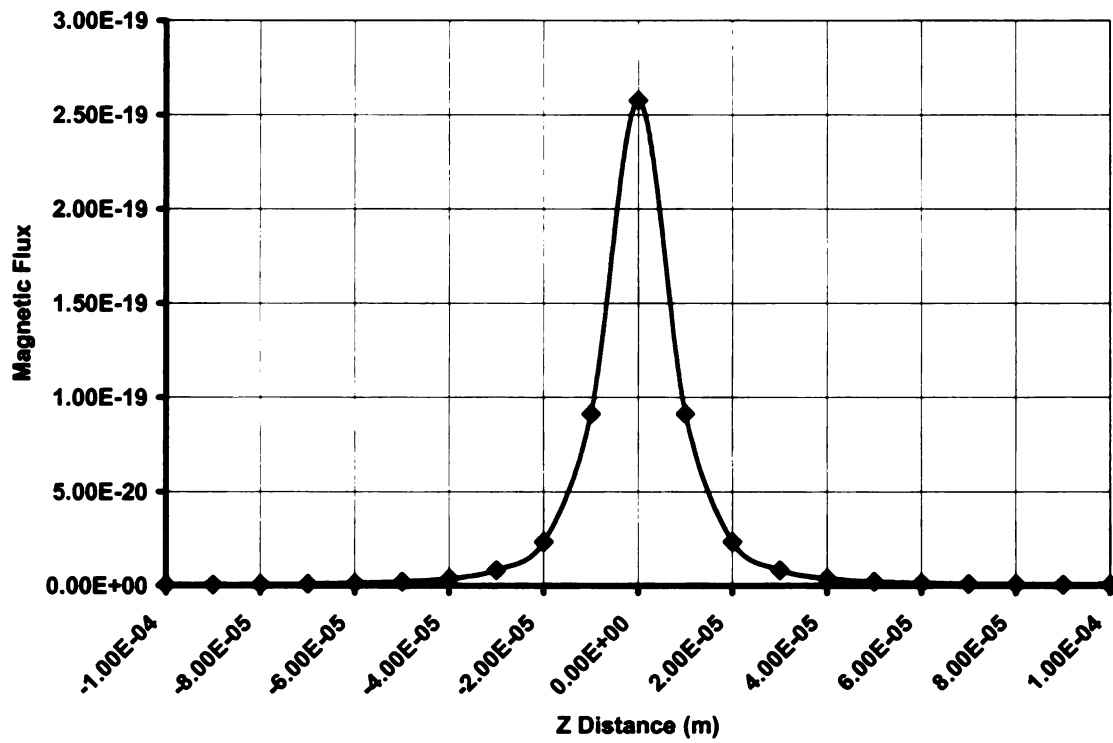


Figure 2.6 Graph of equation 4 showing the magnetic flux of a single FMNC as a function of distance from the loop.

The voltage due to the changing flux

$$V = -N(d\Phi/dt) = -N(d\Phi/dz) \cdot (dz/dt) \quad 6.$$

may be calculated as

$$V = -N \cdot \mu_0 m / 2 \left[ (4/3)(v \cdot t)^3 (R^2 + (v \cdot t)^2)^{-5/2} - 3(v \cdot t)(R^2 + (v \cdot t)^2)^{1/2} \right] \cdot v \quad 7.$$

Equation 5 gives us the rate of change in the magnetic flux as a function of Z (Figure 2.7). Now if we substitute equation 5 into equation 6 and let Z from equation 4 equal  $v \cdot t$  where  $v$  is the velocity of the FMNP and  $t$  is time, we get equation 7 which gives us the voltage as a function of time as it passes through the loop. The graph of equation 10 (Figure 2.8) of the voltage vs. time has a peak voltage of  $1.36 \times 10^{-12} \text{V}$  for a single FMNP passing through the coil at 53 m/sec. Assuming that all of the FMNP are bound to the surface of the bacterium and are aligned in parallel; then the theoretical maximum voltage induced by a single bacterium coated with 15,000 FMNP would be  $2.04 \times 10^{-8} \text{V}$ . This value is based on estimated and predicted values of a proposed detection platform in order to get theoretical maximum values and not actual experimental data (see appendix III for calculations). The predicted voltages are well within the lower range ( $1 \times 10^{-9} \text{V}$ ) of many commercially available voltmeters. We must also remember that if we want to increase our signal we can always add more turns to the coil, and speed up the flow of the suspension. While orientation of FMNCPs may be an issue, one can easily solve this by adding an external field, and in fact it would be beneficial to impose an external field regardless of the size of the particles.

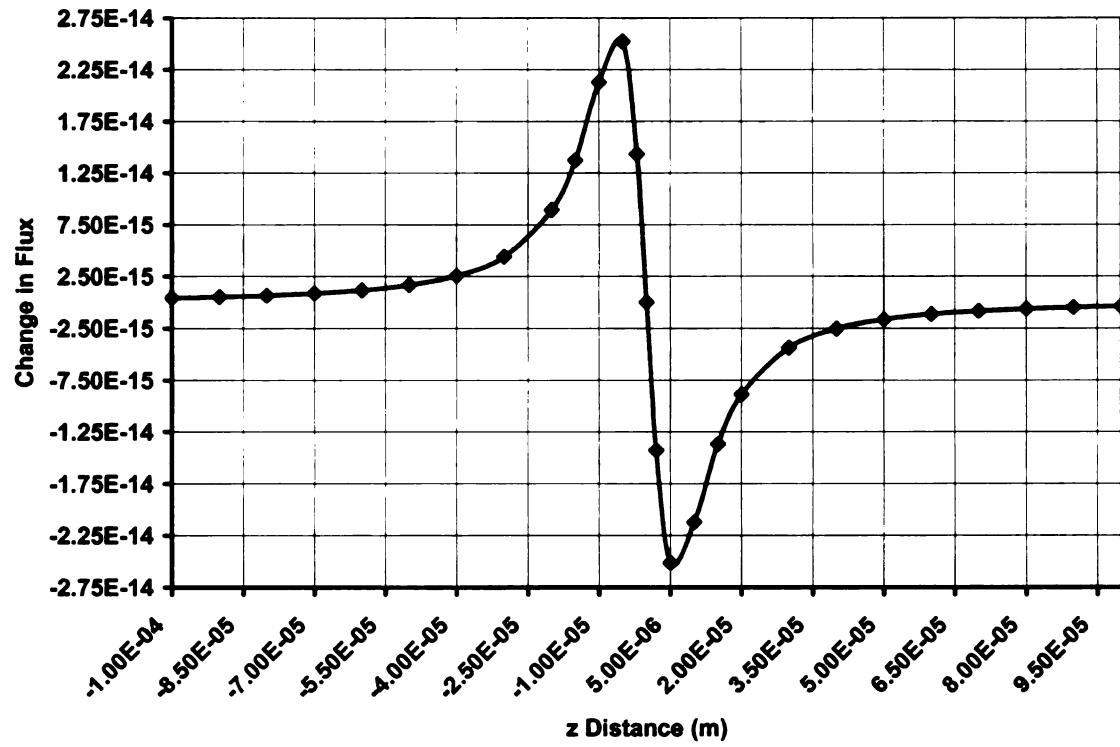


Figure 2.7 Graph of equation 5 showing the change in the magnetic flux of a single FMNC as a function of distance from the loop.

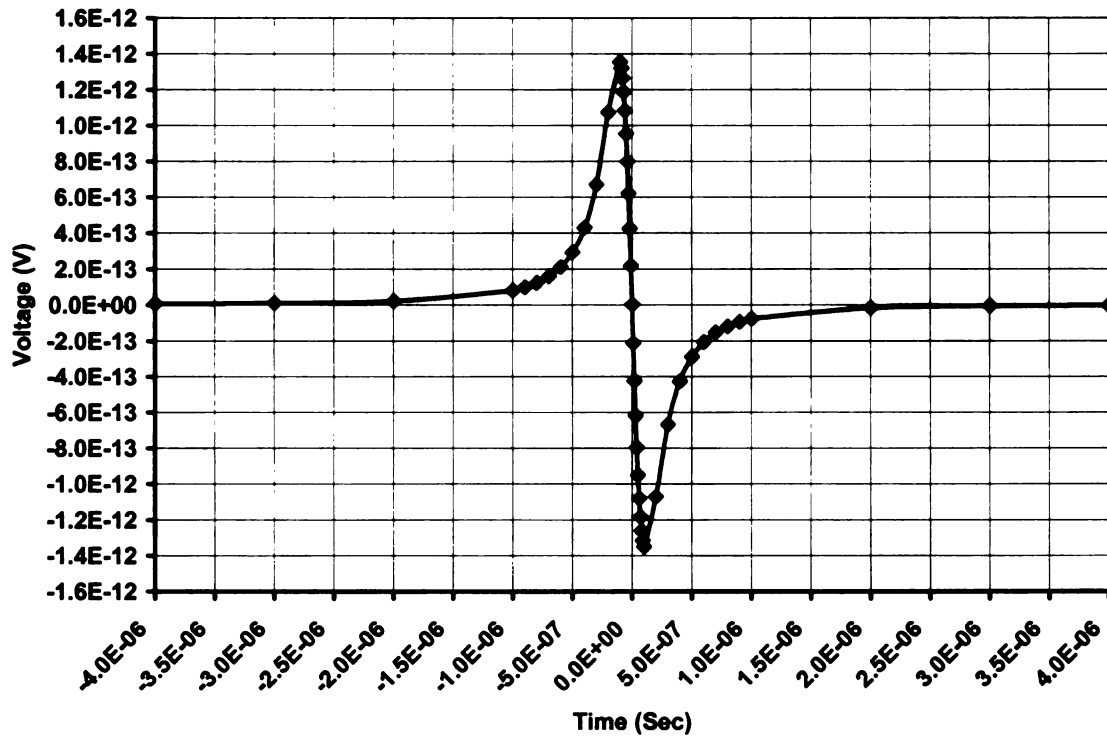


Figure 2.8 Graph of equation 7 showing the voltage induced by a single FNP passing through a single loop.

## Noise

As with most electronic devices, there are both internal and external sources of noise. Many external sources of noise are mainly electromagnetic waves/fields caused by modern electronics; luckily, this noise is easy to remove by proper shielding of the device as well as use of low/high bandpass filters. There are also biological sources of noise such as magnetotactic bacteria in the environment, however chances of encountering them in everyday sampling are very small. When considering noise there are three major sources: chemical, instrumental, and environmental noise.

Environmental noise in the form of electromagnetic radiation is everywhere, saturating our world. Cell phone towers, microwave towers, satellites, radios, high power lines, and much more, all produce electromagnetic radiation (there are also natural sources such as the earth's magnetic field and solar flares). The background of electromagnetic radiation in our environment can make low level voltage measurements difficult without proper grounding and shielding. It is no surprise that nearly all electronic devices require some form of shielding because the 110 V that is used in every home in the US can induce millivolt voltages. Shielding consists of surrounding the instrument and/or its components (circuits, wires, other) with a conducting material that is grounded to the earth, the shielding structure is known as a Faraday cage. Proper grounding and shielding of instruments can eliminate much of the environmental noise caused by electromagnetic radiation. In our detection platform using a Faraday

cage to house the detector-shielded wires is a simple solution to environmental noise from electric fields but not magnetic.

Instrumental noise in low level measurements used by our detection platform can mainly be attributed to thermal (Johnson) noise and thermoelectric effects (thermocouple). Thermal noise arises from thermal agitation of the charge carrying elements of the instrument. The thermal agitation causes charge inhomogeneities that in their turn cause voltage fluctuations. The magnitude of the thermal noise for the platform can be determined using equation 8 [6].

$$V_{RMS} = \sqrt{4kTRF} \quad 8.$$

Where  $k$  is the Boltzmann constant,  $T$  is the temperature (K),  $R$  is the source resistance (ohms) and  $F$  the noise bandwidth (Hz). The second major contributor to the instrumental noise is the thermoelectric effects which are small potentials generated by differences in temperature at junctions of dissimilar metals. These can arise from junctions of the same metal as well. The thermal EMF that can be generated is given by equation 9.

$$E = Q_{ab}(T_1 - T_2) \quad 9.$$

Where  $Q_{ab}$  ( $0.2 \mu\text{V}/^\circ\text{C}$  for Cu-Cu junction) is the thermoelectric coefficient with respect to the two metals in the junction and  $T_1$  and  $T_2$  is the temperature of the respective metals. Using equation 9 we can see that a difference in just one degree in a copper-copper junction can yield an EMF of  $0.2 \mu\text{V}$ . While thermoelectric effects can produce large EMF, they can be minimized by using clean, same metal junctions that are maintained at the same temperature. In both cases of instrumental noise for our detection platform, proper calibrations of the

device for the temperature it is to be operating at allows for noise to be minimized and accounted for.

For this paper, chemical noise will refer to the noise induced by the free nanocomposites in suspension. The noise from the free FMNPs assuming that they are independent of each other is given by Poisson noise. We assume that there are only two orientations that the FMNPs can take with their magnetic moment perpendicular to the loop: either up or down. The number of particles in the coil at any one time will be around  $3.78 \times 10^5$  FMNPs when using a 1nM solution. The Poisson noise produced from these particles can be expected to be about  $\pm 5.92 \times 10^{-10}$  V. This is approximately 2.9% of the voltage that is expected to be induced by the coated pathogen. We can also expect the noise to be less than this, due to the tumbling time of the free FMNPs. A 30 nm FNP has a tumbling time of 21.6  $\mu$ sec and the time for a particle to pass through the loop is 37.7  $\mu$ sec. This means that, the time that it takes the FMNPs to pass through the loop, they have tumbled through every possible orientation at least once. As stated earlier the tumbling time of a bacterium is 0.15 sec, which is much slower than that of the free FMNPs, and then the concern is its orientation to the loop. This problem may be solved by using a series of loops and not just a single loop for detection.



#### Reference:

1. C. N. Keim, M. Farina, U. Lins,. Magnetoglbis; Magnetic Aggregates in Anaerobic Environments. Microbe, Vol:2 pg: 437-445.
2. D. Schuler,. Eds. Magnetoreception and magnetosomes in bacteria; Springer-Verlag Berlin Heidelberg 2007 pg 8.
3. D. Jiles, Introduction to magnetism and magnetic materials, Chapman and Hall, New York. 1991
4. D. Halliday, R. Resnick, J. Walker, Fundamentals of Physics Fifth Edition. USA (1997)
5. J. Marion, W. Hornyak, Physics for science and engineering part 2. New York (1982)
6. D. A. Skoog, F. J. Holler, T. A. Nieman, Principles of instrumental analysis; Saunder College Publishing: United States, 1998.

## **Chapter 3**

### **Macromolecular polymer system**

#### **Introduction**

The macromolecular polymer system is a new polymer that has never been made before. It has been designed to accomplish many features. The ferromagnetic nanocomposite particles consist of a ferromagnetic nanoparticle metal core encapsulated by the macromolecular polymer system, through which the SRMs are covalently linked. In designing the macromolecular polymer system for synthesizing the nanocomposite particles, we are in search of a material with many robust attributes. Nanoparticles that are left uncapped tend to agglomerate and precipitate out of suspension quickly whereas capped particles remain in suspension much longer [1, 2, 3]. There are a multitude of capping agents available with a broad range of chemical makeups and sizes, from small polar molecules to large hydrophobic molecules. In order for a compound to be a capping agent it must have the proper chemical features that will allow it to do two things. One chemical feature is that it must have an affinity for the metal nanoparticle and remain associated with it (bonded to it). The second chemical feature is that it must be soluble in its surrounding solvent; this favorable interaction of capping agent with its surrounding solvent slows the precipitation of nanoparticles out of suspension. There is also a third chemical feature, that while not required in a capping agent, is an advantageous feature especially when dealing with magnetic nanoparticles. The feature is one that prevents agglomeration of nanoparticles such as electrostatic repulsion, which slows the

precipitation nanoparticles out of suspension. All of these features help to maintain and increase the longevity of the suspension.

The polymer scaffold material is an excellent capping agent because, not only does it embody all of the above features, it also has other features that make it suitable for our purpose. It has structural and chemical similarities with that of biomolecules, with a polyamide backbone with side chains made up of carboxylic acid and alcohol groups. The sulfur atoms in the polymer backbone have a high affinity for transition metals and provide binding interaction to the metal core allowing the polymer to encapsulate the nanoparticle. And the Carboxylic acids have the same charge of bacteria which reduces nonspecific bonding, prevents aggregation, and are a point for chemical modification. The macromolecular polymer system is a unique and novel polymer not only by way of its structure but its synthesis as well [4, 5]. Syntheses of high molecular weight polyamides is not an easy task, and not viable in step wise methods. The macromolecular polymer system made using 2(H)-furanone and L-cysteine methyl ester, both of which are organic compounds that are derived from natural sources. The synthesis of the polymer uses mild conditions and no organic solvents, making it an environmentally friendly as well as inexpensive process.

The reaction takes place in a stepwise manor (figure 3.1) first, with the sulfur of the L-cysteine methyl ester attacking the double bound on the 2(H)-furanone in a Michael addition, to form a lactone monomer. The lactone monomer then polymerizes in a head to tail manner with the amine group attacking at the carbonyl, and opening the lactone ring. After polymerization the

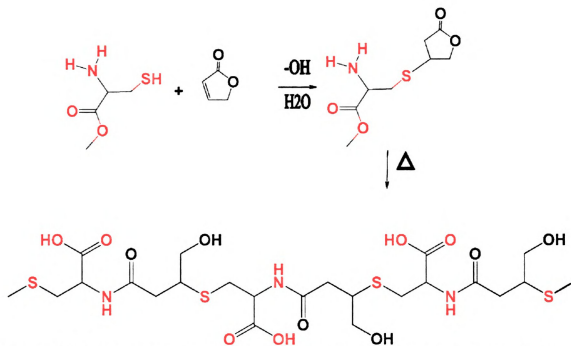


Figure 3.1 Reaction mechanism of macromolecular polymer system synthesis. First a Michael addition of the L-cysteine methyl ester (red) to the 2(H)-furanone to form a lactone monomer. Next the lactone monomer polymerizes in a head to tail manner and then the methyl ester is removed.

macromolecular polymer system is deesterified, and size specific membrane fractionation using molecular weight cut offs (MWCO) of 3,500 and 13,000 Da is done.

## **Experimental**

Synthesis of macromolecular polymer system A and B. Sodium bicarbonate (0.84 g, 0.01 mol) and L-Cysteine-methylester (1.71 g, 0.01 mol) were dissolved in water (20 mL). Once dissolved Furanone (0.84 g, 0.01 mol) was added quantitatively using water (5 mL). The reaction mixture was left at 25 °C for 1 hour with stirring. At the end of one hour the reaction mixture was rotovapped to remove the water, and then placed in an oil bath for 3 hours at 90 °C. Then the reaction mixture was heated at 90 °C for 18 hours for further polymerization. The polymer mixture was then dissolved in a water solution and placed in 3,500 MWCO dialysis membranes and dialyzed for 24 hours, changing the water every 2 hours for the first 8 hours, then every 4 hours. The solvent was then removed to yield the macromolecular polymer system A. The same procedures were followed for macromolecular polymer system B except that after the polymerization the polymer mixture was dissolved in a water solution of sodium hydroxide (0.2 M) for one hour with stirring at 25 °C to remove the methyl ester. And placed in 3,500 MWCO dialysis membranes and dialyzed for 24 hours, changing the water every 2 hours for the first 8 hours then every 4 hours. The solvent was removed to yield the macromolecular polymer system B. All NMR spectra were taken using a Varian Inova 300 NMR.

## Results and discussion

NMR spectroscopy of the macromolecular polymer system was used to determine the reaction mechanism (figures 3.2, 3.3, 3.4) and characterize the macromolecular polymer system structure (figure 3.5). The NMR at time 0 of the reaction mixture show the chemical shifts of both starting materials. After 15 min the chemical shifts of the furanone have decreased by more than 2/3 and new chemical shifts for the lactone monomer have appeared. After 30 min the furanone shifts are nearly gone. Looking at the NMR for the final polymer the chemical shifts for the lactone are gone and the new shifts of the polymer backbone can be seen, this and the broadening of these chemical shift confirms polymerization of the macromolecular system. IR spectroscopy (figure 3.6) of the macromolecular polymer system as well as electrospray mass spectrometry (figure 3.7) was performed. The IR spectra shows the amide I and II bands, as well as the stretches for the alcohol and carboxylic acid side chain groups, which further confirms amide bond formation and polymerization of the polymer. In the mass spectrum we see a typical distribution of fragments for a polymer, and that the major fragments are multiples of 205 Da which is the mass of the monomer unit -1, which confirms the repeat structure of the macromolecular system. The use of size specific membrane fractionation also insures polymerization and high molecular weight material greater than 3,500 and 13,000 Da. The end product is a high molecular weight macromolecular polymer system that is a peptide mimetic with a number of chemical functionality, is inexpensive, and easy to synthesize.

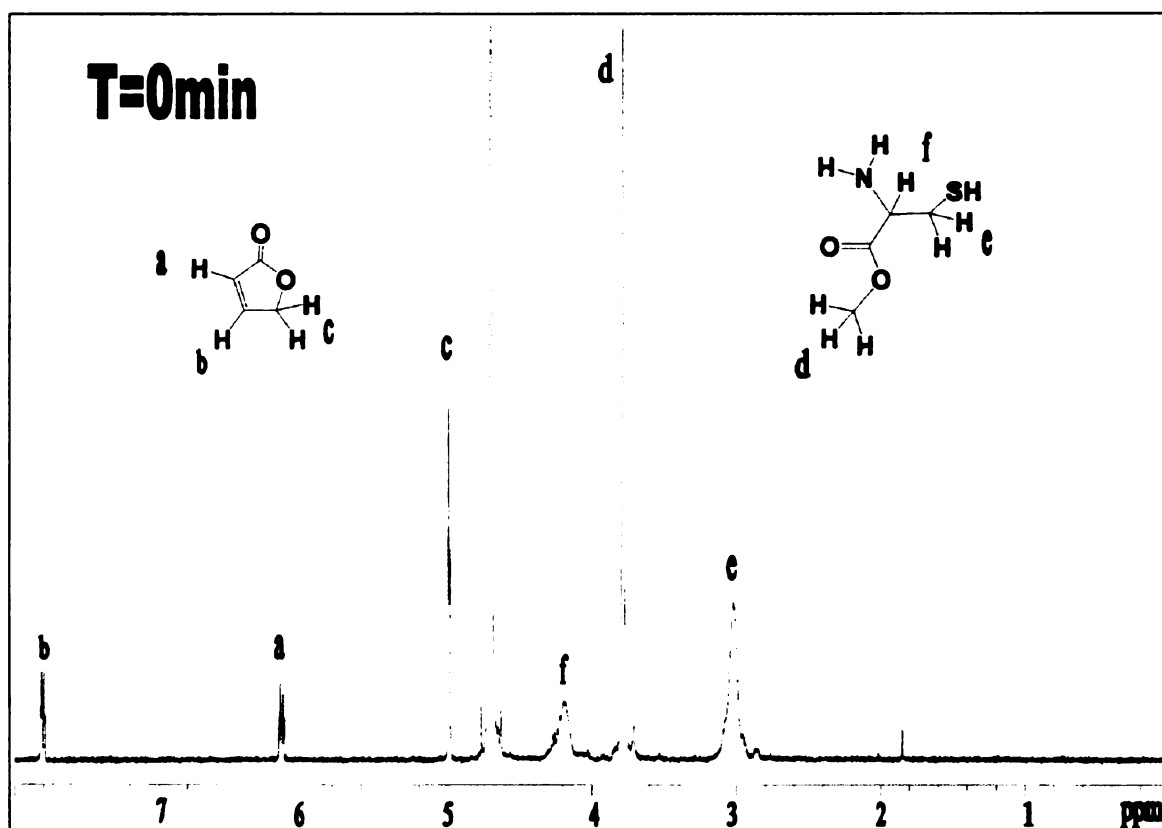


Figure 3.2  $^1\text{H}$  NMR of and L-Cysteine-methylester and Furanone reaction at time 0.

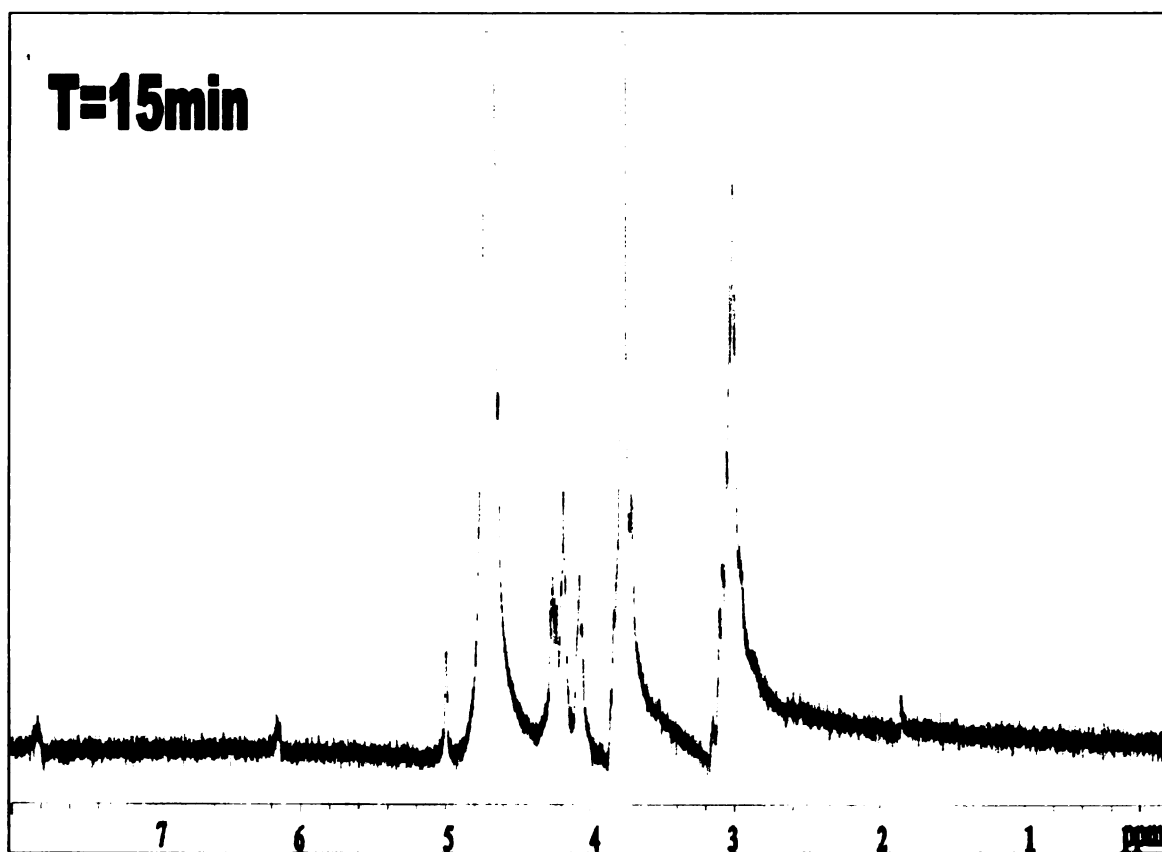


Figure 3.3  $^1\text{H}$  NMR of and L-Cysteine-methylester and Furanone reaction after 15 minutes.



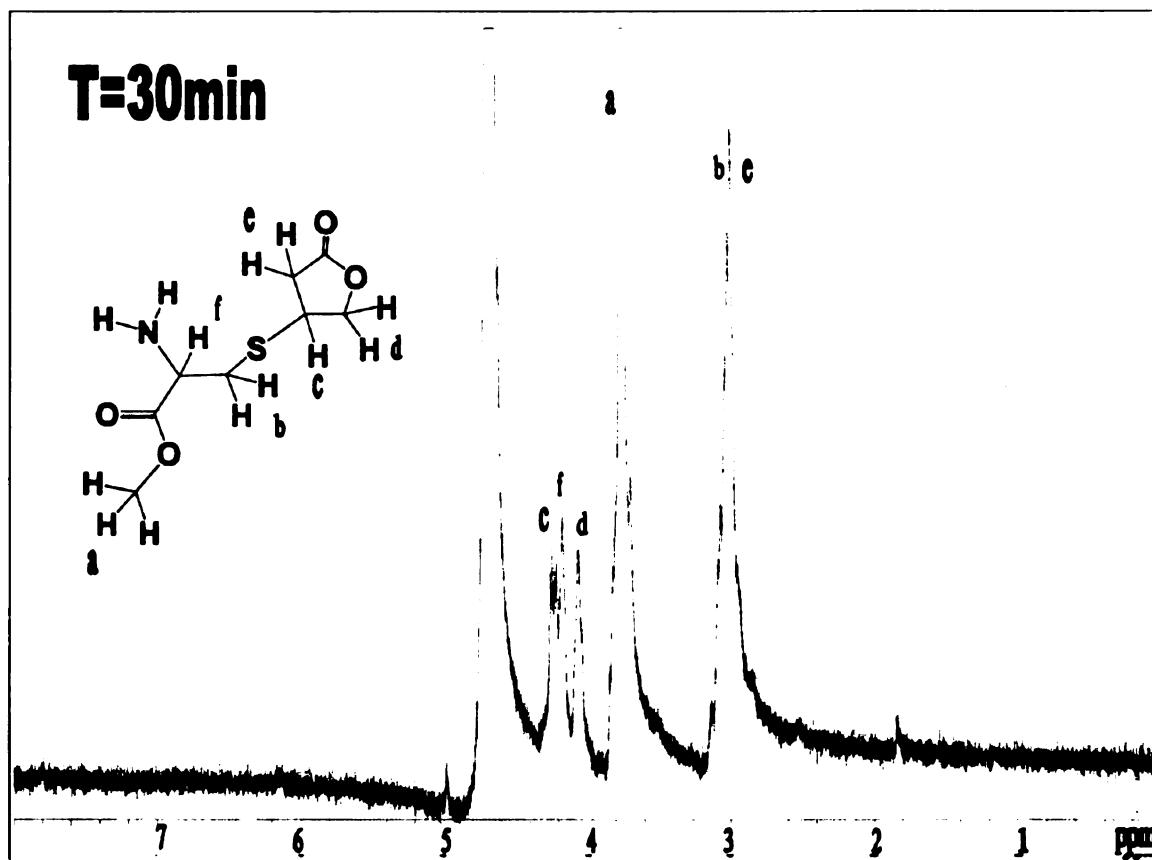


Figure 3.4  $^1\text{H}$  NMR of L-Cysteine-methylester and Furanone reaction after 30 minutes

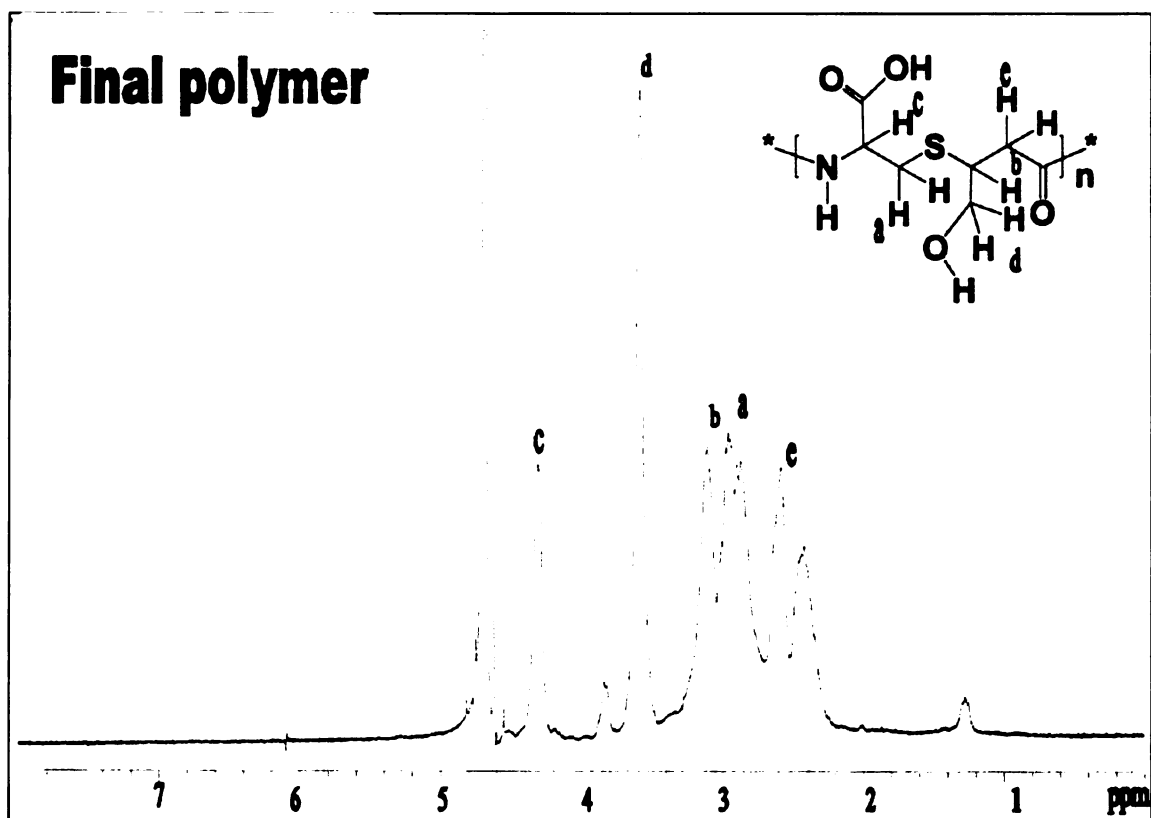


Figure 3.5  $^1\text{H}$  NMR of final macromolecular polymer system after polymerization and deesterification.

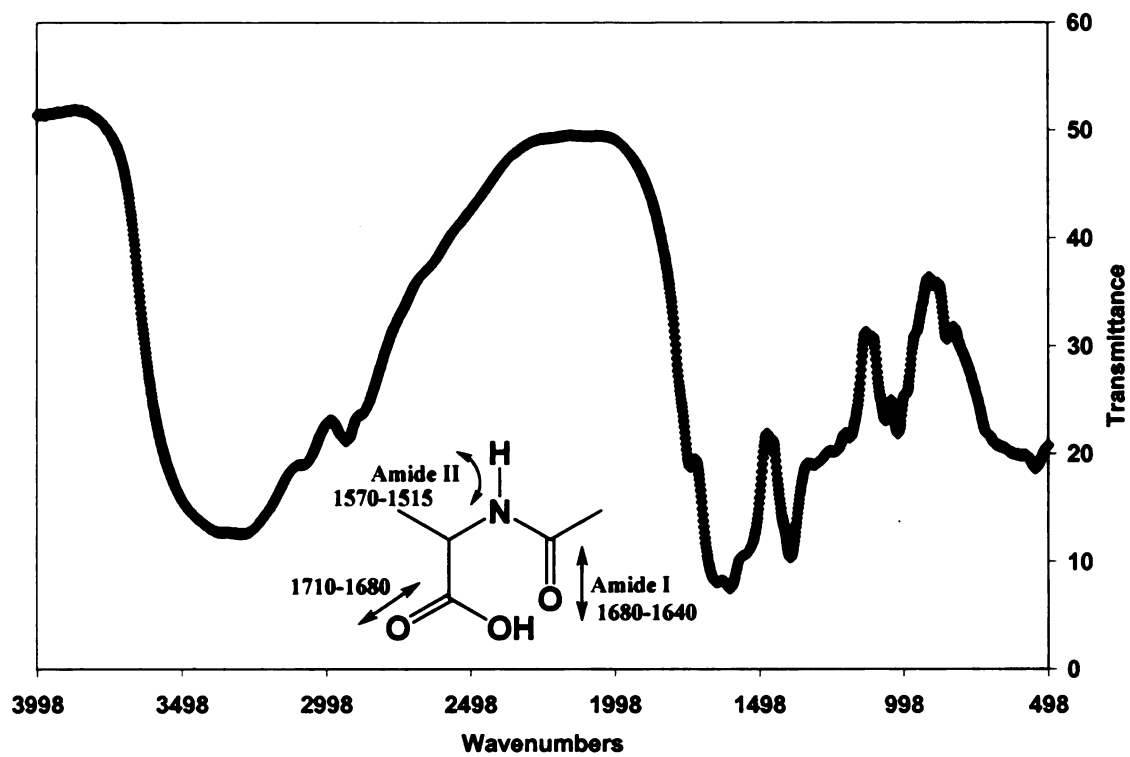


Figure 3.6 IR spectroscopy of macromolecular polymer system.

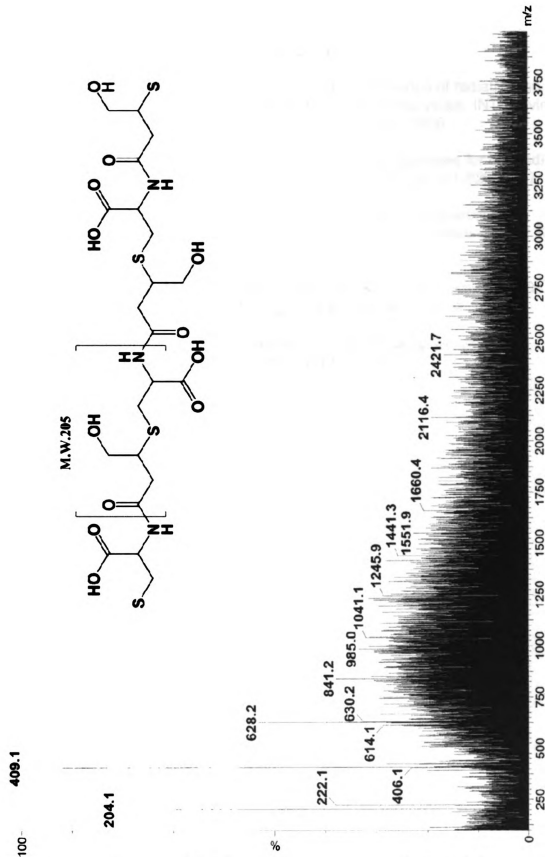


Figure 3.7 Electrospray mass spectrum of macromolecular polymer system.

## REFERENCES

1. S. Link , M.A. El-Sayed, Shape and Size dependence of radiative, non-radiative and photothermal properties of gold nanocrystals. INT. Reviews in Physical Chemistry, Vol:19 Issue:3 pg:409-453, 2000.
2. C.J. Xu, S.H. Sun, Monodisperse magnetic nanoparticles for biomedical applications. Polymer International, Vol:56 Issue:7 pg:821-826, 2007.
3. P. Majewski, B. Thierry, Functionalized magnetite nanoparticles-synthesis, properties, and bio-applications. Critical Reviews in Solid State and Material Sciences, Vol:32 pg:203-215, 2007.
4. Cao, P. Development and Synthesis of Novel Poly (B-Amino acid) Drug Delivery Systems; Thesis Michigan State University, 2004.
5. U.S. Patent # 6153724, Preparation of cross-linked 2-dimensional polymers with sidedness from  $\alpha,\beta$ -lactones. 2000.

## **Chapter 4**

### **Nanocomposite Material**

#### **Introduction**

The optical and magnetic characteristics of nanoparticles differ greatly as compared to their bulk material. These differences are dependent on the size and shape of the nanoparticles, this dependence allows one to control the optical and magnetic characteristics of nanoparticles by changing the size and/or shape of the nanoparticles. The high surface to volume ratio of nanoparticles results in a larger percentage of the total atoms displayed on the surface. As a particle gets smaller, the dispersion, or the fraction of atoms on the surface, increases, and scales with the surface area divided by the volume [1]. The cohesive energy, which is the average bond energy of a solid, can be seen to decrease as the particle gets smaller. This is due to the fact that the atoms at the surface have lower coordination and fewer bonds than the atoms in the interior which lowers the average bond energy of the particle. The lowering of the cohesive energy is one factor that gives rise to the unique properties of nanoparticles such as lower melting points. The optical properties of nanoparticles are due to two separate phenomena: quantum confinement and surface plasmon. Quantum confinement effects cause increasing separation of energy levels as a particle decreases in size similar to a particle in a box [1, 2]. Quantum confinement effects on metal nanoparticles are typically observed in particles smaller than 2 nm, and are distinct from surface effects. The surface plasmon of a nanoparticle, however, is affected by the surface, and is a result of the interactions of the conducting

electrons at the particle's surface with the electric field of a light wave. This leads to a strong absorption of light, with high molar extinction coefficients in the range of  $1 \times 10^9 \text{ M}^{-1} \text{ cm}^{-1}$ , which is several times higher than that of strong absorbing organic dyes [2]. The core of the FMNCP must be made up of a ferromagnetic material such as iron, cobalt, or nickel. The core of our FMNCP is made up of a cobalt nanoparticle. Cobalt has a magnetic moment of  $161 \text{ Am}^2/\text{kg}$  second only to iron [3]. The magnetic properties of nanoparticles are greatly influenced by their shape and size as well, and are discussed in the next section.

The optical and magnetic properties of nanoparticles make them ideal components to be incorporated into our nanocomposite material. Nanoparticles have distinctive advantages over traditional materials, one being that they don't undergo irreversible reactions when a measurement is made, allowing for measurements to be repeated and the recycling of materials. All of the different components of the FMNCP serve specific functions and are integrated to form a simple composite of complex function.

### **Ferromagnetic Nanoparticles**

In bulk ferromagnetic materials domain wall formation is driven by the balance between the magnetostatic energy, which increases proportionally to the volume of the material, and the domain-wall energy, which increases proportionally to the interfacial area between domains [4]. As a nanoparticle's size is decreased the surface-to-volume ratio changes and domain wall formation becomes unfavorable. The area over which the energy would be most highly distributed is larger than the particle itself and the result is a single domain

ferromagnetic nanoparticle. These single domain ferromagnetic nanoparticles can be thought of as a giant magnetic dipoles with unique magnetic properties dependent on size and shape. Ferromagnetic nanoparticles have much higher spin densities than that of their bulk material. Also asymmetries at the surface of the nanoparticles cause enhanced anisotropy, increasing the anisotropy energy. The size at which this happens varies with the material and shape of the nanoparticle; for spherical cobalt nanoparticles the critical diameter is 80 nm [5]. As the ferromagnetic particles get smaller they reach a second critical diameter. This second critical diameter is one at which their magnetic properties change drastically. This is due to the lowering of the anisotropic energy as the particle gets smaller. At the second critical diameter the thermal energy (at room temperature) becomes equivalent to that of the anisotropic energy allowing the magnetization of the particle to rapidly fluctuate from one direction to another. This results in ferromagnetic nanoparticles that have a net magnetic moment of zero and are paramagnetic. These nanoparticles are said to be superparamagnetic; spherical cobalt nanoparticles become superparamagnetic below 10 nm. The exchange energy still holds strong and maintains the cooperative alignment of the point magnetic dipole unlike paramagnetic materials where the thermal energy is proportional to or greater than the exchange energy. In these particles the reversal of magnetization takes place by coherent rotation, that is all of the dipoles remain parallel as the direction changes. Superparamagnetic materials fall inbetween paramagnetic and ferromagnetic behavior, having a much higher magnetization (M) and saturated magnetization



( $M_s$ ) than paramagnetic materials and having coercivity and remanence of zero [6].

The anisotropy energy of a single domain nanoparticle can be determined using the following equation [7]:  $E_A(\theta) = K_{eff} * V \sin^2 \theta$ .

Where  $K_{eff}$  is the anisotropy constant,  $V$  is the volume of the particle and  $\theta$  is the angle between the magnetization and the easy axis; where  $K_{eff} V$  is the energy barrier that must be overcome to reverse the magnetization. For cobalt the calculation is much simpler due to its hexagonal (uniaxial) anisotropy. That is cobalt only has one easy axis due to its hexagonal crystalline structure. In the case of iron the calculation is not as simple; the cubic anisotropy must be calculated from the magnetization of the three crystal easy axis. The easy and hard directions of magnetization along the crystal axis are the result of spin orbit coupling [8]. The Neel-Brown expression can be used to give the relaxation time of the magnetic moment of a particle, using the anisotropy energy and the thermal energy [7]:

$$\tau = \tau_0 e(K_{eff} V / k_b T) \quad \text{note } \tau_0 = 10^{-9} \text{ s}$$

The Neel-Brown expression is used to determine if a ferromagnetic nanoparticle is in a paramagnetic state or a blocked state. That is, if the relaxation time is shorter than the experimental, then it is superparamagnetic. The transition from ferromagnetic to superparamagnetic for a given particle size is called the blocking temperature [9]. Superparamagnetic nanoparticles are very useful because they do not agglomerate like ferromagnetic particles do until placed in a magnetic field of suitable strength.

## Interaction of Ferromagnetic Nanoparticles

The function of our detection platform will be dependant upon the interaction of ferromagnetic/superparamagnetic nanocomposite particles attached to the bacterial cell surface. In order to better understand the phenomena one might expect to see, we shall first take a look at some bacteria with naturally occurring ferromagnetic nanoparticles.

Magnetotactic bacteria are aquatic bacteria that orient and swim along magnetic field lines, a behavior known as magnetotaxis [10]. Magnetotactic bacteria make up a diverse collection of prokaryotes but all contain magnetosomes.

Magnetosomes are intracellular structures made up of mineral crystals of magnetite ( $\text{Fe}_3\text{O}_4$ ) or greigite ( $\text{Fe}_3\text{S}_4$ ) surrounded by a lipid bilayer [11].

Magnetosome crystals range in size from 35 to 120 nm long and are single domain nanomagnets. The magnetosomes are arranged in a chain longitudinally across the cell, with the number of magnetosomes varying, but averaging 20 [10]. It has been shown by Frankel et al. [10] that the interaction of the magnetosomes with the Earth's magnetic field supplies enough energy to overcome the thermal agitation and cause an average orientation parallel with the Earth's magnetic field. The alignment of the magnetotactic bacteria allows them to swim along the earth's magnetic field lines, a phenomenon called magnetotaxis. The magnetotaxis allows the bacteria to swim down in the water column to find the oxic-anoxic interface and anoxic regions that they inhabit.

In order to determine the orientation of a magnetic dipole in an external field like those in magnetotactic bacterium or nanoparticles one can use the

Langevin function:

$$\cos \theta = L(\alpha)$$

Where  $\theta$  is equivalent to the average angle between the magnetic moment and the magnetic field and  $L(\alpha)$  is the Langevin function:

$$L(\alpha) = \coth \alpha - \alpha^{-1} \quad \alpha = mH/kT$$

Where  $L(\alpha)$  is a function of the ratio of the thermal energy and the Zeeman energy (Figure 4.1); the Zeeman energy is the energy of the magnetic dipole moment interacting with an external magnetic field and is given by the equation:

$$E = mH \cos \theta$$

The Zeeman energy is a function of the magnetic moment  $m$ , the external field  $H$  and the angle  $\theta$  between them. The magnetic moment depends on the particle's volume and the material it is made of: the number of atoms and the size of their atomic moments [12]. Figure 4.2 shows the energy of a cobalt nanoparticle interacting with the Earth's magnetic field as a function of the particles diameter. The energy increases exponentially as the particle gets larger, as one would expect because the number of moments added increases proportionately to the volume. We can also see that it takes a rather large particle ( $\approx 50$  nm) to equal that of the thermal energy of  $4.14 \times 10^{-21}$  J. While one single particle may not have enough energy to align itself with the earth's field, one must remember that the energy is dependent on the number of atomic moments, which can be increased simply by

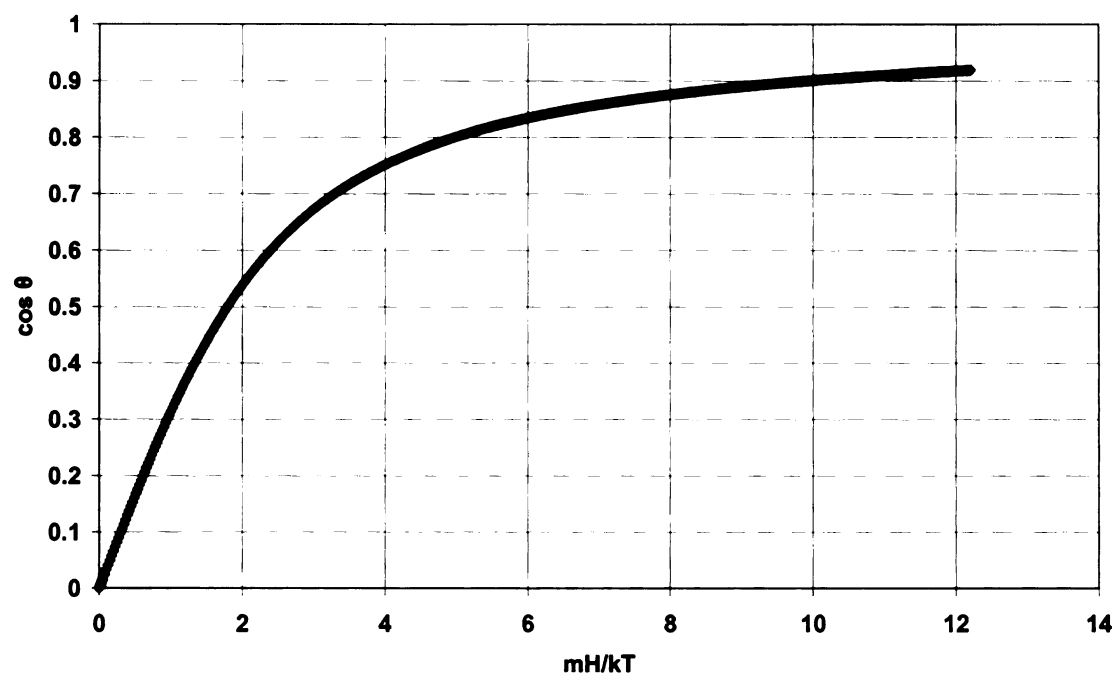


Figure 4.1 The Langevin equation plotted as a function of the ratio  $mH/kT$ .

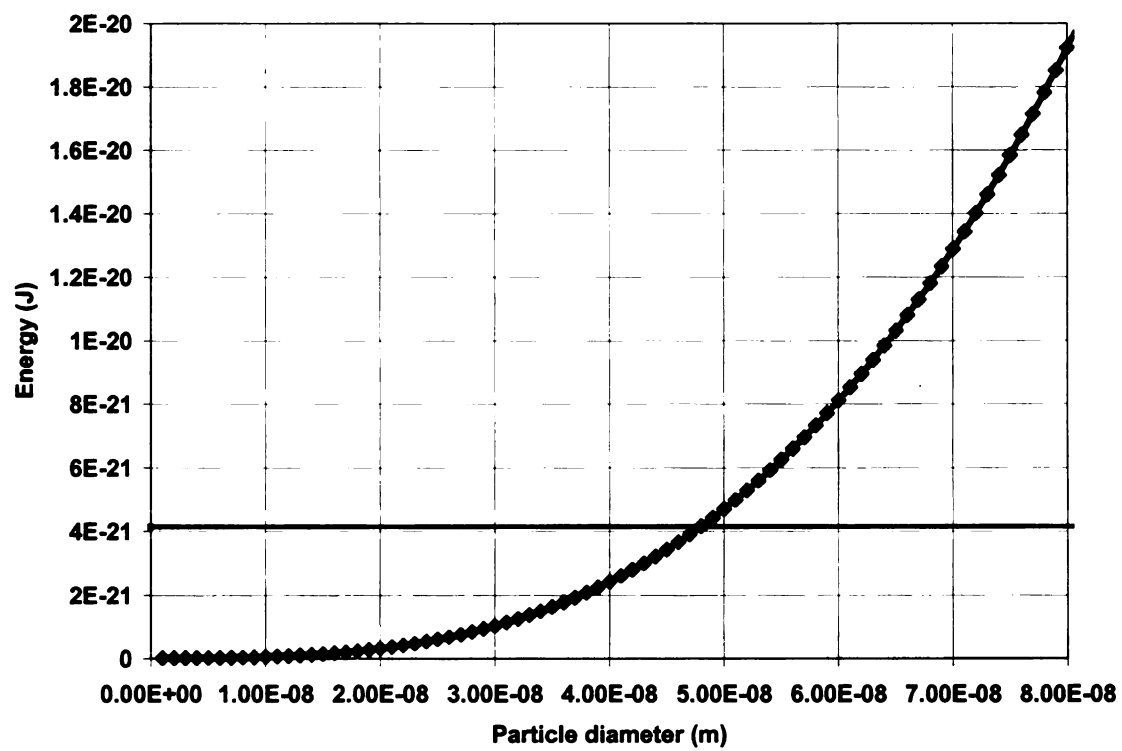


Figure 4.2 The energy of a cobalt nanoparticle interacting with the Earth's magnetic field as a function of its diameter (green) and the thermal energy (pink).

adding more. That is, the total Zeeman energy can be increased by adding more particles. This can be seen in the Magnetotactic bacteria where a single Magnetosome is not sufficient and is made up of 20 or more magnetite nanoparticles. The reason for the difference between the size and number of magnetite and cobalt nanoparticles are that the magnetic moment of a cobalt nanoparticle is greater than that of magnetite nanoparticle of equal mass.

Another energy that comes into play is the magnetostatic energy which is dipole-dipole interactions. The magnetostatic interaction energy for two magnetic dipoles is given by the equation [13]:

$$E_{ms} = \mathbf{m}_1 \mathbf{m}_2 (1 - \cos^2 \theta) / R^3$$

Where  $\mathbf{m}_1$  and  $\mathbf{m}_2$  are the magnetic moments of the two dipoles,  $R$  is the distance between them and  $\theta$  is the angle between them. The maximum range of values for the magnetostatic energy is  $\pm 2 |\mathbf{m}_1| |\mathbf{m}_2| / R^3$  where the negative sign represents an energy minimum where the magnetic dipoles are aligned parallel and in the same directions. The positive sign represents an energy maximum where the magnetic dipoles are aligned parallel but in opposite directions. The area between these two maximums is separated by many smaller maximums and minimums. In the Magnetotactic bacteria the moments of the magnetite nanoparticles are aligned parallel, minimizing the magnetostatic energy and maximizing the Zeeman energy. It is known that concentrated assemblies of nanoparticles have stronger magnetostatic effects than dilute assemblies, showing ferromagnetic ordering at room temperature [8]. These calculations are done based on single non-interacting particles, which work well for dilute

samples with narrow size distributions. When samples become concentrated predicting magnetic interactions and length of scale becomes complicated. It is difficult to discern which interactions are responsible for the observed magnetic properties, because in many cases several interactions can contribute to the same properties. The interactions of these assemblies will depend on their proximity to each other, which is dependent on their polymer coating. The closer they are to each other the stronger the interaction.

While the magnetic properties of individual non-interacting ferromagnetic nanoparticles can be well characterized based on size and shape, these properties change as large assemblies form and begin to interact. That is individual ferromagnetic nanoparticles that are superparamagnetic at room temperature can, when concentrated, also form ferromagnetic ordered assemblies with a net magnetic moment.

### **FMNCP and Bacterium Binding**

The effective binding of the FMNCP to its target bacterium presents three specific issues: specificity, affinity, and coverage. In order to discuss these issues we must first discuss how the FMNCPs bind the bacterium. The binding of the FMNCPs to the bacterium is accomplished by the use of surface recognition molecules (SRM), such as antibodies that are conjugated to the FMNCP. Surface recognition molecules bind to unique molecular structures presented on the surface of the bacterium known commonly as antigens when antibodies are used. Nearly all bacteria display unique molecular structures on their surfaces that are strain specific. These unique molecular structures are either polypeptide

or polysaccharide in composition depending on the bacterial species, with polysaccharide being the most common. One can use these unique molecular structures as antigens to the SRMs to provide specificity for a certain species. The issue of affinity, or how well the FMNCPs bind the pathogen, is addressed by the use of more than one SRM. The FMNCP can be formulated with different SRMs at ratios that reflect the pathogen's surface makeup. The use of SRMs that bind the same antigen but in different ways, in the fashion of polyclonal, antibodies can add to the FMNCPs affinity for a particular pathogen. The affinity of the individual SRMs can also be optimized using the methods and technology discussed in Chapter 1, such as antibody recombinant technology. The final issue is choosing an antigen that is sufficiently distributed throughout the cell membrane and is found in high enough numbers in order to maximize the signal.

Capsular polysaccharides (CPS), also known as K-antigens, are just such surface molecules (antigens), and can be found on a wide range of bacterial species [14]. The CPS with its unique chemistry and structure acts as a physical barrier protecting the cell against dehydration and is an important virulence factor in the pathogenicity of many bacteria [15]. Capsular polysaccharides have been used for serotyping bacterial species for well over fifty years. Serotyping is used to determine specific strains of bacterial species. Both gram positive and negative bacteria can have CPS. While the CPS can be used to identify specific species, it is not always strain specific. For example in our experiments we used *Rhizobium Trifolii* as our model organism. *Rhizobium Trifolii* is a gram negative soil bacterium capable of fixing nitrogen [16]. The CPS of *Rhizobium Trifolii* was



used as an antigen to generate antibodies/SRMs to the *Rhizobium Trifolii* to be used in the detection platform. The structure of the CPS produced by *Rhizobium Trifolii* has been determined (figure 4.3) [17, 18, 19]. While the CPS of *Rhizobium Trifolii* is species specific, it is not strain specific. That is it can be used to identify *Rhizobium* but it can not be used to differentiate between different strains of *Rhizobium*.

In cases where the CPS does not have the specificity that is needed or is not present other polysaccharides are used such as Lipopolysaccharides (LPS) (O-antigens) of gram negative bacteria, and cell wall glycopolymers (CWG) of gram positive bacteria [21] as well as capsular proteins. The structure of the LPS of *Rhizobium Trifolii* has been solved, along with several other surface polysaccharides of *Rhizobium* (figure 4.4) [ 22, 23, 24, 25, 26, 27]. LPS are made of three parts, the lipid A which acts as the hydrophobic anchor in the outer leaflet, the core which is made up of nonrepeating oligosaccharide and the O-antigen which consists of repeating polysaccharide units [21]. There is some debate about the use of SRM to identify bacteria, and that the surface molecular structures can randomly change or be engineered by man, making them a poor choice. This is not correct; as mentioned the CPS is an important virulence factor and changes will directly affect the pathogenicity. The cell surface molecules of pathogenic bacteria are essential to their virulence and are not likely to change. The truth is that variation in the makeup of living organisms is a result of entropy. The thermodynamic laws that govern our world favor disorder, which is why you will never find two identical bacteria. There will always be some difference in

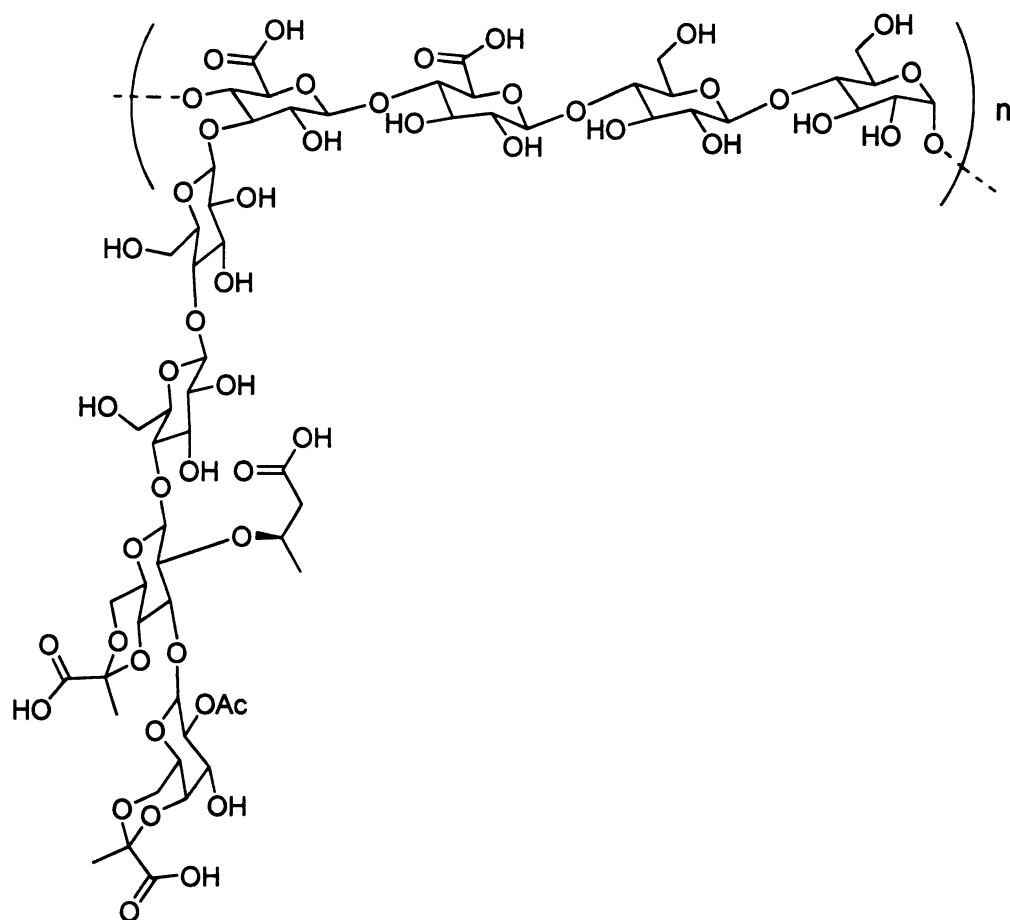


Figure 4.3 Structure of octasaccharide repeating unit of *Rhizobium trifolii* capsular polysaccharide [17, 18, 19].

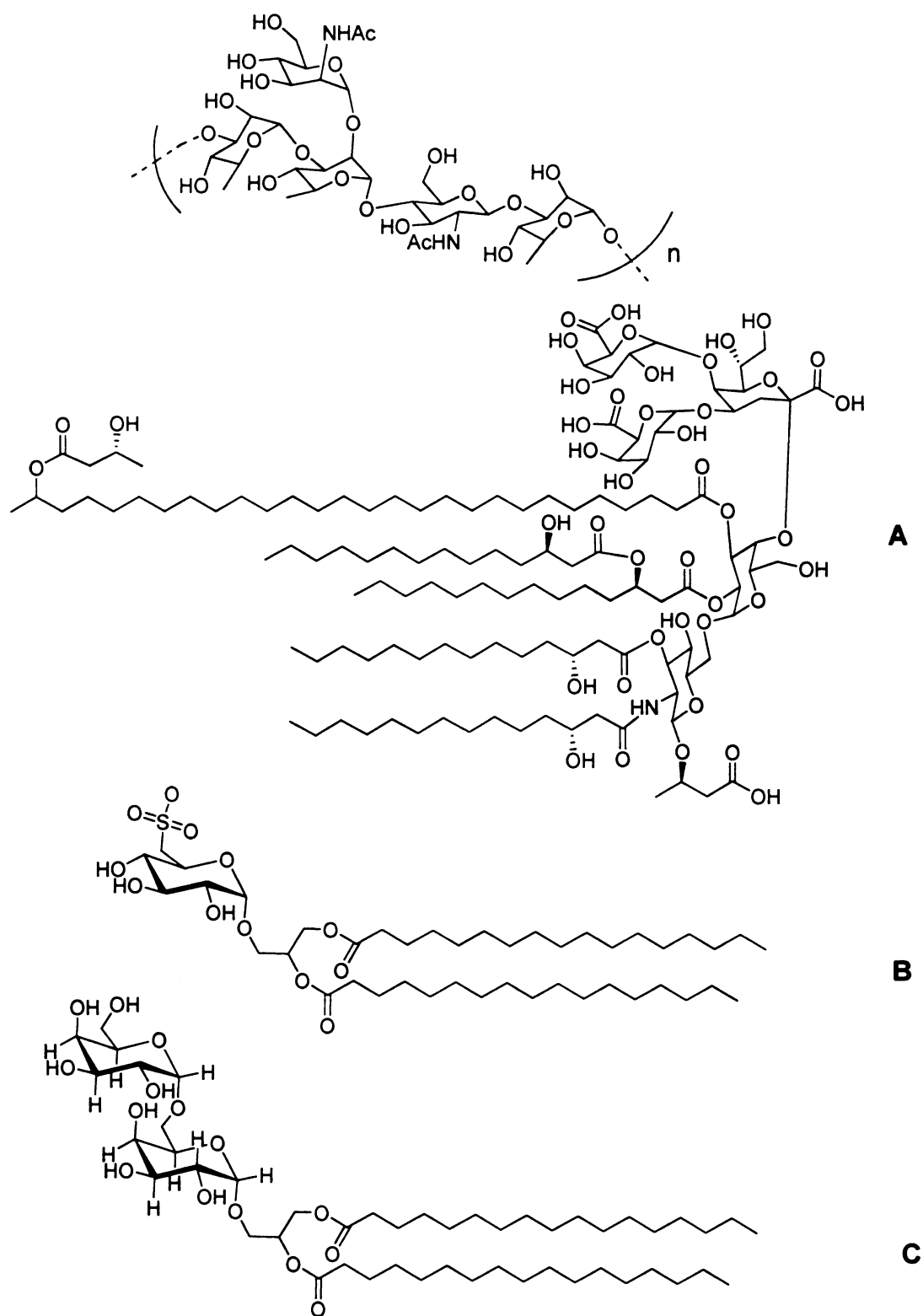


Figure 4.4 Structures of *Rhizobium* polysaccharides. Total *Rhizobium trifolii* 4S LPS Structure (A) [21, 22, 23, 24], sulfoquinovosyl diacylglycerol (B), digalactosyl diacylglycerol (C) [27, 28].

DNA, proteins, carbohydrates, etc. This is why questions of random changes or genetic modification in target surface molecules are trivial. One cannot plan or anticipate all possible chance happenings, and no one method of detection is exempt from this, whatever the specific target maybe it is subject to the consequences of entropy.

## **Experimental**

**Synthesis of Gold Nanoparticles** - The polymer scaffold materials A and B (0.335 g) were dissolved in water (6.65 g) to make a 3.35% w/w solution. In a 12 well tissue culture plate, a gold (III) chloride (825, 412, and 206  $\mu\text{M}$ ) solution was placed in the first 3 columns decreasing in concentration from top to bottom rows. The fourth column contained equivalent volumes of water. Polymer scaffold material B (20  $\mu\text{L}$ ) was added to each well in the first column and row one of the fourth column. Polymer scaffold material A (20  $\mu\text{L}$ ) was added to each well in the second column and row two of the fourth column. Borane in THF (3 drops) was added to each well of the plate. The experiment was repeated, substituting sodium borohydride (0.01 M) as the reducing agent.

**Synthesis of cobalt nanoparticles** - Cobalt nitrate (30 mM) was added to six vials labeled A 1-6 (0.3, 0.2, 0.1 0.3, 0.2, 0.1 mL) and adjusted to a final volume of 3 mL. A second set of six vials labeled B 1-6 had sodium hydroxide (0.2 M, 0.1 mL) added to each vial. To the second set of vials number 1-3 polymer scaffold material B (0.06 mL, 5% w/w) was added. The second set of vials was adjusted to a final volume of 3 mL. Sodium borohydride (0.01 M, 0.2 mL) is added to all six of the first set of vials

containing the cobalt nitrate solutions. After adding and mixing the sodium borohydride, the corresponding numbered vial of the second set is then added and mixed.

Antibody synthesis - Keyhole limpet hemocyanin (10 mg) and *Rhizobium trifolii* CPS (2 mg) are dissolved in a sodium acetate buffer solution (pH 4) with stirring at 25 °C for 1 hour. Sodium cyanoborohydride (2 mg) was added to the mixture and left to stir at 25 °C for 36 hr. The reaction mixture was dialyzed using 3500 MWCO tubing for 48 hrs, changing the water every 2 hours for the first 8 hours, and then every 4 hours. The solution was then lyophilized and sent to Antibodies Incorporated. Antiserum produced was made in rabbits and consisted of one test bleed and one production bleed. Binding of antibodies was checked using heat treated *Rhizobium trifolii* and FITC labeled anti-rabbit antibody.

Nanocomposite Synthesis - Cobalt nanoparticle suspension (60 mL) was concentrated down to 15 mL. The suspension was then dialyzed against water (500 mL) using a dialysis chamber with continuous flow (0.5 mL/min). The suspension was then dialyzed against a solution of sodium phosphate (20 mM, pH 4, 300 mL) using the same dialysis chamber with continuous flow. Dialyzed suspension (1 mL) is then added to two micro tubes which each contain 1-ethyl-3-[3-dimethylaminopropyl] carbodimide (EDC) (30 mg), and the mixture was left to stir for 1 hour. The mixture is then centrifuged (30 sec, 6000 rpm), the supernatant is discarded, and the pellet is resuspended in phosphate buffered saline (PBS) (1 mL). Antibody serum (200 µL) is then added to one tube and an antibody solution (3.5 mg/mL, 200 µL) added to the other as a control, and was

stirred 18 hours at 4 °C. The mixture is then centrifuged (30 sec, 6000 rpm), the supernatant is discarded, and the pellet is resuspended in phosphate buffered saline (PBS) (1 mL), and the suspension is stored at 4 °C. SEM samples were prepared in one of two ways. First *Rhizobium trifolii* cells were heat fixed to a carbon coated glass slide, to which one to two drops of the nanocomposite suspension was added and incubated for 1 hr. Then the samples were washed first with PBS and then with water, and let dry. In the second method the nanocomposite suspension was mixed with a suspension of *Rhizobium trifolii* cells, and left for 18 hours at 4 °C. The samples were then centrifuged (30 sec, 6000 rpm), the supernatant discarded, and the pellet resuspended with water (1 mL). The samples were then pipetted (5 µL) to carbon coated slides for SEM and nickel grids for TEM and let dry.

## **Results and discussion**

Once the macromolecular polymer system had been synthesized, experiments could begin using it to make nanoparticles. The first experiments were done using gold. As mentioned before, sulfur groups have a high affinity for transition metals with gold having the highest. The ability of the polymer scaffold to stabilize metal nanoparticles in suspension was first tested using gold as the core of the nanoparticle. Gold nanoparticles suspensions also have distinctive colors depending on the size of the particles, which is a good litmus test as to whether or not nanoparticles have formed. The first experiment used two forms of the polymer, one with free carboxylic acid groups, and one in which the carboxylic acid groups were converted to methyl ester groups. Figure 4.5 shows

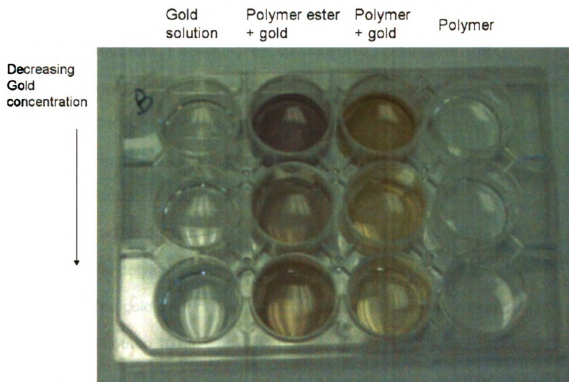


Figure 4.5 Gold nanoparticle suspensions and controls. The 1<sup>st</sup> column is a gold control with no polymer, the 2<sup>nd</sup> is gold with the methyl ester polymer, the 3<sup>rd</sup> is gold with the carboxylic acid polymer, and the 4<sup>th</sup> has both polymers with no gold as controls. The concentration of gold decreases as you move from the top of the column to the bottom. The gold solution were reduced using sodium borohydride.

the gold nanoparticle suspensions and their controls. The gold control samples with no polymer precipitated out, whereas the gold/polymer samples formed gold nanoparticle suspensions. The methyl ester polymer formed purple colored suspensions whereas the carboxylic acid polymer formed more gold to straw-colored gold suspensions. Over a few days the methyl ester polymer did begin to show some precipitation at the highest concentrated suspension. The suspensions were dried and formed a film on the bottom of the plate. Pieces of the film from the dried suspensions were subjected to fluorescent confocal microscopy (Figure 4.6). The fluorescence of the film pieces at different wavelengths indicated that there was a distribution of different sized nanoparticles within the film. Images of the gold nanoparticles tells us that the macromolecular polymer system stabilizes gold nanoparticles in a aqueous suspension. The gold color of the gold nanoparticle suspension indicates that particles smaller than 10 nm were formed.

Once the macromolecular polymer system was shown to be capable of facilitating the formation and stabilization of gold nanoparticles, it was next used in experiments with ferromagnetic metals. Experiments using cobalt, macromolecular polymer system solutions yielded stable nanoparticle suspension (figure 4.7). The cobalt nanoparticles were also shown to have ferromagnetic properties; when a magnet was placed next to the sample, the particles were pulled to, and accumulated on the, side where the pole of the magnet was located (figure 4.8). Small amounts of precipitation were observed in some of the samples after 1 to 2 weeks, though all suspensions maintained their



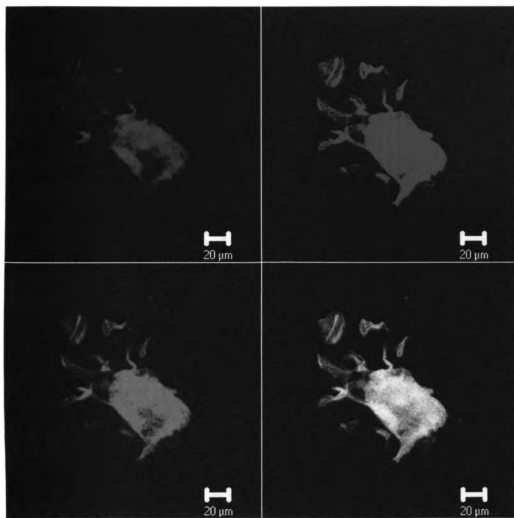


Figure 4.6. Fluorescent confocal microscopy images of a dried piece of the gold nanoparticle suspension. The top left shows the florescence with 488 nm light; the top right at 633 nm. The bottom left is at 543 nm, and the bottom right is an overlay of all three. Images taken with a Zeiss LSM 5 PASCAL confocal microscope.

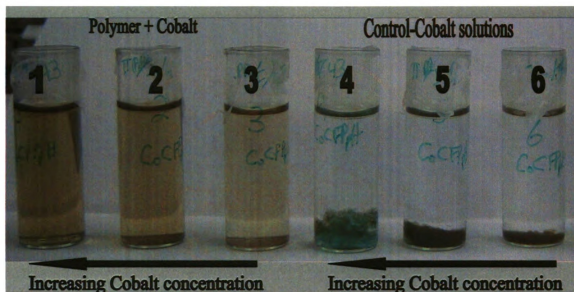


Figure 4.7. Cobalt nanoparticle suspensions (1-3) were made with polymer and cobalt solutions mixed and reduced using sodium borohydride. The controls (4-6) contained the same concentrations of cobalt solution and were reduced using sodium borohydride. The controls did not have any polymer in them.

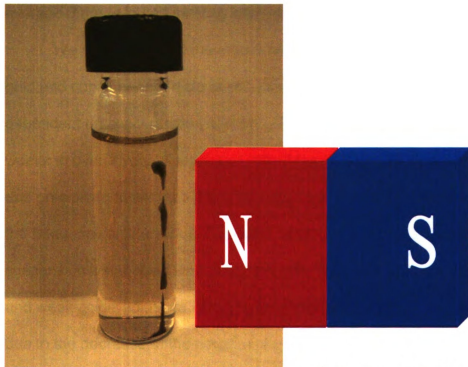


Figure 4.8. Cobalt nanoparticle suspension after a bar magnet has been removed from its side. There is a dark line where the particles have been concentrated in response to the magnet.

gold color. Many of the suspensions were stable after 1 year. Stability seems to depend on concentration and pH, with higher concentration samples precipitating faster, as one would expect from a particle stabilized by a protein mimetic polymer. The suspensions would precipitate at pH 3 and below but were stable at neutral to high pH. The sizes of the cobalt nanoparticles was determined to be on average 3 nm using a tunneling electron microscope (TEM) (figure 4.9).

We have seen that the macromolecular polymer system stabilizes both gold and cobalt nanoparticle suspensions. The stability of the nanoparticles is dependent on concentration and pH, with suspension stability ranging from a few weeks to over a year. Suspensions of higher concentration tended to aggregate and precipitate faster than those of lower concentration. At higher concentrations the frequency of interaction increased, which increased aggregation. The suspension's stabilities also varied with pH; they were stable in basic, neutral, and weak acidic solutions, but quickly precipitated out at pH 3 and below. This is due to the decrease of the negative charge on the particles; as the pH is lowered the number of protonated carboxylic acid groups increases which reduces the charge on the particles allowing them to aggregate.

An interesting result was that some of the cobalt nanoparticle suspensions depending on their concentration after some time (more than two weeks), formed needle-like structures. Using the confocal microscope to look at these newly formed structures, the needle-like structures were determined to be tubules, which had formed from sheets of the polymer that had rolled up upon themselves. Cobalt nanoparticles were incorporated into the polymer sheets and

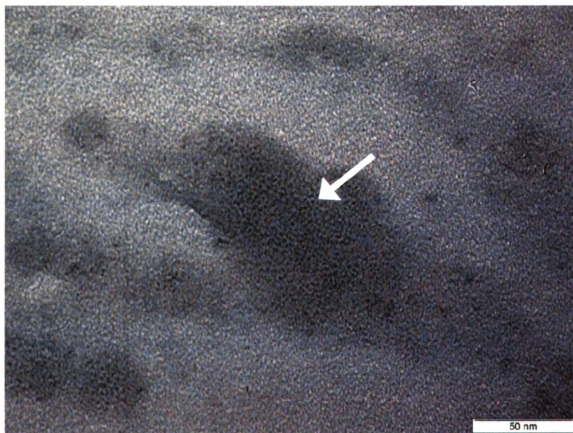


Figure 4.9 TEM image of dried cobalt nanoparticle suspension with particle and average particle size of 3 nm. The image was taken with a JEOL 100 CXII.

tubules, making them magnetic. At higher magnification, thousands of micron and submicron sized particles were observed moving (Brownian motion) around and inside the tubules. The micron and submicron sized particles were mainly concentrated inside the tubules and at their ends. This concentration of particles was due to the magnetic field that is made by the tubules. The particles, when exposed to an external magnetic field, became ordered and lined up with the magnetic field (figure 4.10). The magnetic particles in and around the tubules are clusters of cobalt nanoparticles whose magnetic forces had caused aggregation despite their charged polymer coating.

TEM images showed that the metal core of the cobalt nanoparticle has an average diameter of 3 nm. From this we can calculate the particle's magnetic energies as well as some projected values for comparison with experimental results. Knowing that the core is less than 3 nm we may assume that it is superparamagnetic, nevertheless we can still calculate the anisotropy energy. The anisotropy energy for a 3 nm cobalt particle is  $5.8 \times 10^{-21}$  J. This is a little bigger than the thermal energy of  $4.14 \times 10^{-21}$  J. We can use the Neel-Brown expression to determine if a ferromagnetic nanoparticle is in a paramagnetic state or a blocked state. Remember that the state is relative to the experimental time. Our experimental time was 0.1 s and the relaxation time was determined to be  $4.06 \times 10^{-9}$  s, which is far less than the experimental, meaning that the cobalt core particles are superparamagnetic.

In some of the cobalt samples, needle like structures formed. Closer examination of the needle structures showed them to be hollow with micron size

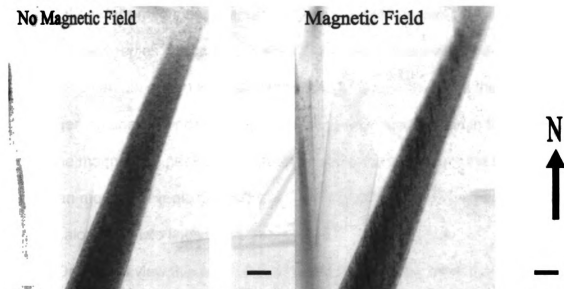


Figure 4.10. The confocal image on the left is of one of the tubules with particles randomly concentrated inside of it and at the ends. The image on the right is the same tubule but in a magnetic field, the particles have become aligned with the magnetic field (bar scale 20  $\mu\text{m}$ ).

and smaller particles moving in and out of them and concentrated at the ends of the needles. Exposure of the sample to a magnet caused the needles as well as the particles to align with the magnetic field. The hollow magnetic needles are the result of polymer sheets formed from the polymer scaffold material that has rolled up on its self. As the sheets are formed they incorporate the cobalt nanoparticles making them ferromagnetic. The earth's magnetic field causes the magnetization of the hollow needles, which in turn act like hollow bar magnets. The particles seen in the sample are aggregates of the cobalt nanoparticles, as the particles get bigger, so does the net moment, increasing its magnetization in the earth's field. The magnetized particles are pulled to the ends or poles of the needles. Brownian motion prevents the particles from fully aligning and keeps the particles moving along the field lines of the needles.

One might view this as an interesting side note, but I think that it helps to demonstrate an important point. That is, the magnetic behavior of the cobalt nanoparticles in large assemblies. We know that the cobalt nanoparticles are superparamagnetic and the magnetic energy of the earth's magnetic field and an individual particle's field is less than the thermal energy. The magnetic energy can increase as the particle gets bigger (more and more particles add to the aggregate) to the point where the magnetic energy is higher than the thermal energy. We can see this in our results, that the particles as well as the needles are magnetized by the earth's magnetic field. The magnetic energy is strong enough to overcome the thermal agitation of the cobalt nanoparticles. We can expect to see similar results with the nanocomposite bound to the bacterium. The



nanocomposites by themselves will have no net moment in the earth's field but as they accumulate on the bacterium the net moment will increase to the point where the magnetic energy is stronger than the thermal energy causing the bacterium to align with the earth's field.

In order to make the final nanocomposite, we must obtain antibodies for our model organism *Rhizobium trifolii*. The CPS of *Rhizobium trifolii* was conjugated to the carrier protein keyhole limpet hemocyanin (KLH). The CPS conjugate was used for the production of the antibodies by Antibodies Incorporated. Antibodies Incorporated produced the antibody serum used. Two test immunopurifications were done on the serum, one using a salt gradient and the other using a pH gradient. In order to determine what fractions contained the antibodies, AUN 843 cells were heat fixed to microscope slides and incubated with the fractions, then they were incubated with an anti rabbit antibody labeled with FITC. The slides were then examined under a fluorescent microscope. The slides showed poor separation of fractions. The pure serum was then tested along with purified antibodies (figure 4.11). While the antibody serum was shown to bind the *Rhizobium trifolii* it did not have the intensity of the purified antibodies. This is due to differences in concentration between the serum and purified antibodies. The serum, while binding the CPS, is just not concentrated enough to show the same intensity.

Once the binding was confirmed, the antibodies could be incorporated into the final nanocomposite. The antibodies were conjugated to the polymer coated cobalt nanoparticles using the coupling agent 1-ethyl-3-[3-dimethylaminopropyl]-

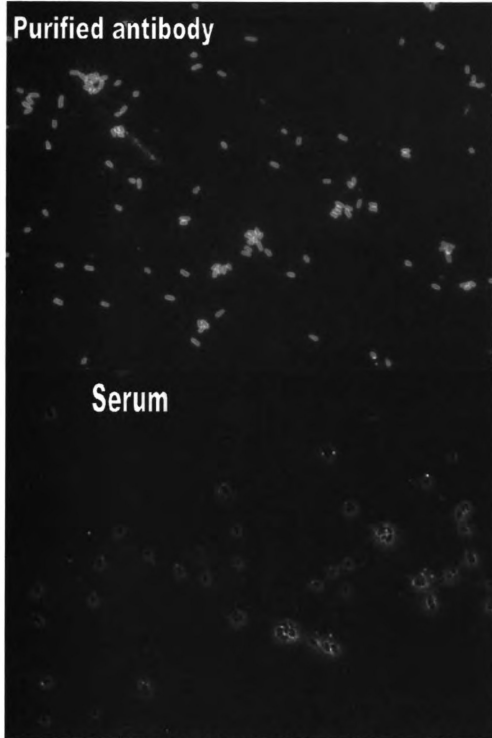


Figure 4.11 Antibody evaluation using FITC-labeled goat anti-rabbit antibody of antibodies raised to capsular polysaccharide.

-carbodiimide (EDC), to make the final nanocomposite. The final treatment and modification does decrease the stability of the nanocomposite in suspensions, which tend to form large aggregates which can be resuspended. The binding of the nanocomposite with the *Rhizobium trifolii* was tested by mixing the two together, and samples were placed on nickel grids for TEM and carbon coated glass slides for SEM. Figure 4.12 shows the *Rhizobium trifolii* control SEM image. Figure 4.13 shows the nanocomposite and *Rhizobium trifolii* samples, the top image shows a large agglomeration of the nanocomposite with the *Rhizobium trifolii* cells. The bottom image is of several *Rhizobium trifolii* cells coated with nanocomposite. Figure 4.14 shows the cells coated with the nanocomposite as well as large nanocomposite aggregates. Figure 4.15 shows the *Rhizobium trifolii* control TEM image. Figure 4.16 is a TEM image of the nanocomposite and *Rhizobium trifolii* sample, showing four cells coated with nanocomposite. Figure 4.17 shows the TEM image of the nanocomposite and *Rhizobium trifolii* mix, the nanocomposite has large concentrations around the sides of the cells.

The side chains of the polymer scaffold provided attachment sites for the conjugation of antibodies to form the nanocomposite. The specificity of our device relies on polyclonal antibodies as opposed to monoclonal. Polyclonal antibodies will give the nanocomposite some flexibility in binding. By not requiring the exact conformation for binding the antigen it will increase the number of antibodies capable of binding. Conjugation of the antibodies to the nanoparticles

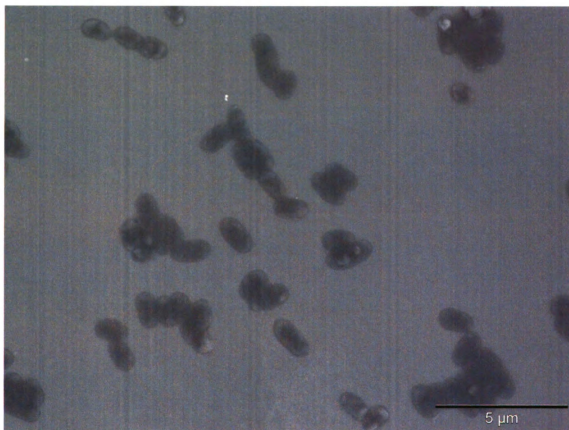
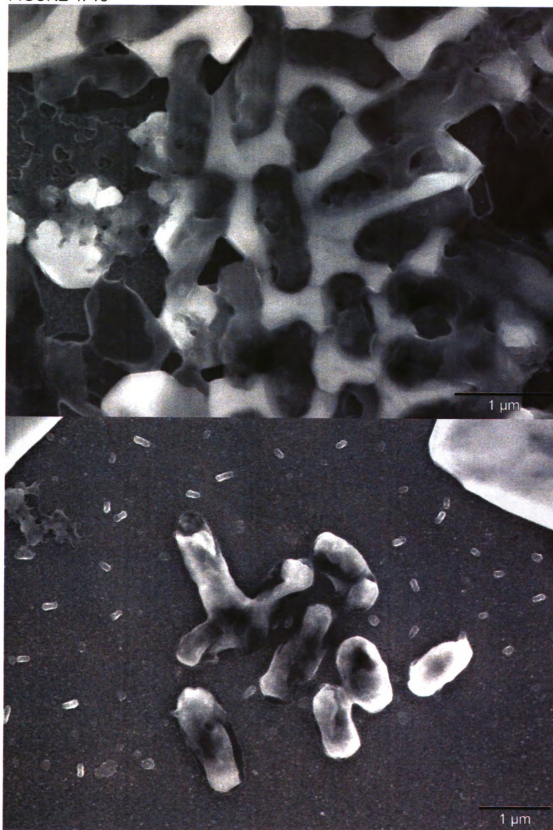


Figure 4.12 SEM image of heat fixed *Rhizobium trifolii* cells.

Figure 4.13 SEM images of nanocomposite and *Rhizobium trifolii* mix samples. The top image shows a large agglomeration of the nanocomposite with the *Rhizobium trifolii* cells. The bottom image is of several *Rhizobium trifolii* cells coated with nanocomposite.

FIGURE 4. 13



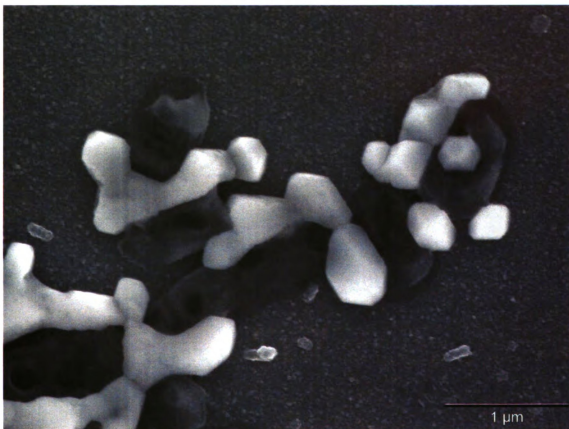


Figure 4.14 SEM image of nanocomposite and *Rhizobium trifolii* mix, the cells are coated with the nanocomposite as well as large nanocomposite aggregates.

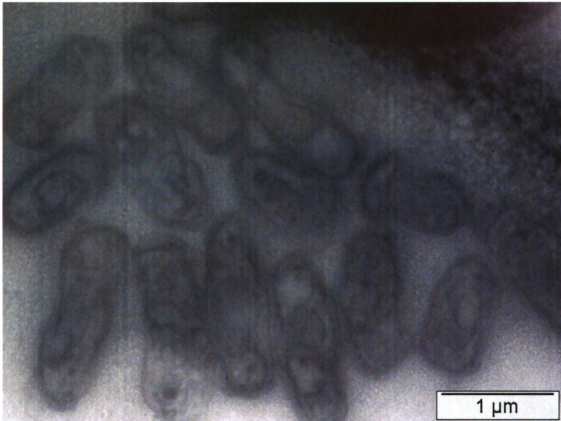


Figure 4.15 TEM image of *Rhizobium trifolii* control.





Figure 4.16 TEM image of the nanocomposite and *Rhizobium trifolii* sample, showing four cells coated with nanocomposite.

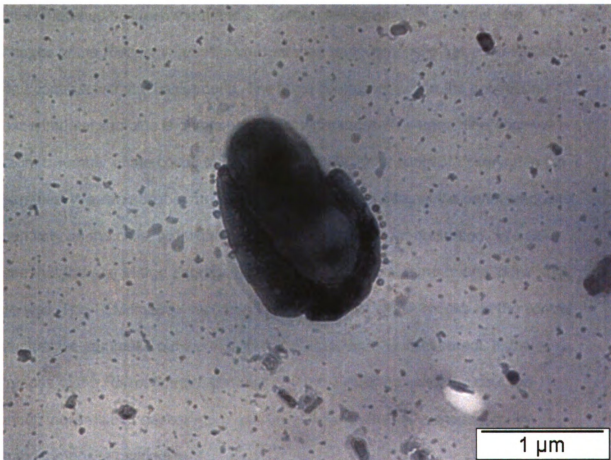


Figure 4.17 TEM image of nanocomposite *Rhizobium trifolii* mix. With a large concentration of nanocomposite around the cell.

decreases the nanocomposites electrostatic repulsion, increasing the rate of agglomeration and precipitation. Pipetting and vortexing is sufficient to resuspend the samples. The SEM images of the nanocomposite and *Rhizobium trifolii* cells clearly show the nanocomposite coating the cells surface. The cells of the control appear flat looking almost like shadows on the slide, as one would expect to see little difference between them and the carbon background. In contrast, the images of the *Rhizobium trifolii* mixed with the nanocomposite has a 3D surface and contrast with the background. The large contrast between the control and experimental samples is due to elemental differences. The large difference in atomic number of the cobalt to the carbon results in the contrast observed in the samples. We can see that the concentration and thickness of the nanocomposite can vary on the cells, with light areas indicating higher concentration. We also see that there are large aggregates of nanocomposite that are bound to the cells as well. The TEM images support what is seen in the SEM images. In the control images we can make out the cells but they are relatively transparent. In the images of the *Rhizobium trifolii* mixed with the nanocomposite, the cells are much more visible, appearing darker than the controls due compared to the nanocomposite coating.

## REFERENCES

6. S. Link , M.A. El-Sayed, Shape and Size dependence of radiative, non-radiative and photothermal properties of gold nanocrystals. *INT. Reviews in Physical Chemistry*, Vol:19 Issue:3 pg:409-453, 2000.
7. E. Roduner, Size matters: why nanomaterials are different. *Chemical Society Reviews*, Vol:35 Issue:7 pg:583-592, 2006.
8. American Institute of Physics Hand book, McGraw-Hill book company Inc, 1957, pg:5-208.
9. A.H. Lu, E.L. Salabas, F. Schuth, *Magnetic Nanoparticles: Synthesis, Protection, Functionalization, and Application*. *Angew. Chem. Int. Ed*, Vol:46 Issue:8 pg:1222-1244, 2007.
10. K.M. Krishnan, A.B. Pakhomov, Y. Bao, P. Blomqvist, Y. Chun, M. Gonzales, K. Griffin, X. Ji, B.K. Roberts, *Nanomagnetism and spin electronics: materials microstructure and novel Properties*. *J Mater Sci* 41 pg:793-815, 2006.
11. G. Li, V. Joshi, R. L. White, S. X. Wang, J. T. Kemp, C. Webb, R. W. Davis, S. Sun, *Detection of single micron sized magnetic beads and magnetic nanoparticles using spin valve sensors for biological applications*. *Journal of Applied Physics*, Vol:93, #10 pg:7557-7559, 2003.
12. A. Lu, E.L. Salabas, F. Schuth *Magnetic nanoparticles: Synthesis, Protection, Functionalization, and Application*. *Ange. Chem. Int. Ed*. Vol:46 pg:1222-1244, 2007.
13. S.A. Majetich, M. Sachan, *Magnetostatic interaction in magnetic nanoparticle assemblies: energy, time and length scales*. *J. Phys. D: Appl. Phys.* Vol:39 pg:R407-R422, 2006.
14. Y.W. Jun, J.W. Seo, J. Cheon, *Nanoscaling laws of magnetic nanoparticles and their applicabilities in biomedical sciences*. *Accounts of chemical research*. Vol:41, No2 pg:179-189, 2008.
15. R.B. Frankel, *Magnetic Guidance of Organisms*. *Annual Review of Biophysics and Bioengineering*, Vol:13 pg:85-103, 1984.
16. D.A. Bazylinski, R.D. Frankel, *Magnetosome Formation in Prokaryotes*. *Nature Reviews Microbiology* Vol:2 Issue:3 Pges:217-230, 2004.
17. C. Kittel, J.K. Galt, *Ferromagnetic Domain Theory*. *Solid state physics* Vol:3, 1956.

18. D.C. Mattis, The Theory of Magnetism Made Simple. World Scientific, New Jersey, 2006.
19. I.S. Roberts, The biochemistry and genetics of capsular polysaccharide production in bacteria. Annu. Rev. Microbiol. Vol:50 pg:285-315, 1996.
20. Y.S. Ovodov, Bacterial capsular antigens structural patterns of capsular antigens. Biochemistry (Moscow), Vol:71, No:9, pg:937-954, 2006.
21. F.B. Dazzo, G.L. Truchet, Interactions of Lectins and their saccharide Receptors in the Rhizobium-Legume Symbiosis. J. Membrane Biol. Vol:73, pg:1-16, 1983.
22. R.I. Hollingsworth, M. Abe, J. Sherwood and F.B. Dazzo. Carbohydrate Research Vol:134 pg:C7-C11 (1984).
23. R.I. Hollingsworth, A. Mort and F.B. Dazzo. Journal of Bacteriology Vol:169 pg:3369-3371, 1987.
24. Hollingsworth, R.I., and Dazzo, F.B., Hallenga, K. Musselman, B. Carbohydrate Research, Vol:172, pg:97-112, 1988.
25. C. Weidenmaier, A. Peschel, Teichoic acids and related cell-wall glycopolymers in Gram-positive physiology and host interactions. Nature, Vol:6 pg:276-287, 2008.
26. C.R.H. Raetz, C. Whitfield, Lipopolysaccharides Endotoxins. Annu. Rev. Biochem, Vol:71 pg:635-700, 2002.
27. R.I. Hollingsworth and R.W. Carlson, J. Biol. Chem Vol:264 pg:9300-9304, 1989.
28. R.I. Hollingsworth, R.W. Carlson, F. Garcia and D. Gage. J. Biol. Chem, Vol:264 pg:9294-9299, 1989.
29. The structure of the O-antigenic chain of the lipopolysaccharide of Rhizobium trifolii 4s. Wang, Y. Hollingsworth, R.I. Carbohydrate Research. Vol:260, issue:2 pg 305-317, 1994.
30. Y. Wang Ph.D. Thesis, Michigan State University East Lansing, MI, 1995
31. Y. Tang, R.I. Hollingsworth, Digalactosyl diacylglycerols, plant glycolipids rarely found in bacteria, are major membrane components of bacteroid forms of *Bradyrhizobium japonicum*. GlycoBiology Vol:7, no:7, pg:935-942, 1997.

32. R.A. Cedergren, R.I. Hollingsworth. Occurrence of sulfoquinovosyl diacylglycerol in some members of the family *Rhizobiaceae*. Journal of lipid research, Vol:35 pg:1452-1461, 1994.

## Chapter 5

### The Detection System

#### Introduction

The design of the detection system is based on magnetic sensing of a bacterium that has been magnetically augmented by ferromagnetic nanocomposite particles. Magnetic sensing is the keystone of our detection platform. Magnetic sensors are used to control and analyze thousands of functions, and can be found everywhere from cars to cell phones. There are many types of magnetic sensors of varying form and function. Here we discuss some different types of magnetic sensors and their limits of detection.

Giant magnetoresistance sensors are very useful and are used as read/write heads in computer hard drives. Giant magnetoresistance sensors are made up of a sandwiched four part electrode. There are two ferromagnetic layers separated by a nonmagnetic conductor. The fourth part is an antiferromagnetic layer on one of the ferromagnetic layers. The antiferromagnetic layer pins the ferromagnetic layer, holding its magnetization in one direction. This ferromagnetic layer is said to be hard, where the other layer is said to be soft. The soft layer is susceptible to magnetization by external fields. The function of a GMR sensor is as follows, if the magnetic fields of the ferromagnetic layers are in a parallel configuration then the resistance does not change. If an external field magnetizes the soft ferromagnetic layer antiparallel to the hard layer then the resistance will increase. GMR sensors are also very sensitive with detection

limits in the hundreds of picotesla range [1] as well as having a high on chip density of 0.1-1 million sensors per square centimeter [2].

Hall Effect sensors are based on the Hall Effect as the name implies. The basic principle of the Hall Effect is that when a current is passed through the length of a thin rectangular shaped conductor, and a magnetic field is applied perpendicular to the plane of the sheet, a potential appears on the opposite edges of the rectangle. This potential is proportional to the current flowing through the conductor and the magnetic flux. Hall Effect sensors have been produced with detection limits in the picotesla range (10 pT) [3]. Hall Effect sensors are easily integrated on silicon chips making them inexpensive and easy to use.

Fluxgate magnetometers are widely used in compass based navigation systems because they can measure the intensity and orientation of the lines of flux. Fluxgate magnetometers are made up of two parallel ferromagnetic cores each wound with a primary coil, with one of them wound in reverse. A secondary coil then surrounds the primary coil and is attached to an amp meter. The primary coil is attached to an AC current. The induced field of the primary coils is canceled out and there is no change measured in the secondary coil. When exposed to an external magnetic field there will be some component in the direction of one of the cores and a separate component opposing in the other. This difference will cause a magnetic field that induces a voltage in the secondary coil, allowing the magnetic field to be measured. Fluxgate



magnetometers have been made with detection limits in the picotesla range (0.015 nT) [4].

Atomic magnetometers (also called optically pumped magnetometers) are made up of alkali metal (Rubidium, or cesium) vapor cells, through which linear polarized laser light passes and is detected by a photodiode. The linear polarized laser light causes a polarization of the alkali metal vapor atoms, this polarization is disrupted when the atoms are exposed to a magnetic field, resulting in a modulation of the intensity of the transmitted light. The modulation or resonant response of the atoms gives a measure of the Larmor frequency. The magnetic field is then determined by the Larmor or precession frequency.

Smaller chip scale atomic magnetometers have been developed with picotesla detection limits [5]. Atomic magnetometers are some of the smallest sensors (3 mm<sup>2</sup>) with the lowest detection limits.

The search coil is one of the simplest and oldest magnet sensors and has a broad dynamic range. Search coil sensors are based on Faraday's Law of Induction, which states that the voltage induced in a coil is proportional to the change in the magnetic flux in the coil. Coil based sensors have sensitivity in the hundreds of femtotesla range [6].

Frequency based detection is also useful; Fourier transform can be used to pick up frequency dependent signals that are buried in the noise. Many of the above sensors make use of this to filter out noise. The widespread use of magnetic sensors has driven the development of improved and smaller sensors, and one can only expect this trend to continue. We can see that there are many

magnetic sensors available with the sensitivities far below that which we would expect to see from the bacterium coated with the FMNCPs. For this detection system a search coil is used for its magnetic sensor, as the design was discussed in chapter 2. The simplicity and sensitivity of search coils make them an excellent chose.

## **Experimental**

Spinning coil in the Earths field – The coil was mounted on a ruler which was rotated about an axis parallel to a level plane. The coil was rotated by an electric motor with a constant speed, located approximately 2 feet away. The speed of the coil was varied by changing the radius of the rotating coil. The voltage was recorded as the coil was spinning in the earths field for several different radius.

Testing Magnetic Beads - A dilution of the stock magnetic beads suspension was made (1 to 1000) using PBS. Magnetic beads used were 1  $\mu\text{m}$  BcMag amine-terminated magnetic beads made by BioClone Inc. From the diluted stock suspension serial dilutions of 1 to 10 were made to make a total of eight samples. Each sample dilution (5  $\mu\text{L}$ ) was loaded in the detection platform, starting with the lowest and going to the highest. Measurements were taken over a 5 min period. In between samples, 10 mL of PBS were pumped through the system to wash it out.

Testing Nanocomposite Material - A turbid suspension of *Rhizobium trifolii* was made using a PBS solution. Using the suspension, 1 to 10 serial dilutions were made for a total of 6 sample. The *Rhizobium trifolii* were grown up on

Modified Bergensen's medium (BIII) agar plates at 28 °C for 5 days. Aliquots (100 µL) from each of the last three dilutions were then plated on BIII plates and were later counted to determine the number of viable cells in the samples. The nanocomposite suspension was then loaded into the detection platform. The *Rhizobium trifolii* suspension samples (4 µL) were then loaded in to the detection platform starting from the lowest concentration to the highest. Measurements were taken for 5 minutes before the next sample was added. The control experiment was done following the same procedures above with *Escherichia coli* used in place of *Rhizobium trifolii*.

Control experiment one - An experiment was run using different water samples, tap water, rusty tap water, milliQ water, deionized water, as well as some sodium chloride solutions of different ionic strengths (0.001, 0.01, 0.1, 0.5, 1 M). For this control the speed of the pump started at 0 then 5 then 10 and then back down to 5 then 0, the speed was changed every 5 min. The same pump profile was used when the pump was run in reverse.

Control experiment two - An experiment was performed to measure the voltage of the nanocomposite suspension at 3 different dilutions. The nanocomposite suspension was prepared as stated in chapter 4, and 2 dilutions were made to give three samples (1, 1/2, 1/10). The voltage was measured for five minutes with the different nanocomposite suspensions at speed 5 and 10.

Control experiment Three – An experiment was run to measure the voltage induced by the different concentrations of *Rhizobium Trifolii* cells.

Different concentrations of cell suspensions were made the same as in previous experiment, and samples were analyzed using the same parameters as well.

## **Results and Discussion**

The fabrication of the device consisted mainly of acquiring the individual components. The pump used was a Buchler instruments peristaltic pump. The voltmeter used was a Keithley 2182 nanovoltmeter. The meter was controlled and measurements were recorded using a Labview program. The coil had to be fabricated in house, consisting of a capillary tube with 3000 turns. The coil was placed into a Faraday cage, leads were cleaned and connected, as well as all the tubing, and all was assembled for testing.

Knowing that the earth has a magnetic field of  $5 \times 10^{-5}$  T, and that magnetotactic bacteria produce fields 20 to 30 times greater than this. And that a bacterium coated with the FMNCPs has fields equal to or greater than those of the magnetotactic bacteria. We can see that if our coil can detect the earth's field and it moves through it, then the coil can detect the FMNCP coated bacterium. In order to see what effect the earth's magnetic field had on the coil, the voltage was measured as it cut the earth's magnetic field at different velocities. Figure 5.1 shows the induced voltages of mechanically spinning the coil in the earth's field at different speeds, along with theoretical values. Looking at the trend lines fitted to the data we see that the slope of the mechanically spun data is less than that of the theoretical data, as well as a large y intercept value of about 800 nV. This large value can be attributed to the noise produced by the electric motor used to spin the coil. The coil was also spun by hand as well and fitted with

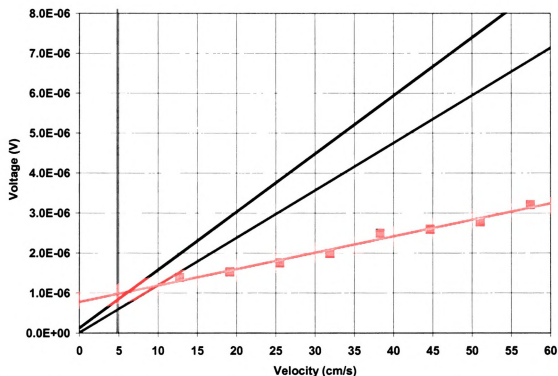


Figure 5.1. Graph of Voltage vs. Velocity. The pink squares are the voltages induced in the coil while spun in the earth's field at different velocities, and the orange line is a line of best fit to the data. The green line is the line of best fit for the hand spun data. The blue line is the expected theoretical induced voltage in the coil by the earth's field at different velocities. the vertical light blue line represents the velocity of the nanocomposite particles through the coil.

a line. The line for the hand spun data has a slope that is close to that of the theoretical, which is good considering the conditions (unshielded) with a intercept of 121 nV. While we may think that this is still high, it can be accounted for if we think about what we know about the earth's core. The rotation of the inner core is 3 to 2 ° per year faster than that of the earths crust [7, 8]. This works out to be about half a mile per day or 1.06 cm/s. Using this information we have determined that a voltage of 125 nV can be induced in our coil as the result of the earth's main field moving with the core relative to the crust. Actual measurements of the average voltage when the coil was stationary were about 122 nV. This puts our experimental and theoretical data are in agreement.

Once the coil was shown to be capable of detecting the earth's field, preliminary testing of the detection system was done using 1 µm superparamagnetic magnetite beads with from BioClone Inc. The magnetic beads were made from dilutions of the bead suspension were added to the platform in increasing concentrations and the voltage was measured. The voltage increases with the first three samples to about 50 nV, and fluctuates with the last four from about 40 to 73 nV. The data is graphed in figure 5.2 and shows average corrected voltage induced by the different magnetic bead samples of the 5 minute analysis time.

The BioClone magnetic beads used were 1 micron in diameter, similar in physical size to our bacteria cells and in magnetic field. The idea was that if the beads could induce a detectable change in the voltage then we would expect to be able to

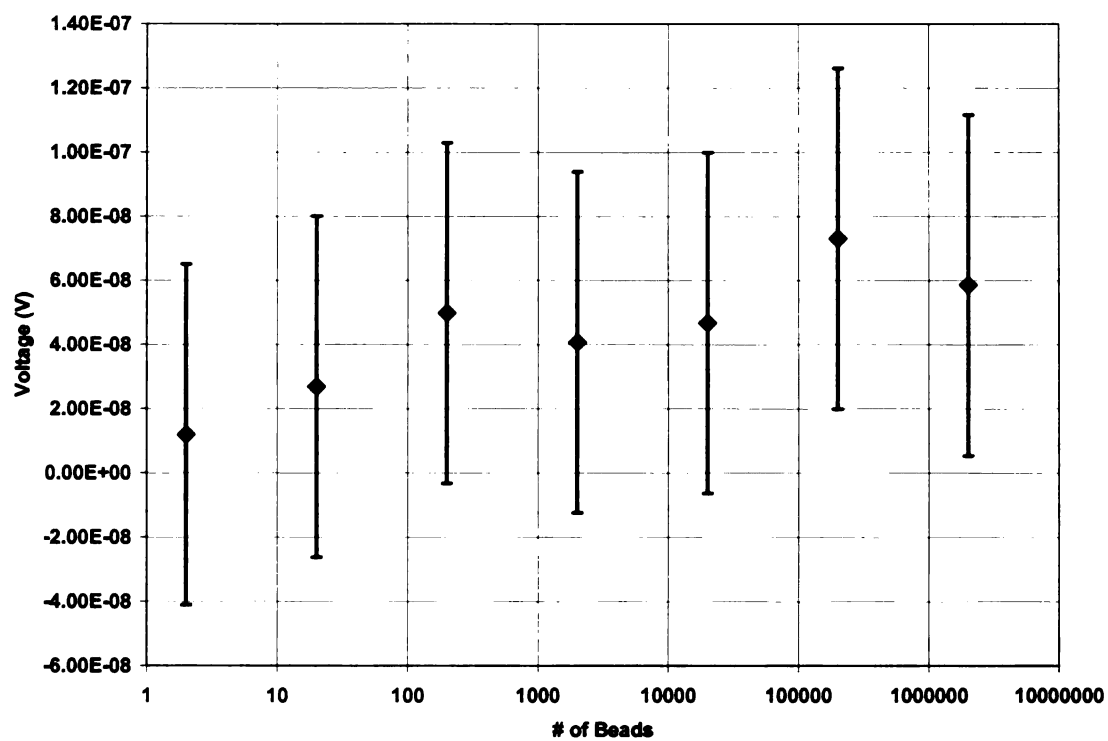


Figure 5.2 The blue diamonds represent the average corrected voltage vs. the number of magnetic beads.

detect a bacterium coated with nanocomposite. We can see from the results (figure 5.2) that as the number of beads in the detection platform increases so does the voltage. It must also be noted that analysis of the raw data and visual observations showed that the magnetic beads quickly became dispersed throughout the circulating solution. This is seen in the data that the voltage increases with more beads and maintains an average voltage and not a distinctive periodic voltage jump when the beads pass through the coil. The dispersion of the beads has an averaging effect on the voltage induced because the beads become evenly distributed throughout the solution resulting in an average magnetic flux passing through the coil. The dispersion of particles throughout the circulation solution seen with the magnetic beads can also be seen with the nanocomposite suspension and *Rhizobium trifolii* data. The data shows an averaging of the induced voltage as well.

With the preliminary tests showing results it was time to test the nanocomposite and *Rhizobium trifolii*. The nanocomposite was loaded into the detection platform to which samples of *Rhizobium trifolii* were added with different concentrations. Figure 5.3 shows the voltage measured over the 5 minute analysis time for one of the samples (raw data). Figure 5.4 shows a graph of all of the samples with some line smoothing applied to the data. In Figure 5.2 we can see the graph of the average corrected voltage and number of cells in the system. The voltage appears to increase logarithmically as a function of the number of cells. As a control the nanocomposite was tested using *Escherichia coli* instead of *Rhizobium trifolii*. Again the nanocomposite was



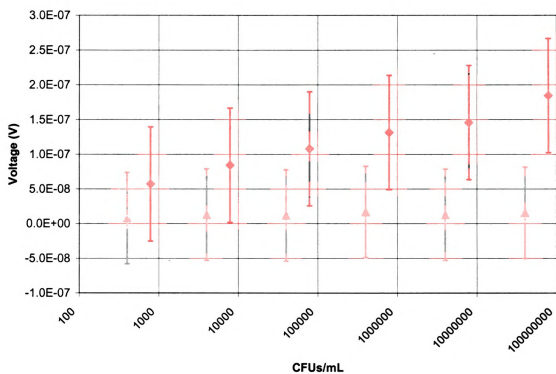


Figure 5.3 Graph of Average corrected voltage vs. the number of CFUs/mL. The orange squares represent the nanocomposite and *Rhizobium trifolii* data. And the yellow triangles represent the nanocomposite and *E. coli* cell data.

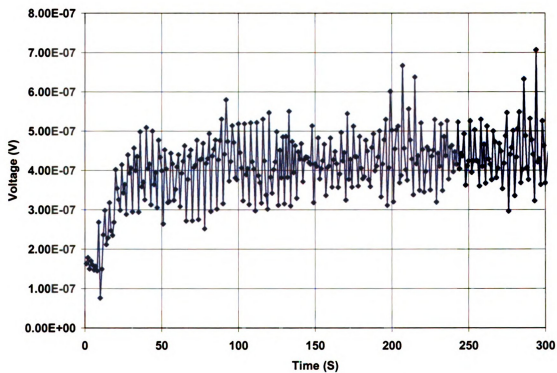


Figure 5.4 Raw data of voltage induced over the 5 minute analysis time from the  $7.89 \times 10^6$  CFU sample (raw data).

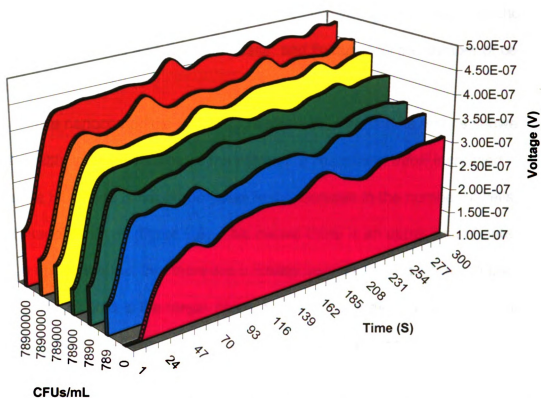


Figure 5.5 Graph of all of the nanocomposite and *Rhizobium trifolii* data samples with line smoothing applied to the data.

loaded into the detection platform and then cell suspensions of different concentrations were added to the detection platform and the voltage measured. The data for the average corrected voltage for the nanocomposite and *Escherichia coli* cells is plotted on Figure 5.3. The voltages are less than those of the *Rhizobium trifolii* and nanocomposite, and fluctuate as the number of cells increases.

The nanocomposite and *Rhizobium trifolii* experiments results showed a measurable induced voltage as the number of *Rhizobium trifolii* increased. The increase in voltage is not proportional to the increase in the number of cells, and the voltage levels off (figure 5.6). This means there is an upper limit of detection. This is due to the fact that there are a limited number of NC particles in the suspension to bind to the target. Once all of the NC particles have been used up (bound to target) addition of more cells will not increase the voltage.

As mentioned before, the core of the nanocomposite is superparamagnetic. How is it possible that they are not only able to induce a voltage but a positive voltage in the experiments? In order to explain the observed phenomena we have to take another look at the magnetic energies involved, specifically the Zeeman energy. The Zeeman energy is dependent on the magnetic moment, the external magnetic field and the angle between them. In our case the external magnetic field is the Earth's magnetic field. While we used a Faraday cage to remove noise from electromagnetic radiation, the earth's magnetic field is not removed.

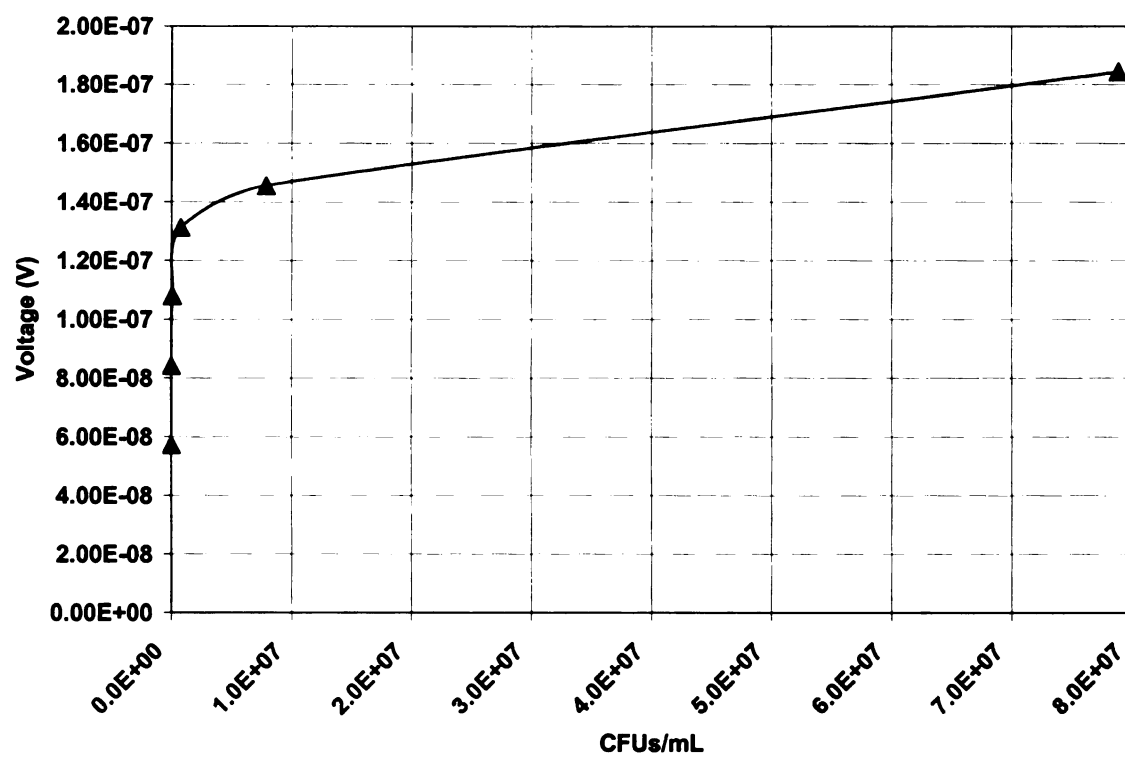


Figure 5.6 Average corrected Induced Voltages by the nanocomposite and *Rhizobium trifolii*.

Knowing the core particle size we can now calculate the Zeeman energy of a single particle in the field and use the Langevin function to determine its average orientation. The Zeeman energy of a single nanocomposite particle in the earth's field is  $1.125 \times 10^{-24}$  J, much less than the thermal energies  $4.14 \times 10^{-21}$  J. While a single nanocomposite particle does not have enough energy to align with the earth's field, a large enough assembly of them does. If we use the Langevin function and look at the average angle as a function of the number of nanocomposites we see that at about 5000 particles the Zeeman energy is greater than the thermal (Figure 5.7). With large assemblies of the nanocomposite on the bacteria surface in the range of 15,000 we can see that there is sufficient energy for interaction. The interaction of the nanocomposites in a large assembly and their interaction with the Earth's magnetic field not only allows them to overcome the thermal energy and behave as a large ferromagnetic particle with a large magnetic moment, but also aligns it with the earth's magnetic field, which causes them to pass through the coil in the same orientation. And because of this permanent orientation of the magnetic field the voltage induced is positive. One question that you may be wondering by now is that why isn't the average voltage zero. As we would have expected from looking at the theoretical calculation where the voltage goes through a positive and then a negative maxima which would lead to an average voltage of zero, and yet we can see from the results that there is a net voltage. What this tells us is that there is a difference in the voltage induced by the bacteria when it enters the coil and when it leaves the coil. So there must be some change in the direction of

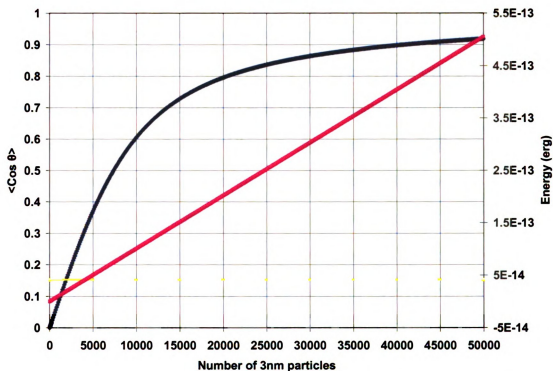


Figure 5.7 Graph of the average angle of alignment of the nanoparticles in the earth's field as a function of the number of 3 nm particles (blue line). The Zeeman energy of the nanoparticles in the earth's field as a function of the number of 3 nm particles (pink line) and the Thermal energy (Yellow line) at room temperature.

the magnetic field as the bacterium moves through the coil. The Lenz's Law states that the path of a moving charge particle is changed in any way by its interaction with a magnetic field, the change is always of such a nature as to generate a new magnetic field which directly opposes the one which caused the change [9]. This means that a voltage induced by the magnetic bacterium moving through the coil generates a magnetic field that apposes the field of the magnetic bacterium. The apposing Lenz field acts to push against a magnet entering a coil and pulls it back exiting the coil. If the Lenz field is strong enough one can see how it can change the direction of the magnetic field. As the magnetic bacterium enters the coil it induces a voltage that generates an opposing field. This opposing field is not felt right away for there is some lag. The opposing field reaches a maximum after the magnetic bacterium has passed half way through the coil. The Lenz field causes a reorientation or flipping of the magnetic bacterium as it is heading out of the coil, which maintains the positive sign of the voltage. Using the voltage induced by the magnetic bacterium, the Lenz field produced in the coil is equivalent to that of earth's field. This is strong enough for the above interactions and explains the net average voltage. The strength of the Lenz field is equal to that of the field of the FMNCP coated bacterium. The fields produced by the samples are listed in table 5.1. The magnetic fields are the same order of magnitude to that of the earth's field which we know from earlier calculation and as a result rotates the magnetized bacteria.

*Escherichia coli* were used to test for nonspecific binding interactions of nanocomposite with non-target bacteria. The data is graphed in figure 5.2 along



**Table 5.1 Voltages and magnetic fields generated by the FMNCP coated bacterium.**

<b>Sample</b>	<b>Average Voltage (V)</b>	<b>Magnetic Field (T)</b>
nc6	3.20615E-07	4.25908E-05
nc5	3.47608E-07	4.61766E-05
nc4	3.71457E-07	4.93448E-05
nc3	3.94712E-07	5.24339E-05
nc2	4.0903E-07	5.43359E-05
nc1	4.47905E-07	5.95001E-05

with the other data. The graph shows us that the voltage fluctuates up and down with increasing concentrations of cells, with an overall small change in voltage. The small change in voltage indicates that there is minimal non-specific binding.

Table 5.2 gives the ionic strengths of the different solutions along with the average voltage induced over the 5 minute analysis time. The Control experiment one Results were similar for all speeds tested forward and reverse. Meaning that running the pump backwards does not change the voltage measured. We can see that there is no correlation between the Average voltage and the ionic strength of the solution with the data being scattered. While the voltages are high when compared to that seen in the nanocomposite and *Rhizobium trifolii* experiments it must be noted that this data has no way of correcting for measurement taken on different days for comparison.

Control experiment two tested to see if the voltage induced changed with the concentration of the nanocomposite suspensions, as well as with the speed of the suspension passing through the coil. Figure 5.8 shows the average voltages of the different nanocomposite suspensions at speed 5 and 10. As you can see the voltage induced, increases as the speed is increased as one would expect, and the average voltage increases minimally with increasing concentration.

In control experiment Three an experiment was run to measure the voltage induced by the *Rhizobium Trifolii* cell by then selves to insure that the voltage induced by the nanocomposite and *Rhizobium trifolii* experiments was not just a result of adding *Rhizobium trifolii*. Figure 5.9, 5.10 shows the graph of

Table 5.2 Control samples conductivity and average voltage with standard deviation.

Sample	Conductivity (1/ $\Omega$ )	Average Voltage (V)	STDEV
Rusty Tap water	808	1.79093E-07	4.22983E-08
Tap water	898	1.73363E-07	5.4657E-08
D.I Tap water	5.2	1.784E-07	3.02854E-08
MilliQ water	0.4	1.20468E-07	3.08291E-08
PBS	14620	2.68714E-07	5.99821E-08
NaCl 1M	82100	1.22225E-07	8.52331E-08
NaCl 0.5M	55000	1.85987E-07	8.86639E-08
NaCl 0.1M	17600	1.89771E-07	9.89374E-08
NaCl 0.01M	1230	1.52554E-07	9.90029E-08
NaCl 0.001M	144	1.28248E-07	7.54727E-08

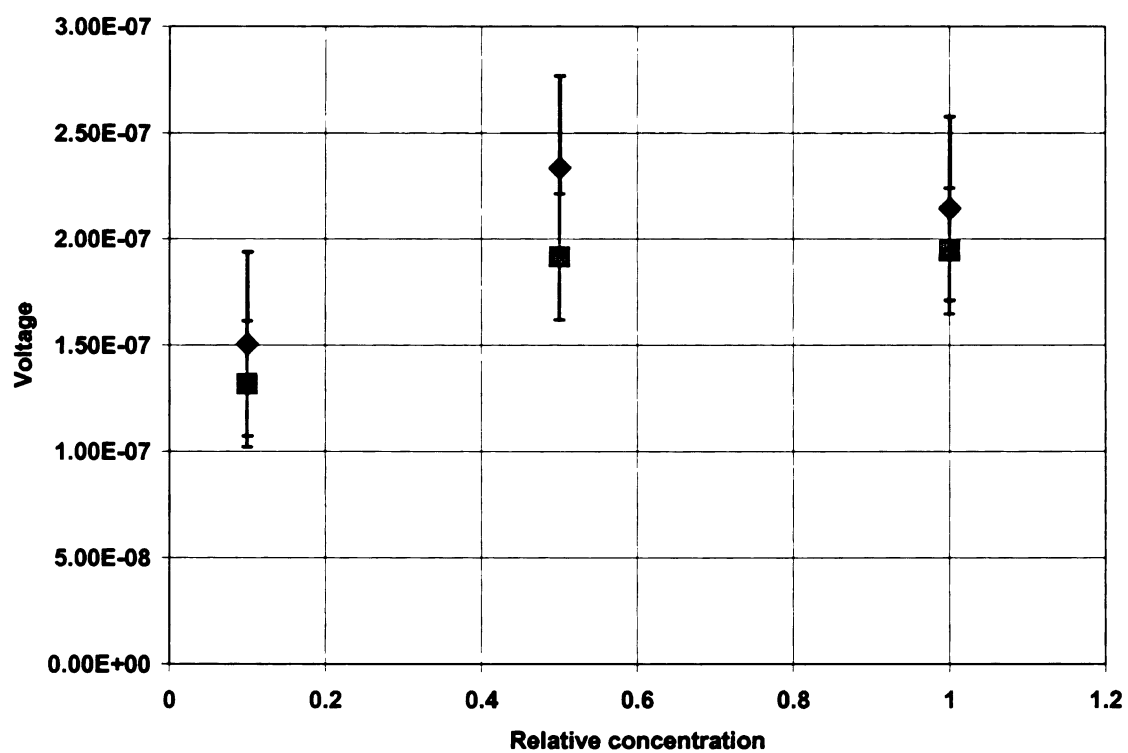


Figure 5.8. Average voltages of the different nanocomposite suspensions at speeds 5 (pink) and 10 (Blue).

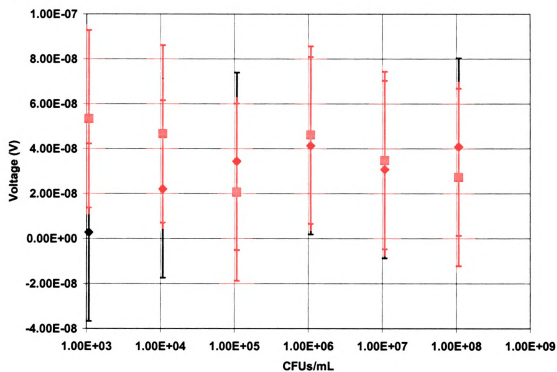


Figure 5.9 Graph of the average corrected voltage vs. the number of cells for *Rhizobium Trifolii* cell. Data from measurements taken from high concentration of cells to low concentration are in red the from low to high are in blue.

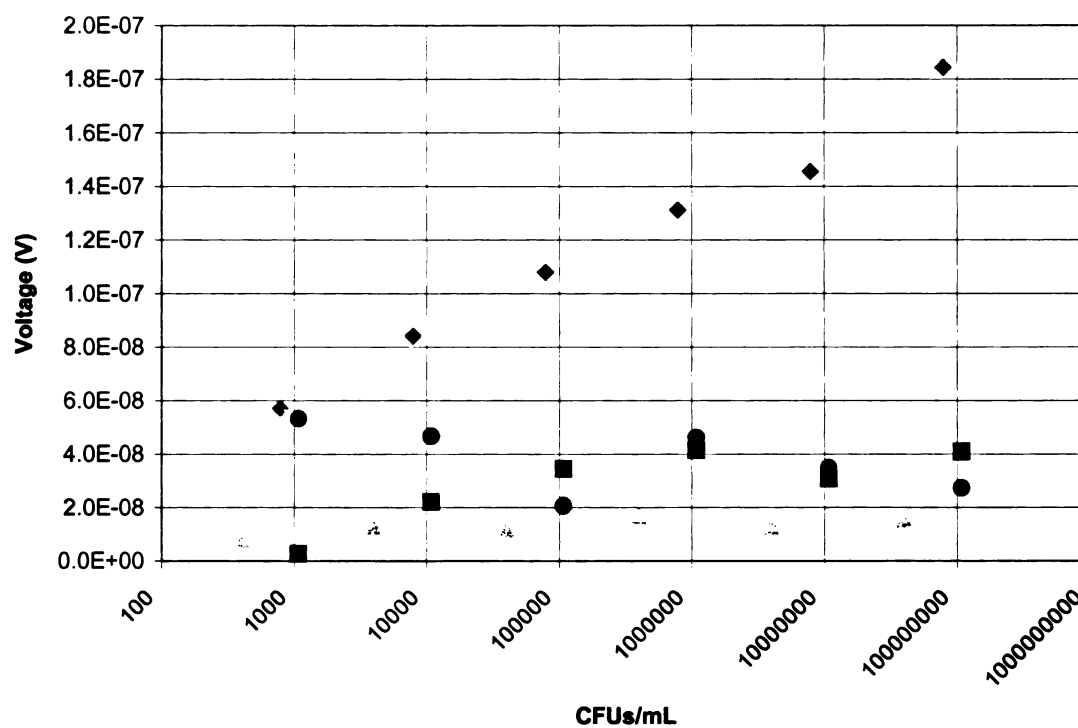


Figure 5.10 Graph of all the corrected voltage data; The orange diamonds show nanocomposite *Rhizobium trifolii* data, the yellow triangles are the nanocomposite and *E. coli* cells data. The red circles are the High to low data and the purple squares are the low to High data.

the average corrected voltage vs. the number of cells. The test was done twice once from highest to lowest concentration and once from low to high. While the voltage increases with concentration in the low to high test in the first 3 samples, it fluctuates in the last 2 as does the high to low over the whole range. While the voltages induced are comparable to the voltages of the lower nanocomposite and *Rhizobium trifolii* experiment, the data is vary scattered. The voltage induced in the experiments is due to the nanocomposite and *Rhizobium trifolii* interaction and not the *Rhizobium trifolii*.

## **Conclusion**

I have been able to design, fabricate, and test our detection system and have shown that our detection platform is capable of a real time detection of bacteria (within five minutes) and low concentrations of cells. And most definitely has the potential for single cells detection. I have demonstrating that Ferromagnetic nanocomposite particles can be used for the detection of bacterial cell by magnetic induction with a search coil. By design our detection platform is capable of a 3 star rating for all of the detection platform features, speed, accuracy, sensitivity, portability, robustness, and ease-of-use. This detection platform has been shown to have the elements of speed, accuracy, and sensitivity. The other elements of portability, robustness, and ease-of-use are areas of improvement and testing in future prototypes. As mentioned before the true challenge for all detection platforms is speed. The time from the moment a sample is taken to the point of detection is crucial. Accuracy is also a challenge that must be balanced with speed. We must keep in mind that there will always

be trade offs between speed and accuracy. We have shown that our detection platforms can perform at the desired speed, and are quite capable of embodying all of the features needed. By no means is our system perfect, nor would we expect to make one. In our system we seek a balance between certainty and time. With infinite time one could know with absolute certainty but time is not infinite and decisions must be made immediately and actions taken.

It is because of this urgency that our idea has evolved beyond a detection platform to a global monitoring system of the origin and progression of disease. In order to create such a system, improvements upon our design must be made. Work has already begun on designing the next prototype, which we will describe here. The detection platform will again make use of Faraday's law of induction, but will not require the need of a pump to circulate the suspension; this greatly reduces the size and possible problems. The basic form and function of the detection platform is as follows. A bacterium enters the detector where it becomes encapsulated with FMNCP and is captured on a small rotating disc. As the FMNCP-encapsulated bacterium rotates on the disc it passes a coil that is located just above the disc. This coil will be able to detect the changes in the magnetic field as the disc rotates. This design allows us to greatly increase our sensitivity in two ways. One is that the speed of the disc's rotation can be controlled to increase the signal. Second the immobilized bacterium will rotate with the disc at a set period, allowing for frequency based detection. Fourier transform can be used to pick up the frequency dependent signals that are buried in the noise. The disc will be disposable, made for one day use, coming as easy



to change cartridges. The used cartridge is removed and discarded and the platform is flushed with sterile water. The new disc cartridge is inserted, then a volume of sterile water is added to rehydrate the disc resuspending and desolving FMNCP, buffer, etc. Circulation of the suspension in the detection platform will be accomplished by convection generated by the rotating disc (this may require some type of structures like grooves, holes, or fins on the disc in order to make it flow accordingly). We have several ideas for the design of the disc. One idea is to have a uniform film of FMNCPs suspended or immobilized in/on a membrane. Basically the FMNCPs are stuck on the disc but have enough freedom and are in large enough concentration that when a bacterium is captured on the disc by FMNCP it will become bound by all of the surrounding FMNCPs. The thought is that a uniform thin film of FMNCPs can be scanned by the coil and give a uniform signal. The binding of the bacterium will cause a discontinuity in the film with an area of no FMNCPs surrounding the bacterium and a large concentration of them at the center. This discontinuity in the field is then picked up by the coil as it passes over the bacterium.

Another design is one that uses SRMs immobilized on the surface of the disc and the FMNCPs are free in suspension. The bacterium picks up FMNCP as it circulates and becomes captured on the disc. The captured bacterium picks up more FMNCPs as it rotates. The build up of FMNCPs on the disc leads to the induction in the coil and detection. We have thought of ways for several pathogens to be detected at the same time by the use of multiple rings on the disc each with different SRMs for their specific target pathogen. While we have

chosen to use coils as our detector in our platform, several different magnetic sensors could be substituted, such as atomic magnetometers, Hall sensors, and GMR to name a few.

The proliferation of personal electronics such as cell phones is apparent all over the world. Integration of our detection platform in to these electronic devices would allow for a broad distribution of detectors throughout a community, whether it be rural, suburban, metropolis, third world or first. A distribution of detectors such as this could supply a level of detection coverage unattainable by any other method.

There are many possible future uses of this technology that could go beyond pathogen detection. The ability to modify an organism with nanocomposite materials has great potential. Not only do we have the ability to genetically modify an organism but, now we can also physically modify it. The nanocomposite material will impart optical and magnetic properties of the nanoparticle to the organism. Incorporation of nanocomposite materials can also go beyond surface modification. Proper coating of nanocomposites and treatment of organisms would allow for internalization of nanocomposite materials. The ability to magnetically modify an organism has many possibilities.

The magnetic modification of an organism allows us a great deal of control over the organism's positioning, orientation, spacing and interaction with others. One can imagine magnetic positioning of cells on surfaces in specific patterns. These cells could produce specific biomolecules such as proteins, lipids, carbohydrates, etc. The precise control over the positioning of the cells would

allow for fabrication of biomaterials with ordering and patterns unparalleled to anything found in nature. This would allow for the production of biomaterials that not only are vastly superior to current materials, but have properties that we have only dreamed of. Another use could be for cellular reconstruction/deconstruction in damaged/unhealthy tissue. One could also imagine magnetically modified organisms used for power generation. Magnetically modified organisms could be made to swim through small coils to generate an EMF to power small electronics.

The physical modification of cells brings us closer to closing the gap between inorganic and bioorganic technologies. While our inorganic technology has advanced much faster than our bioorganic technology, the latter is slowly gaining momentum. We can envision a future where the bioorganic and inorganic technologies merge and form a seamless interface. Science can be simple and easy or complex and difficult, but if we are to make something that will impact the world and help mankind we must be able to put it in the hands of the people of the world in a way that is simple and convenient. We have shown that the modification of a bacterium with ferromagnetic nanocomposite material can be used to generate a signal allowing for detection of a single cell. We have also suggested many improvements and ideas for future devices and applications, which we hope to see come to fruition.

## REFERENCES

1. Low-frequency noise measurements on commercial Magnetoresistive magnetic field sensors. Stutzke, N.A. Russek, S.E. Pappas, D.P. Journal of Applied Physics. Vol:97, 2005.
2. Advances in giant magnetoresistance biosensors with magnetic nanoparticle Tags: review and outlook. Wang, S.X. Li, G. IEEE Transactions on Magnetics, Vol 44, No 7, pg 1687-1702, 2008.
3. P. Leroy, C. Voillot, V. Mosser, A. Roux, G. Chanteur, An ac/dc magnetometer for space missions: Improvement of a hall sensor by the magnetic flux concentration of magnetic core of a searchcoil. Sensors and Actuators A-Physical Vol:142, 2 pg 504-510, 2007.
4. M.H. Acuna, D. Curtis, J.L. Scheifele, et al. The STEREO/IMPACT magnetic Field Experiment. Space Science Reviews Vol:136 Issue:1-4 pg:203-226, 2008.
5. P.D.D. Schwindt, B. Lindseth, S. Knappe, V. Shah, J. Kitching, Chip-scale atomic magnetometer with improved sensitivity by use of the  $M_x$  technique. Applied Physics Letters, Vol:90, 2007.
6. A. Edelstein, Advances in magnetometry. Journal of physics condensed matter, Vol:19 Issue:16, 2007.
7. X. Song and P. Richards, Seismological evidence for differential rotation of the Earth's inner core. Nature, Vol:382 pg:221-224, 1996.
8. G.A. Glatzmaier and P.H. Roberts, "Rotation and magnetism of Earth's inner core," Science, Vol:274 pg:887-1891, 1996.
9. H. E. Burke, Handbook of Magnetic Phenomena, Van Nostrand Reinhold Company Inc, 1986.

## **Appendix A**

### **Magnetism**

#### **Introduction**

Magnetism is a phenomenon that man has tried to understand and manipulate for thousands of years, with the earliest discovery credited to the Chinese in 4000 B.C. [1]. The naturally occurring iron ore magnetite, also known as lodestone, was of great interest because of its tendency to attract steel and iron. Beginning with the first compasses that changed navigation to electric dynamos and motors, and today's advanced materials we can see throughout history that as our understanding of magnetism has grown so has our technology which has allowed for greater discoveries.

The earth's magnetic field can in most cases be thought of as a bar magnet with the magnetic field being the strongest at the poles with field lines emerging from the north pole (geographic south pole) and reentering at the south pole (geographic north pole). The earth's magnetic field forms a toroid around the earth creating the magnetosphere. The earth's magnetosphere protects the earth against solar winds and radiation. Even so the earth's magnetic field is relatively weak at the surface about  $5 \times 10^{-5}$  Tesla, this is a few hundred times weaker than an average refrigerator magnet. While our simple bar magnet model works nicely to visualize the earth's magnetic field at the surface and in the magnetosphere it does not lend any insight as to its origin. The earth is made up of 4 layers, starting with the crust on the outside then the mantle, followed by a liquid outer core and a solid inner core. The cores are made up mainly of iron. But it is not

the permanent magnetization of this iron that gives rise to the earth's magnetic field, for the temperatures at the core are far above that of the Curie temperature of iron, making permanent magnetization impossible. So what is the origin of the earth's magnetic field? Many theories have been proposed, but all have fallen short except for the Geodynamo theory which was first suggested by Larmor in 1919 [2]. Geodynamo Theory, simply put, says that the earth's magnetic field is the result of electrical currents in the liquid outer core. The electrical currents are generated by movement of core fluid by convection and rotation [3, 4].

We have all played with bar magnets at one time or another and noticed their interesting interactions with different materials and other magnets. Magnets are always made up of a "north and a south pole", more properly called a magnetic dipole. The magnetic field of a magnet can be visualized as coming out of the north pole and bending back down and around to enter at the south pole in a toroidal shape. This basic picture of a magnetic dipole holds true for all magnets regardless of size (Figure A1). This is not to say that the magnetic properties of a nanomagnet scale proportionally to those of a large bar magnet of the same material, only that the resulting magnetic dipoles look and behave like those of all magnets.

So what is the origin of the resultant magnetic dipole in our picture? The origin of the resultant magnetic dipole in a magnet is the product of individual point magnetic dipoles that are aligned parallel with one another. We can now visualize our magnet as a collection of point magnetic dipoles (Figure A2) that are the result of unpaired electrons within the material. The cause of magnetism

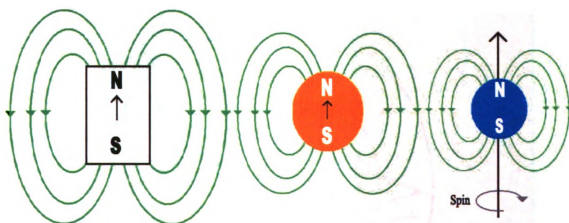


Figure A1 The toroid shaped magnetic fields of magnetic dipoles of different sizes. From left to right a bar magnet then a nanoparticle and last an electron.

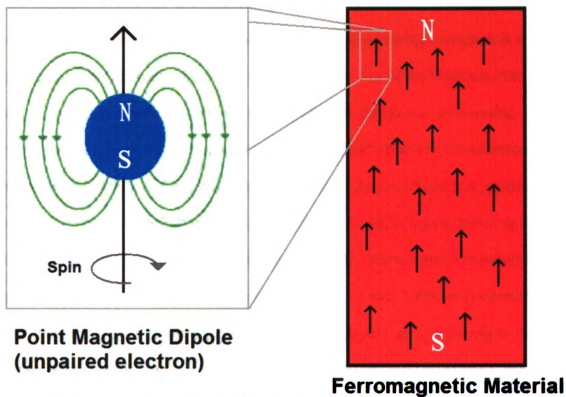


Figure A2 The cooperative interaction of the point magnetic dipoles in ferromagnetic materials results in a net magnetic moment.



is the movement of charged particles; whenever a charged particle moves, it creates a magnetic field. For example when a current is passed through a wire (moving electrons) it creates a magnetic field perpendicular to the direction of the movement of the current by the logic of the right-hand-rule. The relationship between a moving charge and a magnetic field is stated by Ampere's law:

$$dH = ki(dl/r^2)\sin\theta$$

Where  $dH$  is the resultant magnetic field of the moving charge,  $k$  is a constant,  $i$  is the current that travels along the path  $dl$ ,  $r$  is the distance from the path to field of interest, and  $\theta$  is the angle between direction of the moving charge and the field. The movement of the charged particle can be rotational as well as translational; it is the rotation or spinning of the electrons that generates the magnetic field. Electrons can have one of two possible spins, that is spin up or spin down which is assigned a value of  $+$  or  $-\frac{1}{2}$ , respectively. I mention this because electrons spins pair in opposite directions, which effectively cancels out their magnetic fields; this is why only unpaired electrons can contribute to the magnetic field of the magnet with the exception diamagnetic response. While the orbital motion of the electron and nuclear spin can contribute to the magnetic field, they are negligible compared to the magnetic moments of the electron spin. The unpaired electrons act as point magnetic dipoles within a material. One might assume that all materials with unpaired electrons are ferromagnetic, when in fact most are not. While our simple model of a magnet as an assembly of parallel point magnetic dipoles that sum to make one larger magnet dipole is still true, there are microscopic and atomic interactions and assemblies of magnetic

dipoles that affect the net magnetic moment of the magnet that causes not all dipoles to be aligned cooperatively.

### **Magnetic Energies**

There are several energies that contribute to the magnetism of a material, and the degree of their contributions results in the magnetic properties of a material. These energies are exchange, magnetostatic, anisotropy, and Zeeman energies [5]. An important energy that we must not neglect is the thermal energy ( $E_{thermal} = kT$ ), which sets the scale that all other energies are compared to. As the temperature of the material is increased, its effects dominate the others. The exchange energy is the result of quantum mechanical exchange interactions that cause neighboring dipoles to align parallel or antiparallel. The exchange interaction acts to orientate many point magnetic dipoles into regular patterns. Magnetostatic energy is due to the interactions of the magnetic dipoles within the material. While the exchange interactions dominate nearest neighbor interactions, the long range magnetostatic interactions minimize energy by domain formation. Anisotropy energy arises from the crystal structure and shape of the material, and causes the point magnetic dipoles to favor alignment along specific crystallographic axis. The Zeeman effect causes splitting of orbital spin energy levels when exposed to an magnetic field.

Polycrystalline ferromagnetic materials are made up of several magnetic domains. These domains can range in size from a few tens of nanometers to several microns. As mentioned above, domain formation is driven by magnetostatic interactions as well as exchange and anisotropy. Magnetostatic

(dipole-dipole interactions) energy is lowered by the formation of magnetic flux loops or closures (Figure A3). This lowering of energy is less than the cost to form domain walls. These domain closures provide a path for the magnetic flux within the solid. It is the formation of these domains that causes ferromagnetic materials to have net magnetic moments that are small or zero before magnetization. The domain walls are transition layers between domains in which the spins gradually change direction over many atoms (figure A4). This gradual change is favored over one distinct jump that would leave a discontinuity, as a gradual change of spins lowers the exchange energy by distributing it over many spins. While the magnetization of a material is the result of the summation of its point magnetic dipoles, their cooperative interactions (parallel alignment) is due to an entirely different force. That is, the magnetostatic energy (dipole-dipole interactions) is too small to be responsible for the cooperative interactions when compared with the thermal energy.

The exchange energy is responsible for the parallel and antiparallel orientation of neighboring electrons; in ferromagnetic material parallel configurations are lower in energy than antiparallel.

The size of these interactions results in different magnetic properties. A material can be classified as diamagnetic, paramagnetic, and ferromagnetic. The bulk magnetic properties of a material are best visualized using magnetization curves, also called hysteresis loops (Figure A5). A hysteresis loop measures the magnetization of a material in response to an external magnetic field. Then how do point magnetic dipoles within the material react in the presence and absence

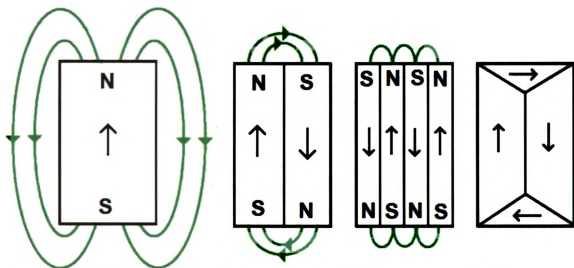
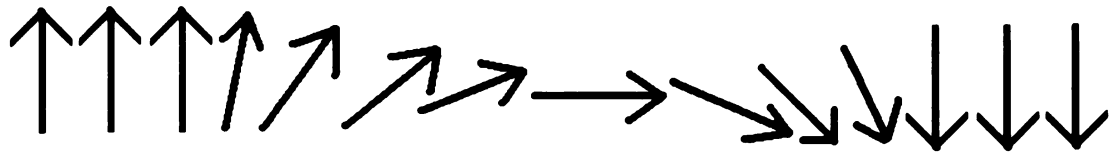


Figure A3 Domain structure of a polycrystalline ferromagnetic material



**Neel wall**



**Bloch wall**

Figure A4 Domain walls are classified as Neel or Bloch walls, depending on the plane of rotation.

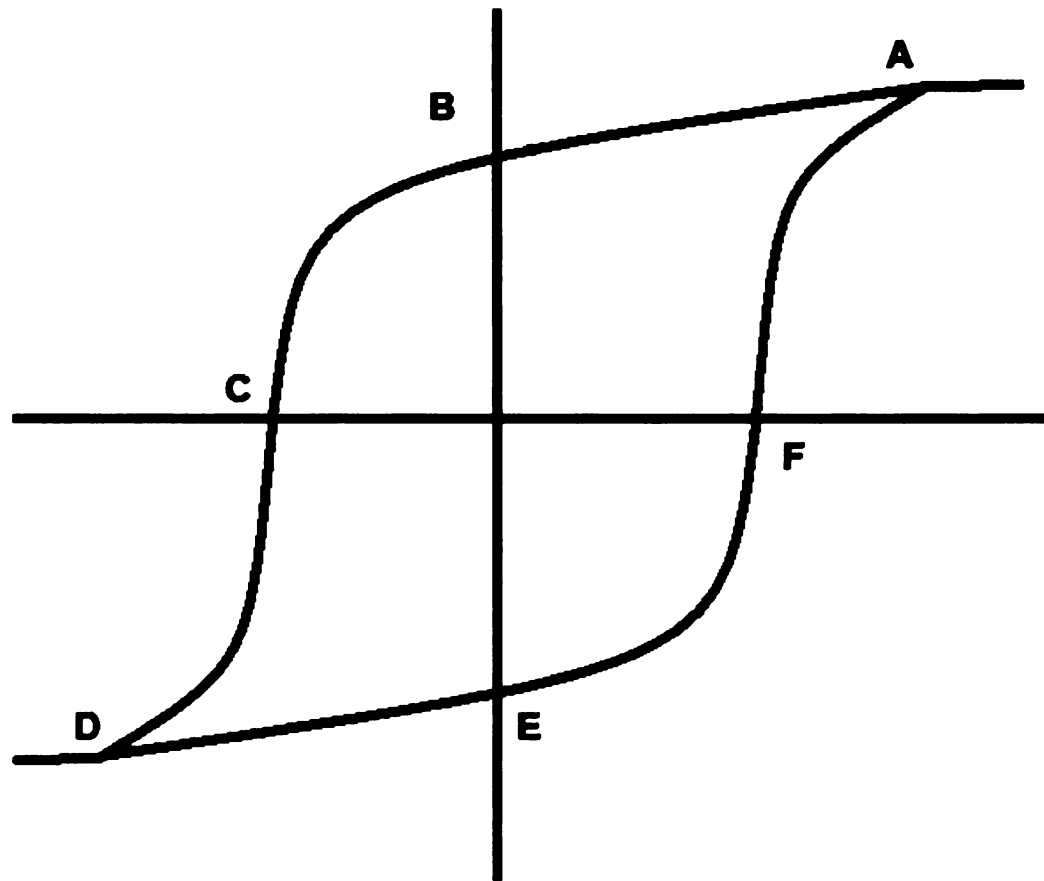


Figure A5 Here is an example of a hysteresis loop where the x axis is the applied magnetic field and y axis is the magnetization of the material. **A** in the figure marks the saturation magnetization when all of the domains are aligned with the field. Point **B** is the remanence or retained magnetization when the applied field goes to zero. **C** is the coercivity which is the field that must be applied to reverse the magnetization to zero. **D** is the same as **A** in the opposite direction. **E** is the same as **B** in the opposite direction, as are **F** and **C**.

of an applied magnetic field. Diamagnetic materials have no net magnetic moment per atom, and in the presences of an external magnetic field the point magnetic dipoles align in opposition to the applied field. The orientation of magnetic dipoles in a paramagnetic material is random in the absence of an external magnetic field, because thermal energy causes jostling of the dipoles and because they have no preferred relationship among them selves. The random orientation of the dipoles results in no net magnetic moment. When an external field is applied to a paramagnetic material the energy of the applied field is strong enough to overcome the thermal energy and the magnetic dipoles align themselves in concurrence with the applied external field. Paramagnetic materials not only align in agreement to the applied magnetic field, they add to the magnetic field with a magnetization that is proportional to the applied field. Ferromagnetic materials, once magnetized, retain a net magnetic moment in the absence of an external magnetic field, and in the presence of an external magnetic field, the degree of magnetization is a factor of the applied field. The magnetization that is retained by a ferromagnet after the magnetizing field diminishes to zero is referred to as its remanence. The magnetic field that is required to return the magnetization of a ferromagnetic material to zero is called the coercivity. The coercivity is related to the anisotropic energy of a ferromagnetic material. The anisotropic energy causes the magnetization of ferromagnetic material to align along crystallographic axis, which are called directions of easy magnetization. Ferromagnetic materials with low coercivities are considered soft and those with high coercivities are called hard. The term

susceptibility is also used to describe magnetic materials, that is diamagnetic materials have negative susceptibilities, paramagnetic materials have low susceptibilities and ferromagnetic materials have high susceptibilities. The susceptibility is given by the following equation:

$$\chi = M/H$$

Where  $\chi$  is the susceptibility and  $M$  is the magnetization and  $H$  is the applied magnetic field. As mentioned above, paramagnetism is the result of thermal agitation, which causes the random alignment of the magnetic dipoles resulting in a net magnetic moment of zero. Ferromagnetic materials have a temperature at which the thermal energy is greater than the exchange and the material becomes paramagnetic: this temperature is called the Curie temperature. The susceptibility of a material as a function of temperature is given by the Curie Weiss Law in the following equation:

$$\chi = C / (T - T_c)$$

Where  $\chi$  is the susceptibility,  $T$  is the absolute temperature,  $T_c$  is the Curie point temperature and  $C$  is the Curie constant of the material. As we can see there are various energies that are at odds with each other in determining the magnetism of a material, and one of the largest effects is due to thermal agitation.



## REFERENCES

1. D.C. Mattis, The theory of magnetism made simple. World Scientific Publishing Company, (2006).
2. P. H. Roberts G. A. Glatzmaier, Geodynamo theory and simulations Reviews of Modern Physics, Vol:72, No. 4, pg:1081-1123 (2000).
3. B. A. Buffett, Earth's Core and the Geodynamo. SCIENCE Vol:288, No.16 pg 2007-2012 (2000).
4. J.A. Jacobs, Reversals of the earth's magnetic field second edition, Cambridge University Press (1994)
5. S. A. Majetich, M. Sachan, Magnetostatic interactions in magnetic nanoparticle assemblies: energy, time and length scales. J. Phys. D: Appl. Phys. 39 pg:R407-R422 (2006)

## Appendix B

### Calculations

Anisotropy energy calculation

$$E_A(\theta) = K_{eff} * V \sin^2 \theta.$$

Where  $K_{eff}$  is the anisotropy constant,  $V$  is the volume of the particle and  $\theta$  is the angle between the magnetization and the easy axis.

For Co,  $K_{eff} = 4.1 \times 10^5 \text{ J/m}^3$ ,  $V = 1.4137 \times 10^{-26} \text{ m}^3$ , and  $\theta = 90$

So  $E_A(\theta) = (4.1 \times 10^5 \text{ J/m}^3)(1.4137 \times 10^{-26} \text{ m}^3) \sin^2 90$

$$E_A = 5.8 \times 10^{-21} \text{ J}$$

The relaxation time for a moment of a particle  $\tau$  is give by the Neel-Brown expression.

$$\tau = \tau_0 \exp(K_{eff} V / k_B T)$$

Where  $k_B$  is the Boltzmann constant and  $\tau_0$  is  $\approx 10^{-9}$  s, and  $K_{eff}$  is the anisotropy constant,  $V$  is the particle volume and  $T$  is the temperature. If the magnetic moment reverses at a time shorter the experimental time then the system is said to be superparamagnetic.

So  $\tau = e(5.8 \times 10^{-21} \text{ J} / 4.14 \times 10^{-21}) \times 10^{-9} = 4.06 \times 10^{-9} \text{ s}$

The magnetic moment of a 3 nm Cobalt particle

$$r = 1.5 \text{ nm} = 1.5 \times 10^{-7} \text{ cm},$$

$$\text{Volume} = 4/3\pi r^3 = 4/3\pi(1.5 \times 10^{-7} \text{ cm})^3 = 1.4237 \times 10^{-20} \text{ cm}^3$$

$$\rho = 8.9 \text{ g/cc}, \quad 8.9 \text{ g/cc} * 1.4237 \times 10^{-20} \text{ cm}^3 = 1.38544 \times 10^{-19} \text{ g}$$

$$1.38544 \times 10^{-19} \text{ g} * 59 \text{ g/mol} = 2.3483 \times 10^{-21} \text{ mol}$$

$$2.3483 \times 10^{-21} \text{ mol} * 6.022 \times 10^{23} \text{ Atoms/mol} = 1414 \text{ Atoms},$$

$$\eta_B = 1.715 \text{ Bohr magnetons/Atom}$$

$$1414 * 1.715 = 2425 \text{ Bohr magnetons} \quad 1\eta_B = 9.234 \times 10^{-24} \text{ Am}^2$$

$$9.234 \times 10^{-24} \text{ Am}^2 * 2425 \text{ Bohr magnetons} = 2.249 \times 10^{-20} \text{ Am}^2$$

$$m = 2.249 \times 10^{-20} \text{ Am}^2, 1 \text{ emu} = 10^{-3} \text{ Am}^2 \quad m = 2.249 \times 10^{-17} \text{ emu}$$

Zeeman energy of particle in earths magnetic field.  $m$  is the magnetic moment of the particle,  $H$  is the magnetic field, and  $\theta$  angle between them.

$$E_z = mH \cos\theta \text{ and } m = 2.25 \times 10^{-17} \text{ emu}, \quad H = 0.5 \text{ G}, \quad \theta = 0$$

$$\text{Then } E_z = 1.125 \times 10^{-17} \text{ erg}, \quad 1 \text{ J} = 10^7 \text{ erg}$$

$$E_z = 1.125 \times 10^{-24} \text{ J}$$

Ampere's law

$$dH = kl(dl/r^2) \sin\theta$$

Where  $dH$  is the resultant magnetic field of the moving charge,  $k$  is a constant,  $I$  is the current that travels along the path  $dl$ ,  $r$  is the distance from the path to field of interest, and  $\theta$  is the angle between direction of the moving charge and the field.

Surface area of circle (loop of coil)

$$\pi r^2 = A, r = 0.5 \text{ mm} = 0.5 \times 10^{-3} \text{ m}, \pi(0.5 \times 10^{-3})^2 = 7.854 \times 10^{-7} \text{ m}^2$$

The magnetic induction  $B$  of 1 tesla generates a force of 1 newton per meter on a conductor carrying a current of 1 ampere perpendicular to the direction of the induction. Earths magnetic at the surface is 0.5 G or  $5 \times 10^{-5} \text{ T}$

The magnetic moment ( $m$ ) of a single Cobalt nanoparticle that has a diameter of 3 nm,  $r = 1.5 \text{ nm} = 1.5 \times 10^{-7} \text{ cm}$

$$\text{Volume of a sphere } V = 4/3\pi r^3 = 4/3\pi(1.5 \times 10^{-7} \text{ cm})^3 = 1.4137 \times 10^{-20} \text{ cm}^3$$

Density of cobalt is  $8.9 \text{ g/cm}^3$ , F.W. = 59 g/mole

$$8.9 \text{ g/cm}^3 / 59 \text{ g/mole} = 0.1508 \text{ moles/cm}^3, \text{ Avogadro's } \# 6.022 \times 10^{23} \text{ atoms/mole}$$

$$(6.022 \times 10^{23} \text{ atoms/mole})(0.1508 \text{ moles/cm}^3) = 9.08 \times 10^{22} \text{ atoms/cm}^3$$

The average Bohr magneton per atom of cobalt is  $\eta_B = 1.715$

One Bohr magneton =  $9.2741 \times 10^{-24} \text{ Am}^2$  or (J/T)

So  $(9.08 \times 10^{22} \text{ atoms/cm}^3)(1.4137 \times 10^{-20} \text{ cm}^3) = 1284 \text{ atoms per nanoparticle}$ .

$1284 \text{ atoms per nanoparticle} * 1.715 \text{ Bohr magneton per atom} = 2200 \text{ Bohr magnetons per nanoparticle}$ .

So  $m = 2200 * 9.2741 \times 10^{-24} \text{ J/T} = 2.04 \times 10^{-20} \text{ J/T}$  for a single 3 nm nanoparticle.

Note: For paramagnets in a magnetic field, their magnetization  $M$  is proportional to the field  $H$ . Energy of a magnetic moment in a magnetic field is  $E = -\mu_0 m \bullet H$ .

Langevin function assumed that moments are non-interacting so it uses classical Boltzmann statistics.  $P(E) = e^{(-E/k_B T)}$

Thermal energy =  $k_B T$

Magnetization is defined as the magnetic moment per unit volume.

$M = NmL(\mu_0 m H / k_B T)$   $N$  is the total number of moments per unit volume and  $m$  is the magnetic moment.

The Langevin equation  $L(\mu_0 m H / k_B T) = \coth(\mu_0 m H / k_B T) - (k_B T / \mu_0 m H)$

The Langevin equation leads to paramagnetic susceptibility and the Curie law susceptibility.  $\chi = M/H$  where  $M$  is the magnetization and  $H$  is the applied magnetic field. Field intensity:  $B = \mu H$ ,  $H$  is the magnetomotive force per unit-length of circuit  $B$  the resulting flux density per unit area And  $\mu$  the permeability of the material

Curie Weiss Law  $\chi = C / (T - T_c)$

$\chi$  is the susceptibility,  $T$  is the absolute temperature,  $T_c$  is the Curie point temperature and  $C$  is the Curie constant of the material

Values and calculations for theoretical maximum.

Surface area of a  $1 \times 3 \mu\text{m}$  bacterium

$$\text{Area of cylinder} = 2\pi r^2 + (2\pi r \times L), \quad r = 500 \text{ nm}, L = 3,000 \text{ nm}.$$

$$\text{Surface area of the bacterium is} = 10,995,574 \text{ nm}^2$$

Volume of bacterium

$$\text{Volume of cylinder } \pi r^2 \times L, \quad \pi \times 500^2 \times 3000 = 2.356 \times 10^{-18} \text{ nm}^3$$

Area covered by a 30 nm nanocomposite

$$\text{Area of a circle } \pi r^2, \quad r = 15 \text{ nm},$$

$$\text{Area covered by a 30 nm nanocomposite is } 707 \text{ nm}^2$$

$$\text{So } 10,995,574 \text{ nm}^2 / 707 \text{ nm}^2 = 15,552 \text{ nanocomposite per bacterium}$$

Volume coil if  $L = 2 \text{ mm}$ ,  $r = 10 \mu\text{m}$

$$2\pi r^2 \times L = \pi (0.001 \text{ cm})^2 \times (0.2 \text{ cm}) = 6.3 \times 10^{-7} \text{ cc}, \quad 1 \text{ cc} = 1 \text{ mL}$$

Speed of particles through the coil, pump flow rate =  $1 \text{ mL/min} = 1.666 \times 10^{-2} \text{ cm}^3/\text{sec}$

$$(\text{flow rate}) \times (\text{area of coil}) = (1.666 \times 10^{-2} \text{ cm}^3/\text{sec}) (\pi 0.001^2) = 53.03 \text{ m/sec}$$

time to pass through the coil is  $37.7 \mu\text{sec}$ .

Magnetic moment (m) of a cobalt nanoparticle with a radius of 10 nm.

Density of cobalt  $8.9 \text{ g/cc}$ , Cobalt has a mass magnetic moment  $m$  of  $100 \text{ emu/g}$ , So  $100 \times 8.9 = 890 \text{ emu/cc}$ ,  $4/3\pi(10^{-6})^3 = 4.188 \times 10^{-18} \text{ cc}$ ,

$$(4.188 \times 10^{-18} \text{ cc}) (890 \text{ emu/cc}) = 4.1 \times 10^{-15} \text{ emu}, \quad \text{units (m)} \quad 1 \text{ Am}^2 = 10^3 \text{ emu}$$

$$m = 4.1 \times 10^{-18} \text{ Am}^2$$

## REFERENCES

1. CRC handbook of Chemistry and Physics 81 edition, 2000.
2. D. Jiles, Introduction to magnetism and magnetic materials, Chapman and Hall, New York. 1991
3. H.E. Burke, Handbook of Magnetic Phenomena. Van Nostrand Reinhold Company, New York. 1986.
4. D.C. Mattis, The Theory of Magnetism Made Simple. World Scientific, New Jersey. 2006.
5. A.H. Lu, E.L. Salabas, F. Schuth, Magnetic Nanoparticles: Synthesis, Protection, Functionalization, and Application. Angew. Chem. Int. Ed, Vol:46 Issue:8 pg:1222-1244, 2007.

MICHIGAN STATE UNIVERSITY LIBRARIES



3 1293 03062 8972